Bluetooth Direction Finding using a Uniform Rectangular Array

Jan Fikse

M.Sc. Thesis
November 2023

Radio Systems Group
Faculty of Electrical Engineering,
Mathematics and Computer Science

University of Twente
P.O. Box 217
7500 AE Enschede
The Netherlands

Supervisors University of Twente:
Prof. Dr. Ir. A. B. J. Kokkeler,
Dr. Ing. A. Lavrenko,
Dr. Z. Mahfouz,
Dr. Ir. A. Chiumento

Supervisors Neways:
Ir. R. Kaspers

UNIVERSITY OF TWENTE.

neways

Acknowledgement

Throughout the journey of my master's thesis, I have been fortunate to collaborate with many exceptional individuals.

First and foremost, I would like to express my deepest gratitude to Neways for their willingness in allowing me to research a topic of my interest. Their contribution of essential resources was pivotal in achieving the objectives of this thesis. My supervisor at Neways, Raymond Kaspers, deserves special thanks for his invaluable guidance in overcoming the challenges of this thesis. I also wish to extend my sincere appreciation to my colleagues at Neways for making my time there truly memorable. The insightful conversations and shared laughter have enriched this journey, making it an experience I will cherish forever.

Secondly, my heartfelt thanks go to my supervisors at the University of Twente: André Kokkeler, Anastasia Lavrenko, and Zaher Mahfouz. Their wealth of knowledge and support, especially during challenging periods, were indispensable.

Thirdly, I am grateful for the opportunity to utilize the anechoic chamber and positioner at ASTRON. Special thanks goes to Marchel Gerbers and Michel Arts, whose assistance was crucial during the preparatory stages and the measurements process.

Last, but certainly not least, I wish to express my deepest appreciation to my family and friends for their support throughout this journey. A special mention goes to my parents, whose love and encouragement have been the foundation upon which this work stands. I am grateful for you, the reader, for accompanying me on my journey and for taking the time to read my work.

Abstract

The Global Positioning System (GPS) has become the de facto standard for outdoor positioning, but it has several shortcomings when used indoors. To overcome these limitations, Indoor Positing Systems (IPSs) have been developed. Although various technologies are available for IPSs, no single standard has been established. Bluetooth Low Energy (BLE), a technology known for its global usage, low cost, and power efficiency, is one such technology. The introduction of the direction finding feature in BLE has significantly improved the accuracy of position estimation.

The Bluetooth SIG does not assign a specific algorithm for direction finding, which opens up opportunities for exploring Direction of Arrival (DoA) estimation algorithms within the context of Bluetooth technology. This thesis primarily focusses on Uniform Rectangular Arrays (URAs), as Uniform Linear Arrays (ULAs) are extensively covered in literature. It compares the theoretical accuracy with results from a commercially available URA. Additionally, the computational complexity of DoA estimation algorithms was examined, providing an analysis among the algorithms as well as between a ULA and URA. Furthermore, this thesis explores potential configurations based on the Bluetooth Core Specifications and investigates techniques to reduce the argument spread to potentially improve the accuracy.

The thesis starts with the background theory, introduces BLE with an emphasis on the direction finding feature. It delves into the principle behind direction finding, starting with a ULA and extending to a URA. Furthermore, data models for both arrays are defined for use throughout the thesis.

Based solely on the Bluetooth Core Specifications, eight configurations of tag and anchors were identified. These configurations were dependent on the communication mode, direction finding method, and antenna composition. The rate at which a Constant Tone Extension (CTE) could be retrieved was also investigated, as it determined the rate at which the incident angle could be estimated. This rate was found to be dependent on the communication mode, either connectionless or connection-oriented, with a minimum time of 7.5 ms between two packets containing a CTE in the case of a single packet per interval.

Four DoA estimation algorithms were analyzed, including two spectral-based methods and two parametric methods. The computational complexity of these meth-

ods was evaluated for both ULAs and URAs. Spectral-based methods exhibited higher computational costs, primarily because the entire spectrum needs to be evaluated. Shifting from a ULA to a URA resulted in an increase in the spectrum by a factor of 180 times, a change which was reflected in the computational complexity. In contrast, parametric methods demonstrated a lower computational complexity, with less than twofold increase when shifting from a ULA to a URA.

The impact of frequency offset and drift were explored through simulation. Several frequency compensation algorithms were introduced and evaluated. The Linear Least Square (LLS) algorithm proved to be most effective when frequency offset was present, but less effective in the case of frequency drift. The algorithm was evaluated on the collected data yielding a Root-Mean-Square Error (RMSE) of less than 1.2° at a transmit power of 8.5 dBm.

The theoretical accuracy of the DoA estimation algorithms was assessed through simulations by varying three key parameters: Signal-to-Noise Ratio (SNR), number of snapshots, and number of antennas. The results revealed that increasing the number of snapshots or antennas only approached a limit, which was dependent on the SNR.

Field measurements were conducted by using a commercially available antenna arrays in two anechoic chambers, one without and one with a positioner to accurately set the incident angle. These measurements allowed for the variation of the three key parameters. The SNR was varied by adjusting the transmit power. However, the range in transmit power was insufficient, as the SNR remained excessively high across all levels of transmit power. A misalignment between tag and anchor was also observed, leading to counterintuitive results. Despite these challenges, the influence of the key parameters on accuracy were discernible.

Finally, two methods of antenna compensation were proposed to reduce the argument spread. Their effectiveness was assessed using the data collected in the anechoic chamber. Additionally, the influence of the snapshot count on the improvement was evaluated. The findings suggest that the improvements were more significant at a lower snapshot count.

Contents

List of Figures

List of Tables

List of Acronyms

AFH	Adaptive Frequency Hopping
AGC	Automatic Gain Control
AoA	Angle of Arrival
AoD	Angle of Departure
AVG	Averaging
AWGN	Additive White Gaussian Noise
BER	Bit Error Rate
BLE	Bluetooth Low Energy
BR	Basic Rate
CTE	Constant Tone Extension
CRC	Cyclic Redundancy Check
DoA	Direction of Arrival
ESPRIT	Estimation of Signal Parameters via Rotational Invariant Techniques
FEC	Forward Error Correction
FLOP	Floating Point Operation
GFSK	Gaussian Frequency Shift Keying
GPS	Global Positioning System
PDU	Protocol Data Unit
IPS	Indoor Positioning System
IQ	In-phase and Quadrature
ISM	Industrial, Scientific and Medical
LLS	Linear Least Squares
LoS	Line of Sight
MUSIC	MUltiple SIgnal Classification

MVDR Minimum Variance Distortionless Response

RFID Radio-Frequency Identification

RMSE Root-Mean-Square Error

RSSI Received Signal Strength Indicator

SNR Signal-to-Noise Ratio

SoC System-on-Chip

UCA Uniform Circular Array

ULA Uniform Linear Array

URA Uniform Rectangular Array

UWB Ultra Wideband

Chapter 1

Introduction

1.1 Motivation

The Global Positioning System (GPS) has revolutionized the way individuals navigate and determine their location in outdoor environments. As a well-established technology, GPS has become the standard for outdoor localization. However, despite its widespread use and success in outdoor environments, GPS is not without its limitations. When used indoors, GPS often lacks precision or fails entirely. This is due to a variety of factors, including obstruction from buildings and other physical barriers.

In order to address the limitations of GPS in indoor environments, Indoor Positioning Systems (IPSs) have been developed. These systems utilize a range of technologies to provide accurate location information within indoor spaces. Among the most commonly employed technologies for indoor positioning are Wi-Fi, Zigbee, Bluetooth, Radio-Frequency Identification (RFID), and Ultra Wideband (UWB) [1]. Each of these technologies offers unique advantages and capabilities, making them well-suited for indoor localization. However, unlike outdoor positioning where GPS is widely accepted as the primary technology, there is no single technology that dominates the field of indoor positioning.

One technology that is widely used as a positioning technology addressing the increasing demand for high-accuracy indoor localization is Bluetooth Low Energy (BLE) [2]. One of its primary design goals is to meet the needs of devices with low power requirements. This makes it an ideal solution for a wide range of applications. Furthermore, the widespread availability of Bluetooth on most devices has driven manufacturing costs down, making BLE an accessible and cost-effective option. With the introduction of Bluetooth Core Specification v5.1 a new capability that supports high-accuracy direction finding is added [3]. This allows devices equipped with an antenna array to accurately determine the direction at which the incoming signal impinges on the antenna array.

The directions from which signals impinge on an antenna array can be determined using algorithms known as Direction of Arrival (DoA) estimation algorithms. These algorithms have been the subject of extensive research in the field of direction finding. In academic literature, the primary focus has been on the Uniform Linear Array (ULA) antenna. As a result, other types of array antennas, such as the Uniform Rectangular Array (URA) and Uniform Circular Array (UCA), are not as widely discussed.

As stated by the Bluetooth Special Interest Group (Bluetooth SIG),

> "The Bluetooth SIG will not designate one algorithm as the standard direction finding algorithm, and so the choice of algorithm is left to the application layer to address. It is believed that this is an area in which manufacturers and developers can compete." [4].

This allows for the exploration and evaluation of various DoA estimation algorithms in the context of Bluetooth technology.

1.2 Research Objective and Questions

This research aims to evaluate the performance of a URA within the context of Bluetooth technology and compare it, where appropriate, with a ULA. Given the aim of this research, several research questions are defined:

1. Based solely on the Bluetooth Core Specifications, what are the unique configurations of tags and anchors, and what rate can the angle of incidence be estimated?
2. How do computational costs of DoA estimation algorithms compare between ULA and URA?
3. Considering the Bluetooth technology, what accuracy is theoretical achievable using DoA estimation algorithms in combination with a URA and how does this compare to the accuracy of commercially available URAs?
4. What techniques can be used to reduce the argument spread between Bluetooth packets on different channels, and how do they affect the accuracy?

In order to ensure feasibility, certain constraints have been established for this research. Firstly, only hardware that complies with the Bluetooth Core Specifications shall be utilized. Secondly, the anchors and tags will be deployed in an indoor environment where a Line of Sight (LoS) can be assumed. Lastly, the tag shall be portable, implying physical and energy constraints.

1.3 Thesis Outline

The structure of this thesis is organized as follows:

- Chapter 2 provides an introduction to BLE, with a special focus on the direction finding feature. It also explains the general principles of direction finding and the key assumptions and data models used in this thesis.
- Chapter 3 explores and discusses the the unique configurations of tags and anchors that are possible by BLE and its direction finding feature. It further investigates the rate at which samples can be collected for estimating the angle of incidence.
- Chapter 4 introduces array signal processing techniques and the DoA estimation algorithms used in this thesis. Additionally, it analyzes the computational complexity of common operations and algorithms.
- Chapter 5 evaluates the performance of DoA estimation algorithms through simulations. It also examines the effectiveness of frequency compensation algorithms.
- Chapter 6 describes the environmental setup and procedure of the conducted measurements. It then presents and analyzes the results.
- Chapter 7 discusses the primary findings and implications of this thesis.
- Chapter 8 concludes the thesis by summarizing the main outcomes. It also provides recommendations for future work.

Chapter 2

Theoretical Background

2.1 Bluetooth Low Energy

Around since the year 2000, Bluetooth technology revolutionized the way data was exchanged between two devices [5]. The first version of Bluetooth technology, known formally as Bluetooth Basic Rate (BR), was incorporated into the earliest Bluetooth products and provided a raw data rate of 1 Mb/s.

BLE was introduced in version 4.0 of the Bluetooth Core Specification with a primary design goal of reducing power consumption. This allows devices to operate for extended periods on battery power. Other design objectives included low cost, reliability, security, and ease of deployment.

2.1.1 Physical Layer

BLE operates within the 2.4 GHz Industrial, Scientific and Medical (ISM) band, which ranges from 2400 – 2500 MHz. This band is divided into 40 radio frequency channels, each with a channel spacing of 2 MHz [6]. The center frequency of each channel can be defined as $2402 + k \cdot 2\,\mathrm{MHz}$, for $k \in [0, \ldots, 39]$. Of these 40 channels, three are designated as primary advertising channels. These channels are specifically selected to minimize the interference from IEEE 802.11 wireless networks [7]. The remaining 37 channels can be used either as secondary advertising channels or as data channels. These channels are also referred to as general-purpose channels. Figure 2.1 presents a overview of the BLE channels, detailing their center frequencies and specific purposes.

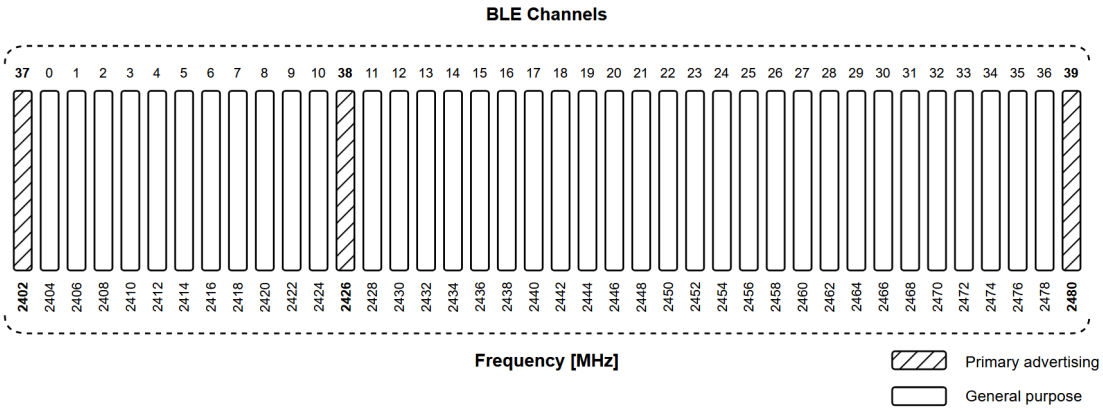

Figure 2.1: BLE's channels and center frequencies

BLE employs Gaussian Frequency Shift Keying (GFSK) modulation with a bandwidth-bit period product of 0.5. According to the BLE specifications, the modulation index must fall within the range of 0.45 to 0.55. To represent a binary one, a positive frequency deviation is used. Consequently, a negative frequency deviation is used to represent a binary zero.

Three modulation scheme variants, where each variant is also referred to as PHY, are defined [5]. The first variant, LE 1M PHY, uses a symbol rate of 1 Msym/s. The support of this PHY is mandatory for any BLE device. The second variant, LE 2M PHY, uses a symbol rate of 2 Msym/s. The support of this PHY is optional. These two PHYs are also referred to as the LE Uncoded PHY. The last variant, LE Coded PHY, uses the same symbol rate as LE 1M PHY but uses a coding called Forward Error Correction (FEC). The support for the LE Coded PHY is optional.

One of the challenges faced by wireless technologies is interference. To enhance immunity to interference, BLE employs a spread spectrum technique known as Adaptive Frequency Hopping (AFH). This technique involves changing the channel based on a channel map at regular intervals. The channel map indicates which channels are used and which are unused. If a channel performs poorly due to interference or other sources of noise, it is marked as unused. This helps to maintain the integrity of the wireless connection and minimize the impact of interference. Table 2.1 provides a concise overview of the key characteristics of BLE.

Table 2.1: Characteristics Bluetooth Low Energy

Characteristic	**Details**
Frequency band	2.4 GHz ISM band
Channels	40 Channels with 2 MHz spacing
Channel usage	AFH
Modulation	GFSK
Modulation schemes and data rates	LE 1M PHY (mandatory): 1 Mb/s LE 2M PHY (optional): 2 Mb/s LE Coded PHY (S=2): 500 kb/s LE Coded PHY (S=8): 125 kb/s
Modulation index	0.45 – 0.55
Bandwidth-bit period product	0.5

2.1.2 Link Layer Packet Structure

The LE Uncoded PHY uses the same packet structure across all physical channels. The structure is comprised of four mandatory fields and one optional field. The mandatory fields include the Preamble, Access Address, Protocol Data Unit (PDU), and Cyclic Redundancy Check (CRC). The optional field is the Constant Tone Extension (CTE). A detailed illustration of this packet structure is shown in Figure 2.2.

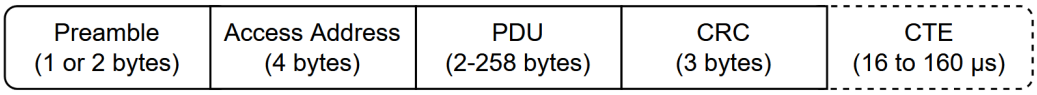

Figure 2.2: LE Uncoded PHY packet structure

The length of the preamble can vary depending on the used PHY. Specifically, the preamble is one byte for the LE 1M PHY and two bytes for the LE 2M PHY. The preamble consists of a fixed sequence of alternating zeros and ones and serves several important functions. These include frequency synchronization, symbol timing estimation, and Automatic Gain Control (AGC) training.

The second field is the access address, which consists of four bytes. This field is used by receivers to determine the relevance of the packet. For instance, connected devices will use the same access address to communicate.

The access address is followed by the PDU. The value of this field is dependent on the type of the packet. For example, when a packet is transmitted on the primary

advertising channel, the PDU shall be of the type Advertising Physical Channel. For a transmitted packet containing data, the PDU shall be of type Data Physical Channel. The length of this field is dependent on the type and can range from 2 and 258 bytes.

The final mandatory field is the CRC. This field is calculated over the PDU and is used to detect transmission errors. To avoid long sequences of zeros or ones, BLE employs data whitening.

The CTE is an optional field that is defined as a constantly modulated series of unwhitened ones. The duration of the CTE can range from 16 µs to 160 µs.

2.1.3 Direction Finding Methods

With the introduction of the Bluetooth Core Specifications Version 5.1 a new direction finding feature is introduced [8]. This feature offers two methods based on the same underlying principle. Both methods require one of the devices to be equipped with an array of antennas. In the first method, Angle of Arrival (AoA), the receiver is equipped with multiple antennas. These antennas are switched during the reception of a Bluetooth packet. In the second method, Angle of Departure (AoD), the transmitter is equipped with multiple antennas. In this case, the transmitter switches the antennas while sending a Bluetooth packet.

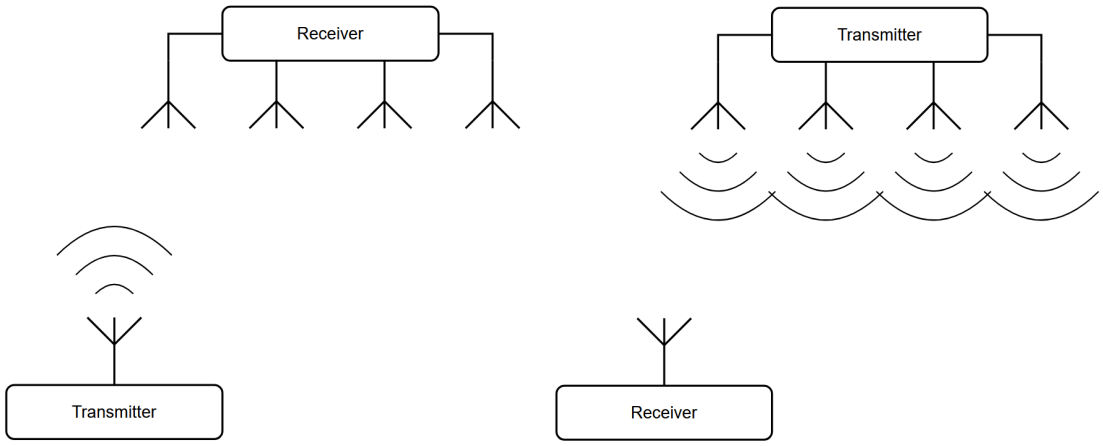

(a) Angle of Arrival (b) Angle of Departure

Figure 2.3: The two BLE direction finding methods

2.1.4 Constant Tone Extension

The CTE is an optional field in the packet structure of the LE Uncoded PHY. The duration of the CTE can vary between 16 µs and 160 µs. Since no whitening shall

be applied, the CTE can be seen as a sinusoidal wave with a positive frequency deviation.

The CTE starts with a 4 µs guard period, which is followed by an 8 µs reference period. During this reference period, a sample is collected every microsecond on the same antenna. Subsequently, the reference period is then followed by a sequence of alternating switch and sample slots, both of identical length. The duration of these slots can be either 1 µs or 2 µs and is also referred to as slot duration. The support for a 2 µs slot duration is mandatory, while the 1 µs slot duration is optional.

The direction finding methods allow different configurations for the transmitter and receiver as shown in Figure 2.4. In the case of AoA, the transmitter consists of a single antenna sending the CTE. The receiver has to switch and sample according to the predefined slot duration. In the case of AoD, the transmitter, consisting of multiple antennas, has to switch its antennas according to the predefined slot duration. The receiver, consisting of a single antenna, has to sample the signal according to the predefined slot duration.

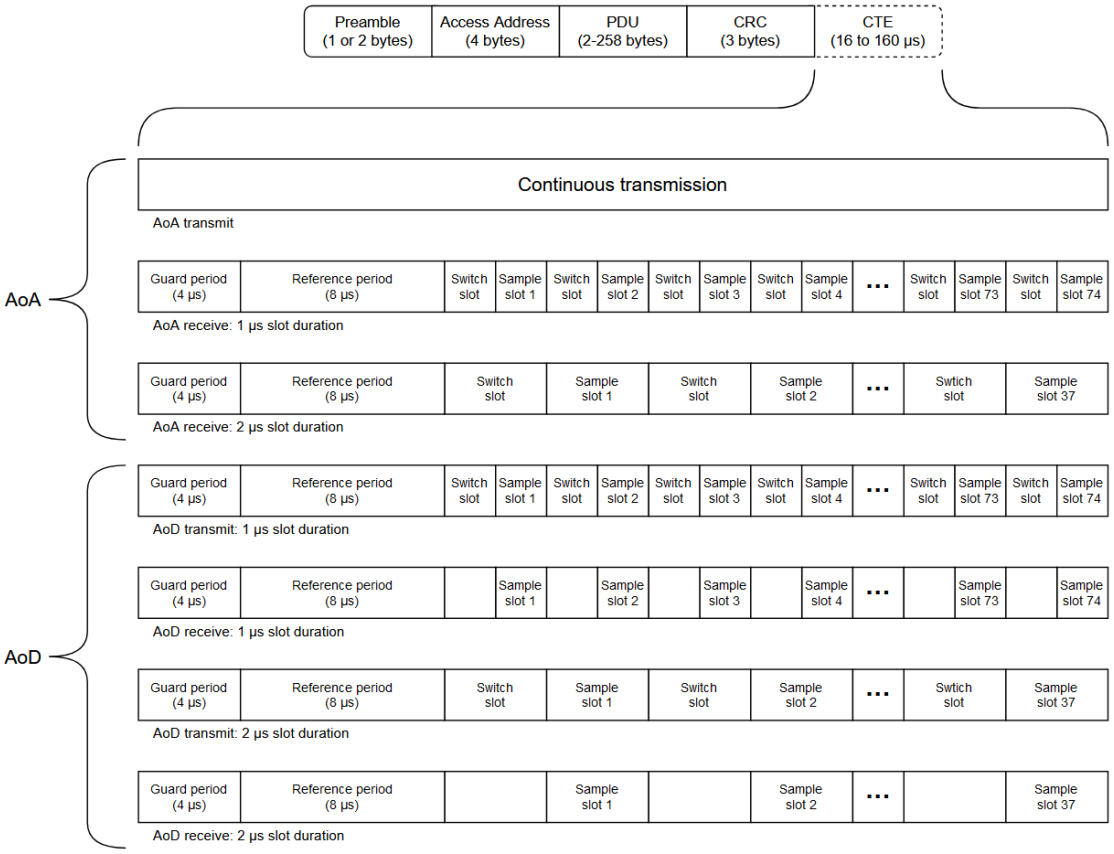

Figure 2.4: Structure of the Constant Tone Extension

2.1.5 Antenna Switching

The switch slots are used to switch between the antennas according to a predefined pattern. This pattern dictates which antenna is employed during each sample slot. During the reference period, the first antenna in the pattern is used. Subsequently, the second antenna in the pattern is employed during the first sample slot. This procedure continues until the pattern is completed. If the pattern is exhausted before the end of the CTE, the pattern is repeated from the beginning. The pattern may comprise any combination of antennas, allowing for the repeated use of the same antenna or the exclusion of certain antennas.

2.1.6 IQ Sampling

The receiver performs In-phase and Quadrature (IQ) sampling when it receives a valid Bluetooth packet containing a CTE. It may also perform IQ sampling even though the CRC is incorrect. It is crucial that the CTE is sampled at a precise point during each sample slot. This sample must fall within the IQ Sampling Window, which starts 0.125 µs after the beginning and ends 0.125 µs before the end of each microsecond period. For the 2 µs sample slot, the sampling must be performed on the latter microsecond. Figure 2.5 illustrates the IQ Sampling Window for both sample slots.

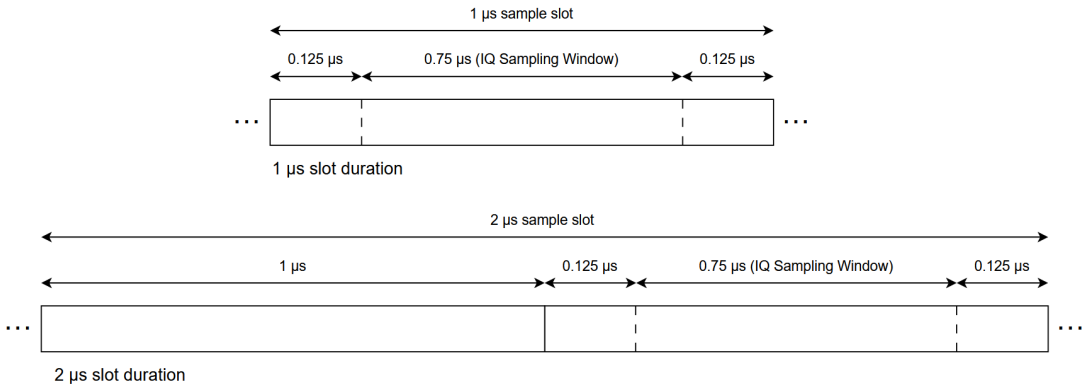

Figure 2.5: IQ sampling slot for a 1 µs and 2 µs sample slot

2.2 Principle of Direction Finding

This section aims to provide a comprehensive explanation on the fundamental principles behind direction finding. The concepts and techniques presented are applicable to a wide range of technologies, and as such, the focus will not be limited to BLE alone. This section begins by outlining the key assumptions used for direction finding and which will be maintained throughout. Subsequently, the concept of direction finding with a ULA is introduced. This concept is then extended to a URA. Finally, a data model for both ULA and URA is defined.

2.2.1 Key Assumptions

Before delving into direction finding, several assumptions are made:

1. *Far-field assumption.* The signal sources are located at a sufficient distance from the antenna array such that each signal can be considered as a planar wavefront. The far-field region, also known as the Fraunhofer region, is typically defined as being at distances greater than $2D^2/\lambda$ from the antenna array [9]. In this equation, D represents the overall dimension of the antenna array and λ is the wavelength of the signals.
2. *Narrowband assumption* [10]. The signals emanating from the signal sources vary slowly over time in amplitude and modulated phase. As a result, the antennas within the array perceive consistent phase and amplitude. Furthermore, it is assumed that the information conveyed by these signals is confined to a narrow frequency band in close proximity to the carrier frequency.
3. *Additive White Gaussian Noise (AWGN).* The noise received at each antenna in the array is assumed to be independent of the noise received at other antennas. The noise follows a normal distribution with a mean of zero.
4. *Isotropic and nondispersive transmission medium.* The transmission medium between the signal source and the antenna array is assumed to be isotopic and nondispersive. This implies that the physical properties of the medium are consistent in all directions and do not vary with the direction of signal propagation. Furthermore, the speed at which the signal travels through the medium is independent of its frequency.

2.2.2 Direction Finding using a ULA

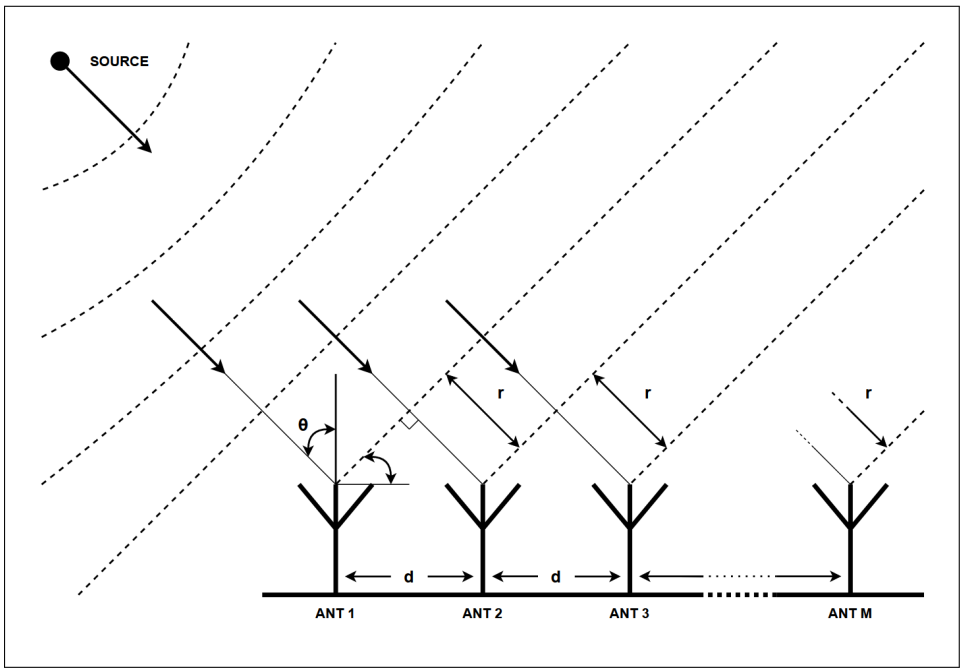

Figure 2.6: Uniform Linear Array

Consider a ULA consisting of M antennas and let d denote the inter-element spacing. The narrowband signal generated by the source impinges on the antenna array at an unknown angle θ. Since electromagnetic waves travel at the speed of light (c) in free space [9], it takes additional time before it reaches the consecutive antenna. This is illustrated in Figure 2.6. Therefore, a delayed version of the signal is received by the consecutive antenna. More generally, the delay τ_i before it reaches the ith element is

$$\tau_i = \frac{(i-1)\,r}{c}, \quad \text{for } i \in [1, \ldots, M]$$

where r denotes the distance that the signal needs to travel between two consecutive antennas.

Using trigonometry, the unknown angle θ and the angle between the wavefront and horizontal axis are congruent. Consequently, the unknown angle can be calculated as

$$\theta = \arcsin\left(\frac{r}{d}\right)$$

Measuring the time-based delay between two consecutive antennas is impractical, as the signal needs to be captured at the speed of light. An alternative method is to measure the phase difference ϕ_Δ between the two antennas. Using an ideal sinusoidal signal, the distance can be expressed as a function of the phase difference:

$$r = \frac{\phi_\Delta}{2\pi}\lambda$$

where λ denotes the wavelength of the sinusoidal signal. The relationship between the wavelength and its frequency f is $\lambda = c/f$. To prevent ambiguity, the distance between consecutive antennas must be less than or equal to half the wavelength.

It is assumed that the phase of the signal is sampled simultaneously at the antennas. Otherwise, the time difference Δt between consecutive samples will introduce a phase offset ϕ_{offset}. This phase offset is a function of the angular frequency ω of the sinusoidal signal and can be written as

$$\phi_{offset} = \Delta t \cdot \omega$$

Substituting the distance based on the phase difference, the unknown phase becomes

$$\theta = \arcsin\left(\frac{\lambda\phi_{\Delta}}{2\pi d}\right)$$

2.2.3 Direction Finding using a URA

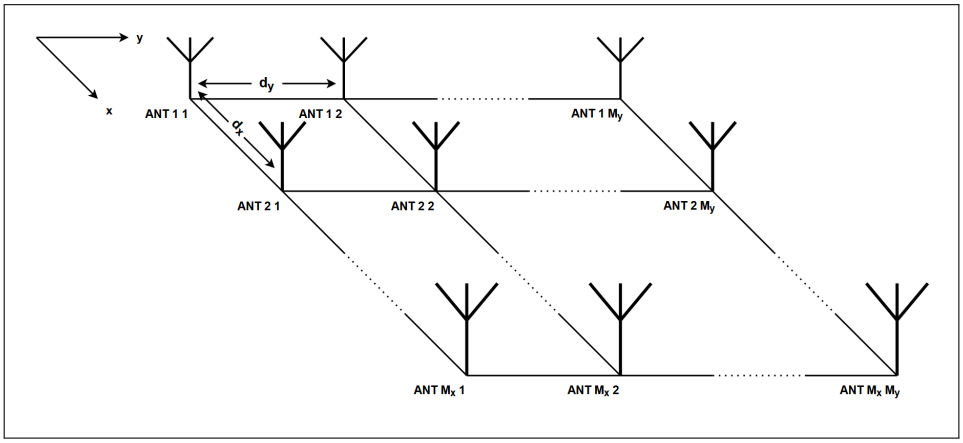

Figure 2.7: Uniform Rectangular Array

The ULA can be extended to a two-dimensional array resulting in a URA antenna. Consider a URA consisting of $M_x \cdot M_y$ antennas where d_x and d_y denotes the inter-element spacing in specified direction as depicted in Figure 2.7.

Similar to the polar coordinate system used in a ULA, the spherical coordinate system can be used for a URA. The direction at which the source impinges on the antenna array can be described using two unknown angles. The angles θ and ϕ will be referred to as the azimuth and elevation, respectively. Given a radius r, the spherical coordinates can be converted to Cartesian coordinates [11]:

$$x = r \cdot \cos(\theta) \cdot \sin(\phi)$$
$$y = r \cdot \sin(\theta) \cdot \sin(\phi)$$
$$z = r \cdot \cos(\phi)$$

Given a Cartesian coordinate, Euler's formula [11], $e^{j\alpha} = \cos(\alpha) + j\sin(\alpha)$, can be used to determine the azimuth and elevation. Assuming that the radius is one or the Cartesian values have been scaled accordingly, the Cartesian coordinate can be expressed as

$$\begin{aligned}\zeta &= x + jy \\ &= \sin(\phi) \cdot e^{j\theta}\end{aligned}$$

Consequently, the azimuth angle θ and elevation ϕ can be obtained

$$\begin{aligned}\theta &= \arg(\zeta) \\ \phi &= \arcsin(|\zeta|)\end{aligned}$$

Where $\arg(\cdot)$ and $|\cdot|$ denote the argument and absolute value of a complex number, respectively.

2.2.4 Data Model ULA

Let $s_t(t)$ be the transmitted narrowband signal coming from the source. This signal can be expressed as

$$s_t(t) = A(t) \cdot \cos(2\pi f_c t + \psi(t))$$

where $A(t)$ and $\psi(t)$ represent the amplitude and phase of the modulated signal, respectively, while f_c denotes the carrier frequency of the signal. The narrowband assumption states that, for a small time delay τ, the amplitude and phase stay approximately the same. Mathematically, this implies that

$$\begin{aligned}\psi(t) &\approx \psi(t-\tau) \\ A(t) &\approx A(t-\tau)\end{aligned}$$

The complex signal representation of the transmitted signal $s_t(t)$ can be expressed as

$$\tilde{s}_t = A(t) \cdot e^{j\psi(t)} \cdot e^{j2\pi f_x t}$$

such that

$$s_t = \Re\left\{A(t) \cdot e^{j\psi(t)} \cdot e^{j2\pi f_c t}\right\}$$

where $\Re\{\cdot\}$ denotes the real part of the complex signal. In the equation, $A(t) \cdot e^{j\psi(t)} = \tilde{s}_{env}(t)$ is defined as the complex envelope also called the complex baseband equivalent representation of the signal. The narrowband assumption implies that a small delay τ only results in a phase offset in the complex envelope

$$\begin{aligned}\tilde{s}_t(t-\tau) &= A(t-\tau) \cdot e^{j\psi(t-\tau)} \cdot e^{j2\pi f_c(t-\tau)} \\ &\approx A(t) \cdot e^{j\psi(t)} \cdot e^{-j2\pi f_c\tau} \cdot e^{j2\pi f_c t} \\ &= \tilde{s}_{env}(t) \cdot e^{-j2\pi f_c\tau} \cdot e^{j2\pi f_c t}\end{aligned}$$

Before the signal impinges on the first element, the signal must travel a distance d_d. This will introduce a delay in the signal of $\tau_d = d_d/c$. Therefore, the complex signal received by the first element of the ULA array can be expressed as

$$\begin{aligned}\tilde{s}_1^r(t) &= \tilde{s}_t(t-\tau_d) \\ &= \tilde{s}_{env}(t-\tau_d)\cdot e^{j2\pi f_c(t-\tau_d)}\end{aligned}$$

The extra delay that the signal needs to travel to impinge on the ith antenna compared to the first antenna can be expressed as

$$\tau_i = (i-1)\frac{d\sin(\theta)}{c}$$

Consequently, the signal received by the ith element can be expressed as

$$\begin{aligned}\tilde{s}_i^r(t) &= \tilde{s}_1^r(t-\tau_i) \\ &\approx \tilde{s}_{env}(t-\tau_d)\cdot e^{-j2\pi f_c\tau_i}\cdot e^{j2\pi f_c(t-\tau_d)}\end{aligned}$$

Observe that $\frac{2\pi f_c d}{c}\sin(\theta) = \frac{2\pi d}{\lambda}\sin(\theta)$ is a constant if both the source and destination are stationary. Additionally, the wavelength λ and inter-element spacing d must remain constant.

Let the complex envelope signal received by the first element be defined as $s(t) = \tilde{s}_{env}(t-\tau_d)$. The complex envelope signals received by the M elements can be expressed in vector form as

$$\begin{aligned}\vec{x}(t) = \begin{bmatrix} x_1(t) \\ x_2(t) \\ \vdots \\ x_M(t)\end{bmatrix} &= s(t)\cdot\begin{bmatrix} 1 \\ e^{-j\frac{2\pi d}{\lambda}\sin(\theta)} \\ \vdots \\ e^{-j(M-1)\frac{2\pi d}{\lambda}\sin(\theta)}\end{bmatrix} \\ &= s(t)\cdot\vec{a}(\theta)\end{aligned}$$

The vector $\vec{a}(\theta)$ is also referred to as the array steering vector.

Let p be the number of sources that impinge on the antenna array at different angles with uncorrelated noise. For an M element array, the received complex envelope signals in vector form becomes

$$\begin{aligned}\vec{x}(t) &= \sum_{i=1}^{p}\vec{a}(\theta_i)\cdot s_i(t) + \vec{n}(t) \\ &= \boldsymbol{A}(\vec{\theta})\cdot\vec{s}(t) + \vec{n}(t)\end{aligned}$$

where $\boldsymbol{A}(\vec{\theta})$ is the $M\times p$ steering matrix with

$$\vec{\theta} = \begin{bmatrix}\theta_1 & \theta_2 & \cdots & \theta_p\end{bmatrix}$$

and

$$\boldsymbol{A}(\vec{\theta}) = \begin{bmatrix} \vec{a}(\theta_1) & \vec{a}(\theta_2) & \cdots & \vec{a}(\theta_p) \end{bmatrix}$$

The vectors $\vec{s}(t)$ and $\vec{n}(t)$ contain the p signal sources and the uncorrelated noise associated with the signal, respectively.

If the signals are sampled at $t = t_n$, each snapshot consists of M samples. Given N snapshots, the data model becomes

$$\begin{aligned} \boldsymbol{X} &= \begin{bmatrix} \vec{x}(t_1) & \vec{x}(t_2) & \cdot & \vec{x}(t_N) \end{bmatrix}^T \\ &= \begin{bmatrix} x_1(t_1) & x_2(t_1) & \cdots & x_M(t_1) \\ x_1(t_2) & x_2(t_2) & \cdots & x_M(t_2) \\ \vdots & \vdots & \ddots & \vdots \\ x_1(t_N) & x_2(t_N) & \cdots & x_M(t_N) \end{bmatrix} \end{aligned}$$

2.2.5 Data Model URA

The data model for a ULA can be extended to a URA to estimate both azimuth θ and elevation ϕ. The two-dimensional array consisting of $M_x \cdot M_y$ elements can be expressed in a comparable way. In an ideal scenario, the received data at $t = t_n$ on the array element (k_x, k_y) can be expressed as

$$x_{k_x,k_y}(t_n) = s(t_n) \cdot e^{-j(k_x-1)\frac{2\pi d_x}{\lambda}\cos(\theta)\sin(\phi)} \cdot e^{-j(k_y-1)\frac{2\pi d_y}{\lambda}\sin(\theta)\sin(\phi)}$$

As discussed, the received data depends on the phase offset in both directions. The data that is received at $t = t_n$ by the $M_x \cdot M_y$ antenna array can be represented as a matrix

$$\begin{aligned} \boldsymbol{T}(t_n) &= \begin{bmatrix} x_{1,1}(t_n) & x_{1,2}(t_n) & \cdots & x_{1,M_y}(t_n) \\ x_{2,1}(t_n) & x_{2,2}(t_n) & \cdots & x_{2,M_y}(t_n) \\ \vdots & \vdots & \ddots & \vdots \\ x_{M_x,1}(t_n) & x_{M_x,2}(t_n) & \cdots & x_{M_x,M_y}(t_n) \end{bmatrix} \\ &= s(t_n) \cdot \vec{a}_x(\theta,\phi) \cdot \vec{a}_y(\theta,\phi) \end{aligned}$$

Where $\vec{a}_x(\theta,\phi) \in \mathbb{C}^{M_x}$ and $\vec{a}_y(\theta,\phi) \in \mathbb{C}^{M_y}$ are the steering vectors in x- and y-direction, respectively. The steering vectors are defined as

$$\vec{a}_x(\theta,\phi) = \begin{bmatrix} 1 & e^{-j\frac{2\pi d_x}{\lambda}\cos(\theta)\sin(\phi)} & \ldots & e^{-j(M_x-1)\frac{2\pi d_x}{\lambda}\cos(\theta)\sin(\phi)} \end{bmatrix}^T$$

and

$$\vec{a}_y(\theta,\phi) = \begin{bmatrix} 1 & e^{-j\frac{2\pi d_y}{\lambda}\sin(\theta)\sin(\phi)} & \ldots & e^{-j(M_y-1)\frac{2\pi d_y}{\lambda}\sin(\theta)\sin(\phi)} \end{bmatrix}$$

respectively. Where $(\cdot)^T$ denotes the transpose.

Again, let p denote the number of sources. The data matrix considering uncorrelated noise at sample time $t = t_n$ becomes

$$\begin{aligned}\boldsymbol{T}(t_n) &= \sum_{i=1}^{p} \vec{a}_x(\theta_i, \phi_i) \cdot \vec{a}_y(\theta_i, \phi_i) \cdot s_i(t_n) + \boldsymbol{N}(t_n) \\ &= \boldsymbol{B}(\vec{\theta}, \vec{\phi}) \cdot \vec{s}(t_n) + \boldsymbol{N}(t_n)\end{aligned}$$

In this case, $\boldsymbol{B}(\vec{\theta}, \vec{\phi}) \in \mathbb{C}^{M_x \times M_y}$ and $\boldsymbol{N}(t_n) \in \mathbb{C}^{M_x \times M_y}$ are the steering matrix and noise matrix, respectively. For the two-dimensional array to be conform with the data model specified for a one-dimensional array, the $M_x \times M_y$ matrix must be translated to a single-column vector. The columns of the data matrix $\boldsymbol{T}(t_n)$ can be stacked column-wise using the vector mapping operator $vec\{\cdot\}$. As a result, the data column vector becomes

$$\vec{x}(t_n) = vec\{\boldsymbol{T}(t_n)\}$$

The same operation can be applied to the steering vector

$$\begin{aligned}\vec{a}(\theta_i, \phi_i) &= vec\{\boldsymbol{B}(\theta_i, \phi_i)\} \\ &= \vec{a}_y(\theta_i, \phi_i)^T \otimes \vec{a}_x(\theta_i, \phi_i)\end{aligned}$$

where the symbol $\otimes$ represents the Kronecker product.

The steering matrix $\boldsymbol{A}$ for the p impinging signals can be written as

$$\boldsymbol{A}(\vec{\theta}, \vec{\phi}) = \begin{bmatrix}\vec{a}(\theta_1, \phi_1) & \vec{a}(\theta_2, \phi_2) & \cdots & \vec{a}(\theta_p, \phi_p)\end{bmatrix}$$

Consequently, the data model for N samples becomes

$$\begin{aligned}\boldsymbol{X} &= \begin{bmatrix}\vec{x}(t_1) & \vec{x}(t_2) & \cdots & \vec{x}(t_N)\end{bmatrix}^T \\ &= \begin{bmatrix} x_{1,1}(t_1) & x_{2,1}(t_1) & \cdots & x_{M_x,1}(t_1) & x_{1,2}(t_1) & \cdots & x_{M_x,M_y}(t_1) \\ x_{1,1}(t_2) & x_{2,1}(t_2) & \cdots & x_{M_x,1}(t_2) & x_{1,2}(t_2) & \cdots & x_{M_x,M_y}(t_2) \\ \vdots & \vdots & \ddots & \vdots & \vdots & \ddots & \vdots \\ x_{1,1}(t_N) & x_{2,1}(t_N) & \cdots & x_{M_x,1}(t_N) & x_{1,2}(t_N) & \cdots & x_{M_x,M_y}(t_N)\end{bmatrix}\end{aligned}$$

Chapter 3

Capabilities of BLE and its Direction Finding Feature

The device whose position is to be estimated is referred to as a tag, while the device that performs the estimation is referred to as an anchor. The anchor has a known and fixed location, while the tag can be mobile and has an unknown location. The tag also has limited power, both in terms of energy and computation, and should be convenient to carry around.

The position estimation relies on receiving Bluetooth packets that contain a CTE. The rate at which these packets are received is termed as the update rate. The update rate relies on the communication mode, which is either connectionless or connection-oriented. Both of these mode will be examined in detail. Additionally, the unique configurations of tags and anchors will be discussed along with the relevant performance metrics.

3.1 Connectionless Mode

In connectionless mode, packets within a periodic advertising train may contain a CTE [6]. Such a train consists of advertisements transmitted at fixed intervals. The PDUs utilized for a sequence of advertisements in a periodic advertising train are *AUX_SYNC_IND* and *AUX_CHAIN_IND*. Where the latter PDU is capable of holding additional advertising data from the former. The *AUX_SYNC_IND* PDU may contain advertising data, a CTE, and a pointer to an *AUX_CHAIN_IND* PDU. The interval between the start of two consecutive packets containing the *AUX_SYNC_IND* PDU, also known as the periodic advertising interval, ranges from 7.5 ms to 81.91875 s with increments of 1.25 ms. Packets within the periodic advertising train can only be transmitted on the secondary advertising channels. The periodic advertising interval is fixed and cannot be altered while enabled. Additionally, two periodic events for the

same periodic advertising train must not overlap. The periodic advertising train with Bluetooth packets are illustrated in Figure 3.1

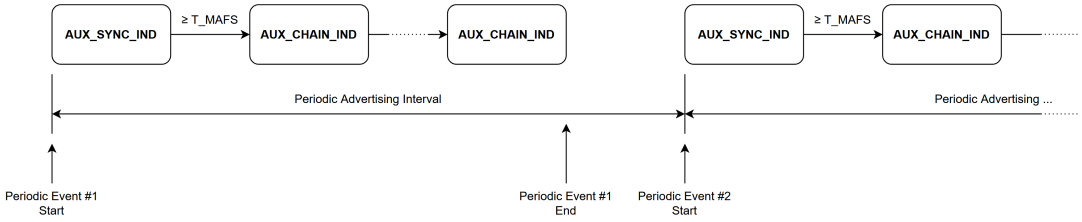

Figure 3.1: Periodic advertising interval

When a periodic event consists of multiple packets, the *AuxPtr* field is utilized to indicate the subsequent packet. The most important components of this field are the offset time and channel index. The offset time contained in the *AuxPtr* field is measured from the start of the packet containing the *AuxPtr* till the start of the packet it indicates. This offset time must be at least equal to the length of the packet plus the minimum AUX frame space (T_MAFS). T_MAFS is defined as the minimum time interval between a packet containing an *AuxPtr* and the auxiliary packet it indicates. This time is fixed at 300 µs. The auxiliary packet shall not be transmitted earlier than the offset time and no later than the offset time plus one offset unit. Where the offset unit is either 30 µs or 300 µs.

For a Bluetooth device to be able to synchronize with a periodic advertising train, at least one advertisement packet on the primary advertising channels is required. This packet shall have the *ADV_EXT_IND* PDU. During an advertising event, a maximum of one packet may be transmitted on each primary advertising channel. Afterwards, when in low duty cycle mode, the device needs to wait before transmitting other packets on the primary channels. The time between the start of two consecutive advertising events ($advEvent$) can be computed as follows

$$advEvent = advInterval + advDelay$$

The advertising interval ($advInterval$) can vary from 20 ms to 10,485.759375 s with increments of 0.625 ms. The advertising delay ($advDelay$) is a random value and shall be within the range 0 ms to 10 ms. Figure 3.2 provides an illustrative example of these advertising events.

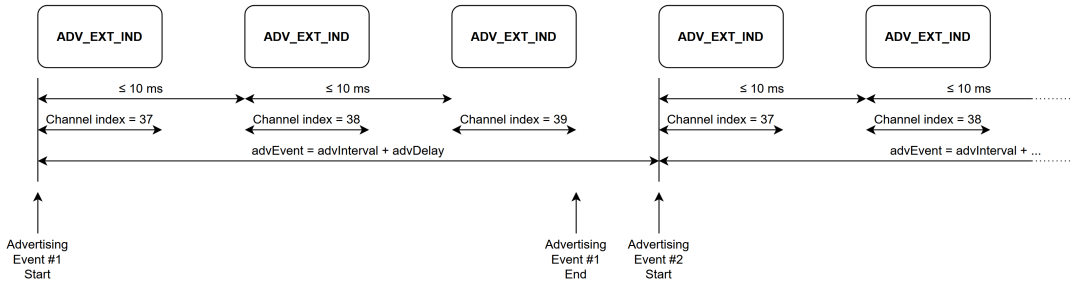

Figure 3.2: Advertising event

Each packet that contains an *ADV_EXT_IND* PDU also includes an *AuxPtr* field to point to the packet containing an *AUX_ADV_IND* PDU, as depicted in Figure 3.3. The advertising packets on the primary advertising channels point to the same *AUX_ADV_IND* PDU.

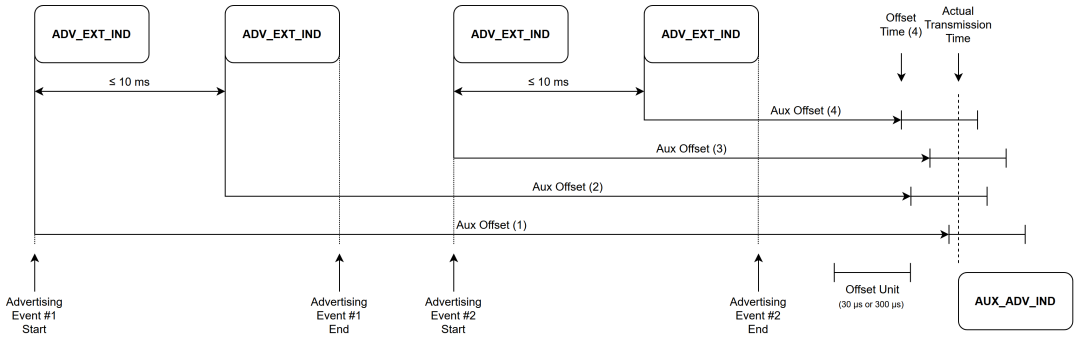

Figure 3.3: *AuxPtr* offset time

The *AUX_ADV_IND* packet on the other hand contains a *SyncInfo* field to point to the *AUX_SYNC_IND* PDU. Its structure is similar to the *AuxPtr* field and includes an offset time and offset unit. Additionally, it provides information about the interval of the periodic advertising train. This information is used to synchronize with said periodic advertising train. A detailed representation of offsets can be found in Figure 3.4.

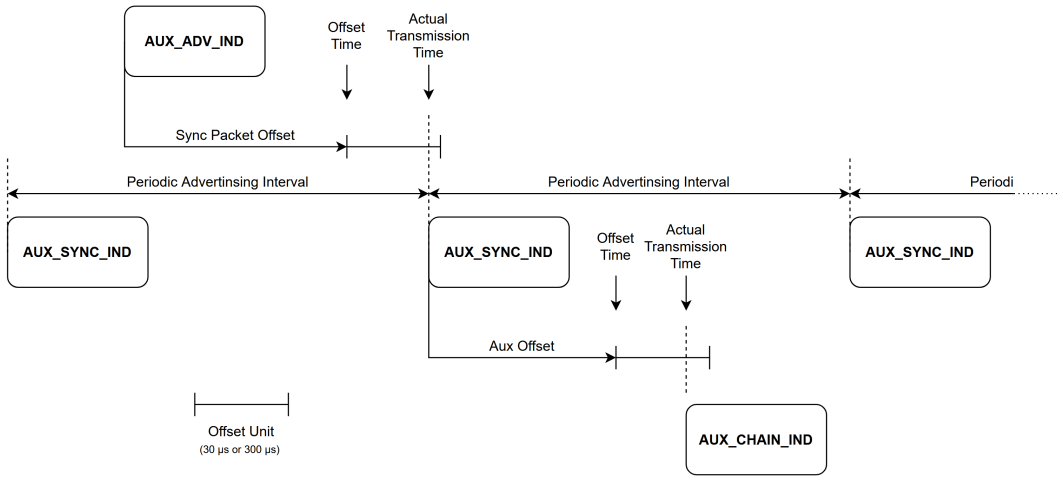

Figure 3.4: *SyncInfo* offset time

Every time the periodic advertising trains is enabled; it is required to transmit at least one *AUX_ADV_IND* PDU indicating the first *AUX_SYNC_IND* PDU of the periodic advertising train. Afterwards there is no obligation to transmit PDUs indicating subsequent packets in the periodic advertising train. The procedure for connecting with a periodic advertising train is illustrated in Figure 3.5.

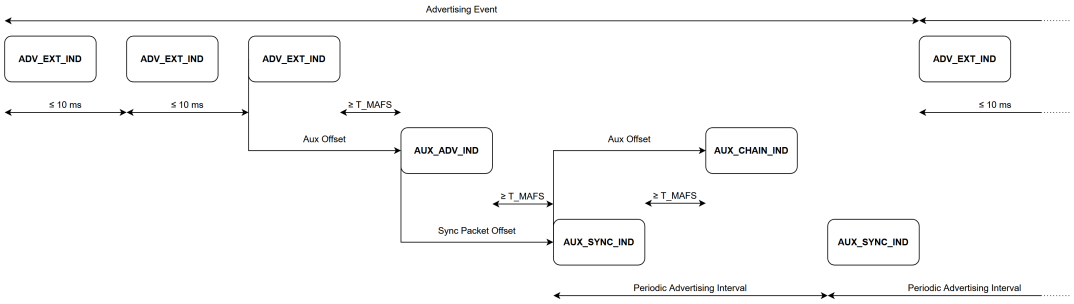

Figure 3.5: Periodic advertising train

During the configuration of the Bluetooth device enabling the connectionless mode, the number of packets containing a CTE can be specified. This allows for transmission of additional *AUX_CHAIN_IND* packets containing a CTE without the need of any additional data. If circumstances prevent the transmission of specified number of packets containing the CTE, the device should transmit as many packets as possible.

The information that is included in the packets containing a CTE consists of the length and type of CTE. The length of the CTE must be between 16 µs and 160 µs, in increments of 8 µs. The type of the CTE is determined by the direction finding method that is deployed. This can be either AoA or AoD. In the case of AoA, the master can specify the slot duration to be either 1 µs or 2 µs.

Concluding, when synchronized with a periodic advertising train, the minimum time between two packets that contain a CTE is the length of the packet plus the T_MAFS of 300 µs. If only packets containing the *AUX_SYNC_IND* PDU are used, the update rate is 7.5 ms at maximum.

3.2 Connection-Oriented Mode

In connection-oriented mode, first a connection between the Bluetooth devices must be established. There are two possibilities for establishing a connection. The first option is transmitting advertisement packets containing an *ADV_IND* or *ADV_DIRECT_IND* PDU on the primary channels. The initiator, the device which initiates the connection, will transmit a connect request (*CONNECT_IND*). This process is illustrated in Figure 3.6

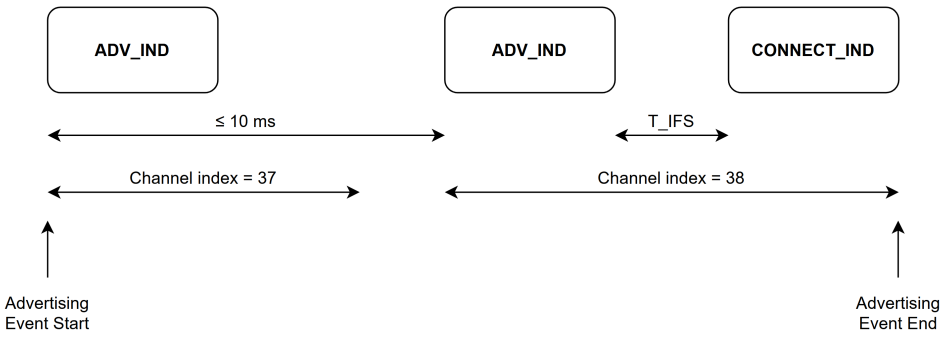

Figure 3.6: Connection advertisement using the primary channels

The second option is using the secondary channels for advertisement, which is similar to the procedure used in connectionless mode. Different advertising packets containing an *ADV_EXT_IND* PDU are transmitted on the primary advertising channels. These will point to the *AUX_ADV_IND* PDU. If the event type is connectable undirected or connectable directed, the initiator can transmit a connection request (*AUX_CONNECT_REQ* PDU). The connection is created when the initiator receives

a response packet (*AUX_CONNECT_RSP* PDU) from the advertiser. Both packets are transmitted on the same channel index and the delay between these packets is referred to as the inter frame space (T_IFS) and defined to be 150 µs. This process is illustrated in Figure 3.7

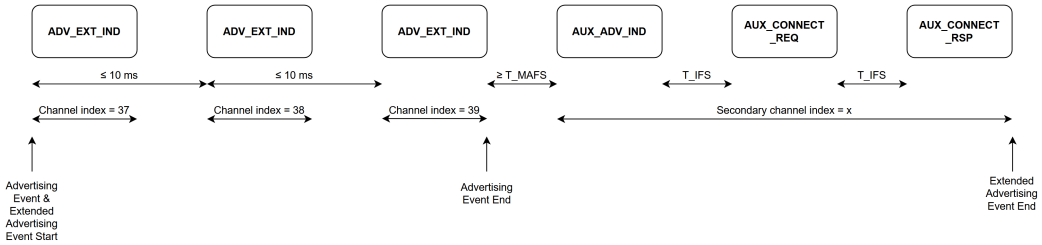

Figure 3.7: Connection advertisement using the secondary channels

In a connection two roles are defined: master and slave. The master is the device which initiated the connection while slave is the advertising device. The connection is only considered established once a data physical channel packet is received. During a connection request the master provides a connection interval and slave latency. These two parameters determine the timings of a connection event. The connection interval is defined to be in the range 7.5 ms to 4.0 s with steps of 1.25 ms. The slave latency allows the slave to skip consecutive connection events. This implies that the slave is nonobligatory to listen for the master each connection interval. During a connection event the same channel index shall be used and consists normally of at least one packet transmitted by the master. An example of the connection interval and packets between master and slave can be seen in Figure 3.8.

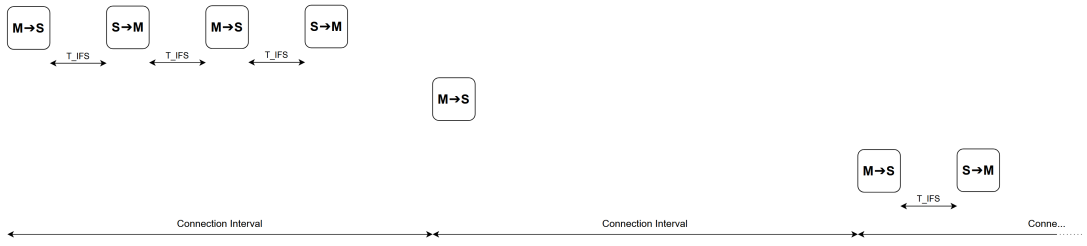

Figure 3.8: Connection interval

To obtain direction information, the master can request a CTE from the slave during a connection event using the *LL_CTE_REQ* PDU. The master can specify

two parameters: minimum length of the CTE and type of the CTE. The length of the CTE between must be between 16 µs and 160 µs, with increments of 8 µs. The type of the CTE depends on the deployed direction finding method, which is either AoA or AoD. In the case of AoD, the master can specify the slot duration to be either 1 µs or 2 µs. In response to the master device's request for a CTE, the slave will transmit a *LL_CTE_RSP* PDU with specified CTE parameters.

In summary, when a connection is established, the minimum time between two packets that contain a CTE is the sum of the lengths of a packet containing a *LL_CTE_REQ* PDU, a packet containing a *LL_CTE_RSP* PDU, and twice the T_IFS of 150 µs. If only a single packet can be transmitted during a connection interval, the maximum update rate is 7.5 ms.

3.3 Bluetooth Direction Finding Configurations

Various configurations can be implemented by utilizing the available direction finding methods and communication modes as shown in Table 3.1. Because the tag needs to be mobile and easy to carry, it mainly consists of a single antenna. Therefore, the anchor must consist of multiple antennas.

The process of computing the three-dimensional coordinates of the tag requires the involvement of multiple anchors. One possible method to be used is AoA, in which the tag transmits a CTE that can be simultaneously received and sampled by multiple anchors. The samples can be used to estimate the angles of the incoming signals, which are subsequently used to determine the three-dimensional position of the tag. The other possible method is AoD, in which the anchors transmit a CTE that is sampled by the tag. Since the tag has limited computational power, it cannot perform angle estimation by itself and has to transmit the samples to a central node for further processing. In this method, only the CTE of one anchor can be sampled at a time by the tag. This is undesired since the tag may move between the sampling of different anchors, resulting in inaccurate position estimation.

Two communication modes are available for the interaction between the anchors and tags. The first mode is connection-oriented, in which each anchor establishes a connection with every tag. This mode has the advantage of allowing the anchor to change the rate at which it requests the CTE from the tag. The disadvantage of this mode is that each anchor needs to keep track of the connection information of each tag such as connection interval and connection supervision timeout period. The second mode is connectionless, in which the tag broadcasts a CTE at a fixed periodic advertising interval. The anchors have to synchronize to such periodic advertising train. Depending on the required update rate, the anchor does not have to sample each packet from the tag. However, it needs to keep track of each packet in

order to determine the channel index of the next packet.

Table 3.1: Possible Bluetooth direction finding configurations

Config	Tag	Anchor	Method	Mode
1	Single antenna	Multiple antennas	AoA	Connectionless
2	Single antenna	Multiple antennas	AoA	Connection-oriented
3	Single antenna	Multiple antennas	AoD	Connectionless
4	Single antenna	Multiple antennas	AoD	Connection-oriented
5	Multiple antennas	Single antenna	AoA	Connectionless
6	Multiple antennas	Single antenna	AoA	Connection-oriented
7	Multiple antennas	Single antenna	AoD	Connectionless
8	Multiple antennas	Single antenna	AoD	Connection-oriented

3.4 Performance Metrics

The performance of indoor positioning systems depends on various metrics that reflect their quality and efficiency. One of these metrics is the scalability characteristic, which has two aspects: geographic scale and density scale. The geographic scale refers to the area that is covered by the system. This area is influenced by the number of anchors, the device characteristics, the presence of obstacles and other sources of interference. The device characteristics include factors such as the receiver sensitivity and transmission power. Using a ULA instead of a URA requires additional anchors to cover a given area. The density scale is a measure for the number of devices located per unit area within a time period. As the density of tags increases, the system performs more computations to estimate the angles, reducing its update rate. Moreover, increasing the number of tags will result in spectrum congestion. However, this is heavily dependent on the used configuration. The optimal scenario is for the tags to sample the CTE contained in the periodic advertising train and estimate the incident angle. This ensures that increasing the number of tags will not result in an increased utilization of the spectrum.

Cost is another metric that determines the quality and efficiency of indoor positioning systems. It depends on various factors such as money, time, space, weight, and energy. The money factor encompasses the cost of hardware and software components as well as operational expenses. For instance, the manufacturing cost of a URA is higher than that of a ULA due to its more complex design. However, a higher number of ULAs are required for determining the three-dimensional position

of a tag. Tags may have constraints on the weight and dimensions. For example, limiting the tags to consist of a single antenna will reduce the number of possible configurations. Energy is another crucial factor. Some tags require to operate on batteries for extensive periods of time. This will affect how frequently the tag can receive or transmit a packet, resulting in a lower update rate.

Chapter 4

Array Signal Processing Techniques

Array signal processing techniques are methods for determining the direction of incoming signals by using an array of antennas [12]. These techniques can be classified into two categories: spectral-based methods and parametric methods. Spectral-based methods use the spatial spectrum of the received signals to estimate the directions of multiple impinging signals. There are two types of spectral-based methods: beamforming and subspace methods. Beamforming uses a spatial filter to scan and measure the output power for each direction. Where the output power is proportional to the spatial spectrum of the received signals. Subspace methods on the other hand uses the eigenstructure of the spatial covariance matrix. The spatial covariance matrix can be decomposed into a signal subspace and noise subspace. The signal subspace is spanned by the eigenvectors corresponding to the largest eigenvalues, while the noise subspace is spanned by the eigenvectors corresponding to the smallest eigenvalues. The spatial spectrum is obtained by projecting a steering vector onto the noise subspace and measure its orthogonality. Parametric methods use a mathematical model to describe the relationship between the received signals and the unknown source angles. This usually requires solving an optimization problem to find the optimal value to fit the model for the given data. An overview of these techniques is shown in Figure 4.1.

4.1 Computational Complexity

Understanding the DoA estimation algorithms is an essential aspect of their analysis, particularly in terms of computational resources. The computational resources required to perform the calculations involved in theses algorithms are often measured in terms of their computational complexity. A common approach for describing their computational complexity is by measuring the number of operations or Floating Point Operations (FLOPs). This approach has several advantages, including being

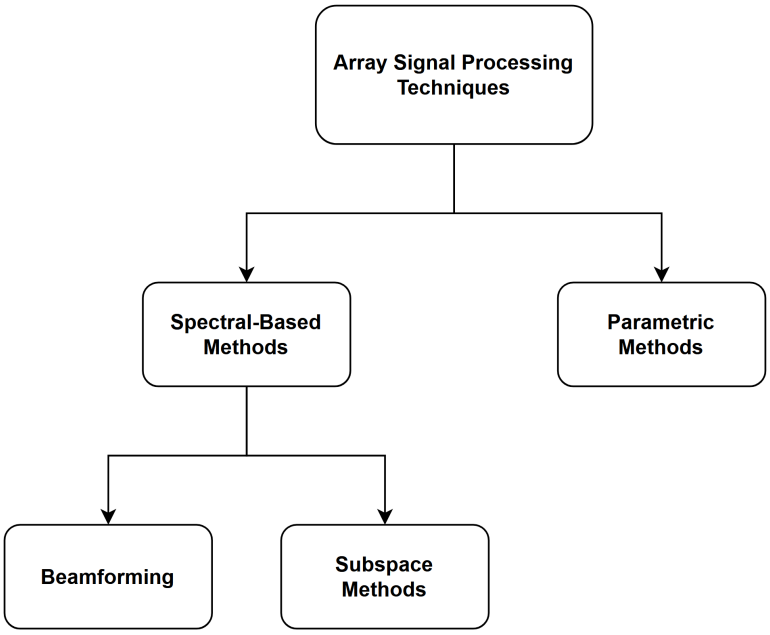

Figure 4.1: Overview of array signal processing techniques

independent of specific hardware and software, providing a consistent measure of complexity.

To apply this method, certain assumptions must be made concerning the execution time of basic arithmetic operations such as addition and multiplication. These operations are assumed to have a constant execution time. This assumption is not limited to real numbers but also extends to complex numbers. By expressing the complexity of DoA estimation algorithms in terms of FLOPs, it becomes possible to compare different algorithms and determine their relative efficiency. In the subsequent chapters, the derived data model will be referred to as $\boldsymbol{X}$.

The dimensions of this data model are dependent on the number of snapshots N and number of elements in the antenna array M. The rows of the data model span the number of snapshots, while the columns span the total number of antennas. For a URA, the total number of antennas is dependent on the number of antennas in the x- and y-direction, which are denoted M_x and M_y, respectively. The total number of elements is $M = M_x \cdot M_y$. The data model is said to be $\boldsymbol{X} \in \mathbb{C}^{N \times M}$.

Matrix Multiplication

Matrix multiplication is a fundamental operation in linear algebra and scientific computation. It is considered as one of the primary building blocks for a wide range of numeric algorithms that are used in various fields [13]. The efficiency with which

matrix multiplication is performed has a considerable impact on the computational complexity of these algorithms.

Given two matrices $\boldsymbol{A} \in \mathbb{C}^{i\times j}$ and $\boldsymbol{B} \in \mathbb{C}^{j\times k}$ of different lengths parameterized as

$$\boldsymbol{A} = \begin{bmatrix} a_{1,1} & a_{1,2} & \dots & a_{1,j} \\ a_{2,1} & a_{2,2} & \dots & a_{2,j} \\ \vdots & \vdots & \ddots & \vdots \\ a_{i,1} & a_{i,2} & \dots & a_{i,j} \end{bmatrix} \text{ and } \boldsymbol{B} = \begin{bmatrix} b_{1,1} & b_{1,2} & \dots & b_{1,k} \\ b_{2,1} & b_{2,2} & \dots & b_{2,k} \\ \vdots & \vdots & \ddots & \vdots \\ b_{i,1} & b_{i,2} & \dots & b_{i,k} \end{bmatrix}.$$

Their product $\boldsymbol{C} = \boldsymbol{AB}$ can be computed using the row multiplying column procedure. Each row of matrix $\boldsymbol{A}$ is multiplied by each column of matrix $\boldsymbol{B}$. For instance, the computation of the first index $c_{1,1}$ of the resulting matrix $\boldsymbol{C}$ is

$$c_{1,1} = a_{1,1}b_{1,1} + a_{1,2}b_{2,1} + \cdots + a_{1,j}b_{j,1}$$

This result includes j multiplications and $j-1$ additions. Repeating this procedure for each row of matrix $\boldsymbol{A}$ requires i iterations. Similarly, performing this operation for each column of matrix $\boldsymbol{B}$ takes k iterations. Consequently, the total number of operations consists of ijk multiplications and $ijk - ik$ additions, which results in a total of $2ijk - ik$ operations. In the event where the matrices are square, such that $i = j = k = n$, a total of n^3 multiplications and $n^3 - n^2$ additions are required. Hence a total of $2n^3 - n^2$ operations.

Transpose and Complex Conjugate

The complex conjugate of a complex number is defined as reversing the sign of the imaginary part. Given a complex number $z = a + bi$, the complex conjugate of z is often denoted by $\overline{z}$ and is mathematically expressed as

$$\overline{z} = a - bi$$

For matrices composed of complex numbers, the complex conjugate is defined as the element-by-element conjugate. The number of operations depends on the number of elements. Given a matrix $\boldsymbol{A} \in \mathbb{C}^{i\times j}$, a total of ij operations are required. For a square matrix $i = j = n$, the number of operations is n^2.

The transpose of matrix, denoted by $(\cdot)^T$, is defined as the operation of reflecting the matrix over its main diagonal. This results in an interchange of the row and column indices for each element in the matrix. Mathematically, this can be expressed as

$$\left[\boldsymbol{A}^T\right]_{i,j} = \left[\boldsymbol{A}\right]_{j,i}$$

Given an $i \times j$ matrix $\boldsymbol{A}$, a total of ij operations are required to transpose the matrix. Note that the position of the diagonal elements within the matrix remains

unchanged. Furthermore, two elements may be simultaneously interchanged given their respective row and column indices. The transpose of a square matrix only requires $\frac{n(n-1)}{2}$ operations. For non-square matrices, the number of operations is dependent on the dimensions of the matrix. Such a matrix can always be partitioned into two matrices, one square matrix and its remainder. If $i > j$, the number of operations is $\frac{j(j-1)}{2} + (i-j)\,j$. Conversely, if $i < j$, the number of operations is $\frac{i(i-1)}{2} + (j-i)\,i$.

The conjugate transpose or Hermitian transpose, denoted by $(\cdot)^H$, is defined as taking the complex conjugate of a matrix followed by its transpose. The number of operations required to perform this operation is the sum of the operations required for each individual step. For an $n \times n$ square matrix, this will result in $\frac{3}{2}n^2 - \frac{1}{2}n$ operations. For a non-square matrix with dimensions $i \times j$, this number is dependent on the dimensions. If $i > j$, the total number of operations is $2ij - \frac{1}{2}j^2 - \frac{1}{2}j$. Conversely, if $i < j$, the total number of operations is $2ij - \frac{1}{2}i^2 - \frac{1}{2}i$.

Matrix Multiplication with Hermitian Transpose

Some DoA estimation algorithms require the multiplication of a matrix with its Hermitian transpose. This can be expressed mathematically using two matrices $\boldsymbol{A} \in \mathbb{C}^{j \times i}$ and $\boldsymbol{B} \in \mathbb{C}^{j \times k}$ such that their product $\boldsymbol{C} = \boldsymbol{A}^H \boldsymbol{B}$. The procedure of taking a Hermitian transpose followed by matrix multiplication can be optimized. Rather than transposing the matrix prior to multiplication, the matrix can be transposed during the multiplication process. This entails switching the row and column indices during the indexing of a matrix. A similar approach can be employed for the complex conjugate, whereby the sign is inverted during multiplication. Applying these optimizations yields a total of $2ijk - ik$ operations, which is equivalent to matrix multiplication.

Matrix Inversion

Matrix inversion is a fundamental concept in the field of linear algebra. It involves the determination of the inverse of a matrix such that, when multiplied with the original matrix, the resulting product is the identity matrix. There exist several techniques for performing matrix inversion, one of which is using Gauss-Jordan elimination, also known as row reduction. This technique uses elementary row operations and requires $2n^3$ operations for an $n \times n$ square matrix $\boldsymbol{A}$ [14]. The resulting inverse matrix is commonly denoted as $\boldsymbol{A}^{-1}$.

Spatial Covariance Matrix

The calculation of the covariance matrix is an essential step in some DoA estimation algorithms. The signals received by the antenna array are often corrupted by noise. It is assumed that the noise sources at the elements have a zero mean and equal

variance. Additionally, the noise is considered to be uncorrelated, while the signal received by the antennas is correlated. This property can be exploited to obtain information about the direction of arrival of the signals. The covariance matrix of the data received by the antenna array is

$$\begin{aligned}\boldsymbol{R} &= \mathbb{E}\left[\vec{x}\left(t\right)\vec{x}^{H}\left(t\right)\right] \\ &= \boldsymbol{A}\boldsymbol{S}\boldsymbol{A}^{H} + \sigma_N^2\boldsymbol{I}\end{aligned}$$

Where $\mathbb{E}\left[\cdot\right]$ denotes the expectation and $\boldsymbol{S} = \mathbb{E}\left[\vec{s}\left(t\right)\vec{s}^{H}\left(t\right)\right]$ is the signal covariance matrix.

In practical applications, the estimation of the covariance matrix is limited by the availability of a finite number of snapshots. Given the predefined data model $\boldsymbol{X} \in \mathbb{C}^{N\times M}$, the spatial covariance matrix is defined as

$$\begin{aligned}\boldsymbol{R}_{xx} &\approx \frac{1}{N}\sum_{n=1}^{n}\vec{x}\left(t_n\right)\vec{x}^{H}\left(t_n\right) \\ &\approx \frac{1}{N}\boldsymbol{X}^{H}\boldsymbol{X}\end{aligned}$$

The process of computing the spatial covariance matrix involves several mathematical operations, including taking the Hermitian transpose, performing matrix multiplication, and multiplying the resulting matrix by a constant. The first two steps can be combined as previously discussed. The resulting matrix will be a square matrix with dimensions $M \times M$. The final step involves dividing each element by N, which requires M^2 operations. In total, the number of operations required to compute the spatial covariance matrix is $2M^2N$.

Eigendecomposition

Given an $n \times n$ square matrix $\boldsymbol{A}$, a vector $\vec{v}$ is considered an eigenvector if it satisfies the linear equation

$$\boldsymbol{A}\vec{v} = \lambda\vec{v}$$

Where λ is a scalar known as the eigenvalue corresponding to the eigenvector.

This equation is also referred to as the eigenvalue problem and can be solved for the eigenvalues using

$$\det\left(\boldsymbol{A} - \lambda\boldsymbol{I}\right) = 0$$

This results in an nth order characteristic polynomial. In this equation, $\boldsymbol{I}$ is an $n \times n$ identity matrix. Solving this characteristic polynomial yields less than or equal to n distinct solutions. The collection of eigenvalues is referred to as the spectrum of $\boldsymbol{A}$. For each eigenvalue λ_i, a specific eigenvalue equation exist

$$\left(\boldsymbol{A} - \lambda_i\boldsymbol{I}\right)\vec{v} = 0$$

If there are n distinct solutions, it follows that there are n linearly independent eigenvectors. Often the eigenvectors are normalized such that $\|\vec{v}\| = 1$. Where $\|\cdot\|$ denotes the norm or length.

The Abel-Ruffini theorem state that there is no algebraic solution to general polynomial equations of degree five or higher with arbitrary coefficients [15]. As a result, eigenvalue algorithms have been developed to find eigenvectors and eigenvalues. One such algorithm is the QR algorithm, which has been recognized as one of the top ten algorithms of the 20th century [16]. The QR algorithm is an iterative algorithm that requires $9n^3$ operations for an $n \times n$ square matrix [17].

4.2 Averaging

The Averaging (AVG) algorithm stands out for its simplicity. The basic idea behind this algorithm involves averaging the phase difference between the antenna elements. First, a mathematical explanation of the AVG algorithm is provided for a ULA, and this is subsequently extended to a URA. The complexity of this algorithm is then evaluated for each stage for both types of antenna arrays.

Given the predefined data model $\boldsymbol{X} \in \mathbb{C}^{N \times M}$ consisting of IQ samples. In this model, N is the number of snapshots, while M indicates the number of antenna elements in the ULA. The first step is obtaining the argument of each IQ sample in the data model. Given an IQ sample, the argument can be calculated as follows

$$\phi = \arg\left(\frac{Q}{I}\right)$$

Taking the argument of each element in the data model results in the matrix $\boldsymbol{X}_{\arg} \in \mathbb{C}^{N \times M}$, which is defined as

$$\boldsymbol{X}_{\arg} = \begin{bmatrix} \phi_1(t_1) & \phi_2(t_1) & \cdots & \phi_M(t_1) \\ \phi_1(t_2) & \phi_2(t_2) & \cdots & \phi_M(t_2) \\ \vdots & \vdots & \ddots & \vdots \\ \phi_1(t_N) & \phi_2(t_N) & \cdots & \phi_M(t_N) \end{bmatrix}$$

The phase difference between two consecutive antennas is dependent on the angle at which the signal impinges on the antenna array. The phase difference ϕ_{diff} of the ith element at sample time t_n in the matrix can be mathematically written as

$$\phi_{diff_i}(t_n) = \phi_{i+1}(t_n) - \phi_i(t_n), \quad 1 \leq i \leq M-1$$

Note that this will result in a matrix $\boldsymbol{X}_{diff} \in \mathbb{C}^{N \times (M-1)}$.

Next, the average phase difference of the samples can be computed. This average is computed over all the phase differences in a snapshot and subsequently over all the snapshots. Mathematically, this can be expressed as

$$AVG = \frac{1}{N\left(M-1\right)} \sum_{i=1}^{N} \sum_{j=1}^{M-1} \phi_{diff_j}\left(t_i\right)$$

The average phase difference can be used to obtain the angle at which the signal impinges on the antenna array. This angle can be calculated as follows

$$\theta = \arcsin\left(\frac{AVG \cdot \lambda}{2\pi d}\right)$$

The AVG algorithm for a ULA can be extended to a URA. For visualization purposes, the given data model $\boldsymbol{X} \in \mathbb{C}^{N \times M}$ is split into two separate data models, namely $\boldsymbol{X}_x$ and $\boldsymbol{X}_y$. Here, the total number of elements in the URA M is the product of the number of elements in each direction $M_x \cdot M_y$. Each snapshot in the original data model becomes a matrix. The dimensions of this matrix are dependent on the number of elements in the x- and y-direction. The dimensions are $M_x \times M_y$ and $M_y \times M_x$ for data model $\boldsymbol{X}_x$ and $\boldsymbol{X}_y$, respectively.

$$\boldsymbol{X}_x = \begin{bmatrix} \begin{bmatrix} \phi_{1,1}\left(t_1\right) & \phi_{2,1}\left(t_1\right) & \cdots & \phi_{M_x,1}\left(t_1\right) \\ \phi_{1,2}\left(t_1\right) & \phi_{2,2}\left(t_1\right) & \cdots & \phi_{M_x,2}\left(t_1\right) \\ \vdots & \vdots & \ddots & \vdots \\ \phi_{1,M_y}\left(t_1\right) & \phi_{2,M_y}\left(t_1\right) & \cdots & \phi_{M_x,M_y}\left(t_1\right) \end{bmatrix} \\ \vdots \\ \begin{bmatrix} \phi_{1,1}\left(t_N\right) & \phi_{2,1}\left(t_N\right) & \cdots & \phi_{M_x,1}\left(t_N\right) \\ \phi_{1,2}\left(t_N\right) & \phi_{2,2}\left(t_N\right) & \cdots & \phi_{M_x,2}\left(t_N\right) \\ \vdots & \vdots & \ddots & \vdots \\ \phi_{1,M_y}\left(t_N\right) & \phi_{2,M_y}\left(t_N\right) & \cdots & \phi_{M_x,M_y}\left(t_N\right) \end{bmatrix} \end{bmatrix}$$

$$\boldsymbol{X}_y = \begin{bmatrix} \begin{bmatrix} \phi_{1,1}\left(t_1\right) & \phi_{1,2}\left(t_1\right) & \cdots & \phi_{1,M_y}\left(t_1\right) \\ \phi_{2,1}\left(t_1\right) & \phi_{2,2}\left(t_1\right) & \cdots & \phi_{2,M_y}\left(t_1\right) \\ \vdots & \vdots & \ddots & \vdots \\ \phi_{M_x,1}\left(t_1\right) & \phi_{M_x,2}\left(t_1\right) & \cdots & \phi_{M_x,M_y}\left(t_1\right) \end{bmatrix} \\ \vdots \\ \begin{bmatrix} \phi_{1,1}\left(t_N\right) & \phi_{1,2}\left(t_N\right) & \cdots & \phi_{1,M_y}\left(t_N\right) \\ \phi_{2,1}\left(t_N\right) & \phi_{2,2}\left(t_N\right) & \cdots & \phi_{2,M_y}\left(t_N\right) \\ \vdots & \vdots & \ddots & \vdots \\ \phi_{M_x,1}\left(t_N\right) & \phi_{M_x,2}\left(t_N\right) & \cdots & \phi_{M_x,M_y}\left(t_N\right) \end{bmatrix} \end{bmatrix}$$

Note that each matrix associated with a snapshot in $\boldsymbol{X}_y$ is the transposed version of corresponding matrix in $\boldsymbol{X}_x$, and vice versa. The first step is to compute the

argument of each IQ samples in the original data model. Afterwards, the phase difference between two consecutive antennas is taken. It is important that the phase difference has to be taken in the x- and y-direction, resulting into two matrices.

Afterwards, the average for the two matrices can be computed

$$AVG_x = \frac{1}{NM_y\left(M_x - 1\right)} \sum_{i=1}^{N} \sum_{j=1}^{M_y} \sum_{k=1}^{M_x - 1} \phi_{diff_{j,k}}\left(t_i\right)$$

$$AVG_y = \frac{1}{NM_x\left(M_y - 1\right)} \sum_{i=1}^{N} \sum_{j=1}^{M_x} \sum_{k=1}^{M_y - 1} \phi_{diff_{j,k}}\left(t_i\right)$$

Using these averages, the azimuth and elevation can be calculated using

$$\mu = \frac{AVG_x \cdot \lambda}{2\pi d_x}$$

$$\nu = \frac{AVG_y \cdot \lambda}{2\pi d_y}$$

$$\zeta = \mu + \nu j$$

such that

$$\theta = \arg\left(\zeta\right)$$

$$\phi = \arcsin\left(|\zeta|\right)$$

4.2.1 Computational Complexity AVG

The AVG algorithm for a ULA can be summarized using four distinctive steps. The initial step is taken the argument of each element in the data model. Since each snapshot in the data model consists of M antenna elements and the matrix consists of a total of N snapshots, the number of operations required is NM. The second step is to calculate the phase difference between two consecutive antennas. This will result in $N\left(M-1\right)$ subtract operations. The third step is taking the average of each snapshot resulting in a total of M arithmetic operations. More specific, this consists of $M-1$ subtractions and one division. As this process needs to be performed for each snapshot, this results in $NM+1$ operations. The last step is calculating the angle. This consists of two multiplications, one division and one inverse trigonometric function. The steps and their complexity are summarized in Table 4.1.

Table 4.1: Computational complexity AVG ULA

Algorithm 1: AVG ULA Procedure	
1. Get arguments	NM
2. Obtain phase difference in each direction	$NM - N$
3. Averaging of each direction	$NM + 1$
4. Calculate azimuth and elevation	4
Total complexity:	$3NM - N + 5$

The AVG algorithm for a URA can be summarized again using the four distinctive steps. The first step is computing the argument of each element in the data model. Given that each snapshot in the data model consists of $M_x \cdot M_y = M$ antenna elements and the matrix includes a total of N snapshots, the number of operations required is NM. The second step is calculating the phase difference in each direction. Starting with the x-direction, the operation count for calculating the phase difference equals $NM_yM_x - NM_y$. The same applies for the y-direction, which equals $NM_xM_y - NM_x$. This results in a total of $2NM_xM_y - N(M_x + M_y)$ arithmetic operations. The third step is computing the average in each direction. For the x-direction, first $M_x - 1$ additions and one division are performed, resulting in M_x operations. This procedure is then repeated for each partial array in the antenna array, resulting in M_yM_x+1 operations. Finally, this procedure is performed for every snapshot, resulting in NM_yM_x+N+1. The same applies for the y-direction resulting in the same number of operations. To calculate the average in both directions, the number of operations required is $2NM_yM_x + 2N + 2$. The final step is to determine the azimuth and elevation. This requires four multiplications, two divisions and two inverse trigonometric functions and one modulus. A summary of these steps and their complexity can be found in Table 4.2.

Table 4.2: Computational complexity AVG URA

Algorithm 1: AVG URA Procedure	
1. Get arguments	NM
2. Obtain phase difference in each direction	$2NM - N\left(M_x + M_y\right)$
3. Averaging of each direction	$2NM + 2N + 2$
4. Calculate azimuth and elevation	9
Total complexity:	$5NM - N\left(M_x + M_y - 2\right) + 11$

4.3 Minimum Variance Distortionless Response

The Minimum Variance Distortionless Response (MVDR) beamforming, also known as Capon beamforming, was introduced in 1969 [18]. This method aims to minimize noise and spectral leakage from signals impinging from undesired angles, while maintaining a fixed gain in the desired direction. This is achieved by designing a weight vector, denoted as $\vec{w}$, which is used to linearly combine the received data $x\left(t_n\right)$ at time $t = t_n$ from an antenna array to form a single output signal:

$$y\left(t\right) = \vec{w}^H x\left(t\right)$$

The total averaged output power from an antenna array over N snapshots can be expressed as

$$\begin{aligned} P\left(\vec{w}\right) &= \frac{1}{N}\sum_{n=1}^{N}\left|y\left(t_n\right)\right|^2 \\ &= \vec{w}^H \boldsymbol{R} \vec{w} \end{aligned}$$

The weight vector is chosen such that it minimizes the average output power, or in other words, minimizes the variance, while maintaining a unity gain in the looking direction [19]. The looking direction is represented by the steering vector $\vec{a}\left(\theta\right)$. This minimization can be written as

$$\min_w \left\{P\left(\vec{w}\right)\right\} \text{ subject to } \vec{w}^H \vec{a}\left(\theta\right) = 1$$

such that the resulting weight vector is given by

$$\vec{w}_{MVDR} = \frac{\boldsymbol{R}^{-1}\vec{a}\left(\theta\right)}{\vec{a}^H\left(\theta\right)\boldsymbol{R}^{-1}\vec{a}\left(\theta\right)}$$

By substituting the optimal weight vector into the averaged output power, the spatial power spectrum becomes

$$P_{MVDR}(\theta) = \frac{1}{\vec{a}^H(\theta) R^{-1} \vec{a}(\theta)}$$

Figure 4.2 presents the MVDR spectrum for a ULA. It is constructed using a snapshot count of 100, a Signal-to-Noise Ratio (SNR) of 25 dB, and a ULA consisting of four elements. The spectrum features three incident angles, specifically -50°, 25°, and 60°.

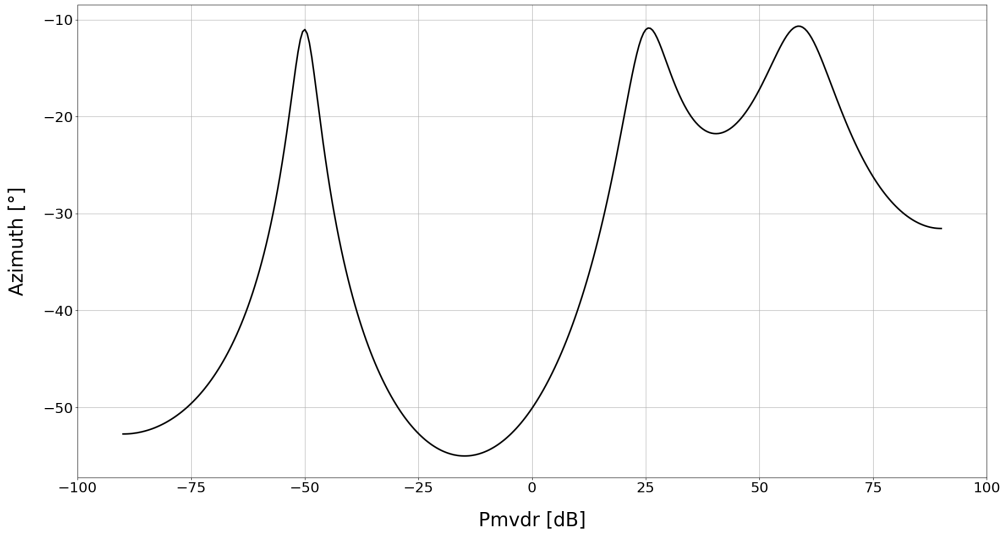

Figure 4.2: MVDR spectrum for a ULA

Capon's beamformer can be extended to a URA in order to obtain both the azimuth and elevation. The key distinction is that the steering vector $\vec{a}(\theta, \phi)$ is dependent on both the azimuth θ and elevation ϕ. As a result, the spatial power spectrum becomes

$$P_{MVDR}(\theta, \phi) = \frac{1}{\vec{a}^H(\theta, \phi) \boldsymbol{R}^{-1} \vec{a}(\theta, \phi)}$$

Figure 4.3 presents the MVDR spectrum, which is constructed using a snapshot count of 100, a SNR of 25 dB, and a four by four URA. The spectrum reveals three distinct incident angles. These angles, presented in the format (azimuth, elevation), are as follows: (45°, 75°), (-90°, 60°), and (-165°, 30°).

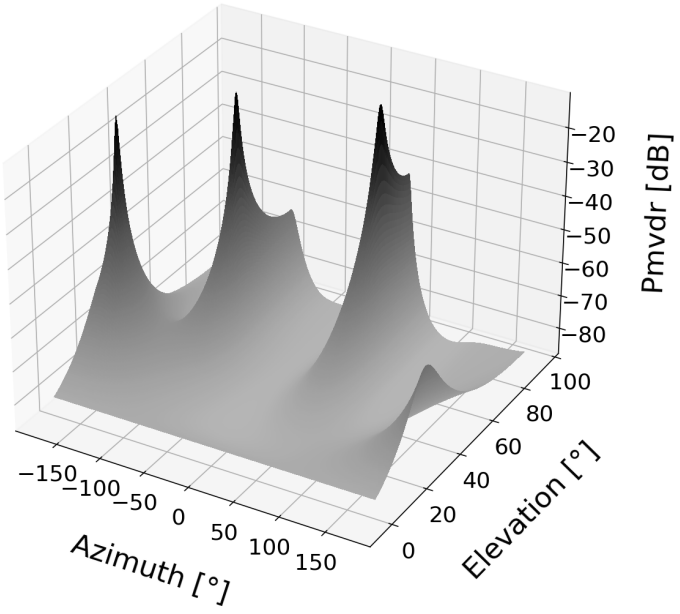

Figure 4.3: MVDR spectrum for a URA

4.3.1 Computational Complexity MVDR

The MVDR algorithm can be summarized using four distinctive steps. The first step is calculating the spatial covariance matrix R. Given the data model $\boldsymbol{X} \in \mathbb{C}^{N \times M}$, the required number of operations is $2M^2N$. The resulting dimensions of the spatial covariance matrix is $M \times M$. The second step requires calculating the inverse of the spatial covariance matrix. Using the Gaussian elimination method, this requires approximately $2M^3$ arithmetic operations. The third step is computing the spatial power spectrum. This requires the construction of a steering vector $\vec{a}\,(\theta) \in \mathbb{C}^M$, resulting in M operations. The number of operations required for matrix multiplication calculating $\vec{a}^H\,(\theta)\,\boldsymbol{R}^{-1}\vec{a}\,(\theta)$ is $2M^2+M-1$. Taking division into account, the spectrum obtained using MVDR requires $2M^2 + 2M$ operations.

The last step is finding the peaks corresponding to the p impinging signals in the MVDR spectrum. One of such algorithms which can be used is linear search. The resolution of the spectrum is dependent on the stepsize δ. For a ULA, the incident angle is in the interval $[-90°, 90°]$. This implies that the spectrum of the MVDR algorithm must be evaluated approximately $\frac{180}{\delta}$ times. For detecting a single impinging signal, the maximum power can be tracked. However, to detect multiple impinging signals, additional criteria must be established. In the case of Bluetooth direction finding only one signal is considered to impinge the antenna array at a given time.

Table 4.3: Computational complexity MVDR for a ULA

Algorithm 2: MVDR ULA Procedure	
1. Calculate covariance matrix	$2M^2N$
2. Inversion of the covariance matrix	$2M^3$
3. Compute the MVDR spectrum	$2M^2 + 2M$
4. Find peaks	$\frac{360M^2+360M}{\delta}$
Total complexity:	$2M^3 + M^2\left(\frac{360}{\delta} + 2N\right) + \frac{360}{\delta}M$

The same procedure can be taken to obtain the MVDR spectrum using a URA. The main differences are the steering vector and the angle interval of the impinging signals. A URA can be used to determine two angles; azimuth θ and elevation ϕ. Constructing a steering vector $\vec{a}\,(\theta, \phi) \in \mathbb{C}^M$, which still consists of M elements, results in $2M$ operations. The interval of the two angles are $(-180°, 180°]$ and $[0°, 90°]$ for the azimuth and elevation respectively. Using linear search and a stepsize of δ, the spectrum must be evaluated $\frac{32400}{\delta}$ times.

Table 4.4: Computational complexity MVDR for a URA

Algorithm 2: MVDR URA Procedure	
1. Calculate covariance matrix	$2M^2N$
2. Inversion of the covariance matrix	$2M^3$
3. Compute the MVDR spectrum	$2M^2 + 2M$
4. Find peaks	$\frac{64800M^2+64800M}{\delta}$
Total complexity:	$2M^3 + M^2\left(\frac{64800}{\delta} + 2N\right) + \frac{64800}{\delta}M$

4.4 Multiple Signal Classification

The MUltiple SIgnal Classification (MUSIC) algorithm was proposed by Schmidt [20]. The algorithm relies on the decomposition of the spatial covariance matrix into a signal subspace and noise subspace using eigendecomposition. It exploits the orthogonality property to isolate the signal and noise subspaces [21].

Consider an ULA consisting of M antennas with p impinging signals. The spatial covariance matrix $\boldsymbol{R}$ corresponding to the data model can be expressed as

$$\boldsymbol{R} = \boldsymbol{A}\boldsymbol{S}\boldsymbol{A}^H + \boldsymbol{N}$$

where $\boldsymbol{S}$ is the signal correlation matrix, $\boldsymbol{N}$ is the noise correlation matrix and $\boldsymbol{A}$ is the array steering matrix. The noise correlation matrix can also be expressed in terms of the noise variance as $\sigma_N^2\boldsymbol{I}$. The spatial covariance matrix can be decomposed in M eigenvalues, where the largest p eigenvalues correspond to the signal subspace while the other $M-p$ eigenvalues represent the noise subspace. Given the eigenvalues $\{\lambda_1, \cdots, \lambda_M\}$ it can be stated that

$$\det\left(\boldsymbol{R} - \lambda_i\boldsymbol{I}\right) = 0$$

Substitution of the spatial covariance matrix results in

$$\det\left(\boldsymbol{A}\boldsymbol{S}\boldsymbol{A}^H + \sigma_N^2\boldsymbol{I} - \lambda_i\boldsymbol{I}\right) = 0$$

If $\boldsymbol{A}\boldsymbol{S}\boldsymbol{A}^H$ has the eigenvalues e_i, then it can be stated that

$$e_i = \lambda_i - \sigma_N^2$$

The steering vectors that make up the steering matrix $\boldsymbol{A}$ are linearly independent. In other words, the steering matrix is full column rank. When $\boldsymbol{S}$ is nonsingular and the number of incident signals p is less than the number of elements M, it is guaranteed that the matrix $\boldsymbol{A}\boldsymbol{S}\boldsymbol{A}^H$ is positive semidefinite with rank p. This implies that $M-p$ of the eigenvalues e_i of $\boldsymbol{A}\boldsymbol{S}\boldsymbol{A}^H$ are zero. Consequently, the $M-p$ eigenvalues of $\boldsymbol{R}$ are equal to the noise variance σ_N^2. Note that the signal correlation matrix is nonsingular as long as the incident signals are not highly correlated [22].

For the eigenvectors $\vec{q}_i$ associated with the $M-p$ smallest eigenvalues it can be stated that $\boldsymbol{A}^H q_i = 0$. The eigenvectors are therefore orthogonal to the p steering vectors that compose $\boldsymbol{A}$. Let $\boldsymbol{V}_n$ be the eigenvectors corresponding to the noise subspace

$$\boldsymbol{V}_n = \begin{bmatrix} \vec{q}_{p+1} & \cdots & \vec{q}_M \end{bmatrix}$$

Since the steering vectors corresponding to the signal components are orthogonal to the noise subspace eigenvectors, $\vec{a}\left(\theta\right)\boldsymbol{V}_n\boldsymbol{V}_n^H\vec{a}\left(\theta\right) = 0$, for $\theta = \theta_i$. The MUSIC

spectrum can be constructed taking the inverse

$$P_{MUSIC}(\theta) = \frac{1}{\vec{a}(\theta)\boldsymbol{V}_n\boldsymbol{V}_n^H\vec{a}(\theta)}$$

Figure 4.4 presents the MUSIC spectrum for a ULA. It is constructed using a snapshot count of 100, a SNR of 25 dB, and a ULA consisting of four elements. The spectrum features three incident angles, specifically -50°, 25°, and 60°.

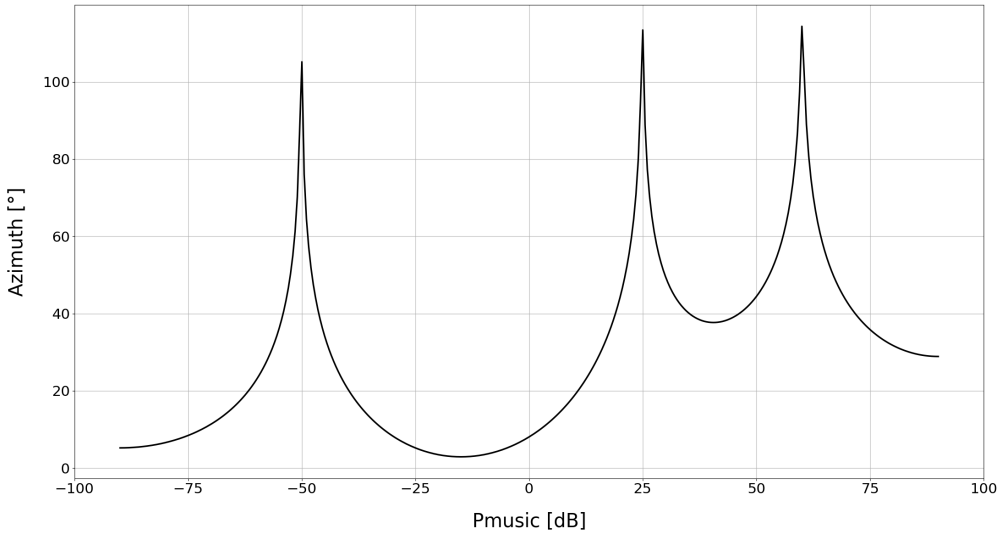

Figure 4.4: MUSIC spectrum for a ULA

The MUSIC algorithm can be extended to a URA in order to obtain the azimuth and elevation [23]. The steering vector for a URA is dependent on the azimuth and elevation. For this reason, the MUSIC spectrum becomes

$$P_{MUSIC}(\theta,\phi) = \frac{1}{\vec{a}^H(\theta,\phi)\boldsymbol{V}_n\boldsymbol{V}_n^H\vec{a}(\theta,\phi)}$$

Figure 4.5 presents the MUSIC spectrum, which is constructed using a snapshot count of 100, a SNR of 25 dB, and a four by four URA. The spectrum reveals three distinct incident angles. These angles, presented in the format (azimuth, elevation), are as follows: (45°, 75°), (-90°, 60°), and (-165°, 30°).

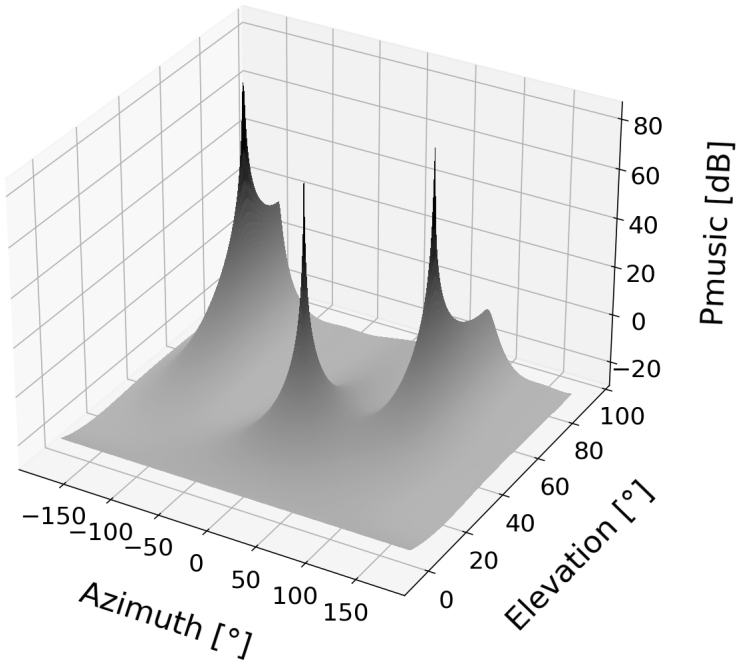

Figure 4.5: MUSIC spectrum for a URA

4.4.1 Computational Complexity MUSIC

The MUSIC algorithm for a ULA can be summarized using five distinctive steps. The first step is calculating the spatial covariance matrix $\boldsymbol{R}$. Given a data model $\boldsymbol{X} \in \mathbb{C}^{N \times M}$, the required number of operations is $2M^2N$. The second step is to decompose the spatial covariance matrix into its eigenvalues and eigenvectors. Using the QR algorithm, this will result in $9M^3$ operations. The third step is to compute the MUSIC spectrum. This step can be further divided into two smaller steps. The first of these involves multiplying the noise subspace $\boldsymbol{V}_n \in \mathbb{C}^{M \times p}$ with its Hermitian transpose, $\boldsymbol{V}_n \boldsymbol{V}_n^H \in \mathbb{C}^{M \times M}$. This will result in M^2p operations. Afterwards the MUSIC spectrum can be calculated. This requires the construction of a steering vector $\vec{a}\,(\theta) \in \mathbb{C}^M$, resulting in M operations. The number of operations required for matrix multiplication calculating $\vec{a}\,(\theta)\, \boldsymbol{V}_n \boldsymbol{V}_n^H \vec{a}\,(\theta)$ is $2M^2 + M - 1$. The same steering vector can be used during the matrix multiplication. Accounting for the division, calculating the MUSIC spectrum result in a total of $2M^2 + 2M$ operations.

The last step is finding the peaks corresponding to the p impinging signals in the MUSIC spectrum. Similar to the MVDR, linear search can be used to track the maximum value. Given the stepsize δ and the interval $[-90°, 90°]$ for a ULA, the MUSIC algorithm must be evaluated approximately $\frac{180}{\delta}$ times.

Table 4.5: Computational complexity MUSIC for a ULA

Algorithm 3: MUSIC ULA Procedure	
1. Calculate covariance matrix	$2M^2N$
2. Eigenvalue decomposition	$9M^3$
3. Eigenvector multiplication	M^2p
4. Compute the MUSIC spectrum	$2M^2 + 2M$
5. Find peaks	$\frac{360M^2+360M}{\delta}$
	Total complexity: $9M^3 + M^2\left(\frac{360}{\delta} + 2N + p\right) + \frac{360}{\delta}M$

The same procedure can be performed for computing the MUSIC spectrum using a URA. Similar to the MVDR, the primary distinctions are the steering vector and the interval of the incident angle. Constructing a steering vector $\vec{a}\,(\theta, \phi) \in \mathbb{C}^M$, which still consists of M elements, results in $2M$ operations. The interval of the two angles are $(-180°, 180°]$ and $[0°, 90°]$ for the azimuth and elevation respectively. Using linear search and a stepsize of δ, the spectrum must be evaluated $\frac{32400}{\delta}$ times.

Table 4.6: Computational complexity MUSIC for a URA

Algorithm 3: MUSIC URA Procedure	
1. Calculate covariance matrix	$2M^2N$
2. Eigenvalue decomposition	$9M^3$
3. Eigenvector multiplication	M^2p
4. Compute the MUSIC spectrum	$2M^2 + 2M$
5. Find peaks	$\frac{64800M^2+64800}{\delta}$
	Total complexity: $9M^3 + M^2\left(\frac{64800}{\delta} + 2N + p\right) + \frac{64800}{\delta}M$

4.5 Estimation of Signal Parameters via Rotational Invariance Techniques

The Estimation of Signal Parameters via Rotational Invariant Techniques (ESPRIT) algorithm was introduced in 1986 [24]. It is classified as a parametric method and falls under the category of subspace-based methods. The fundamental concept of the algorithm is based on the presence of identical subarrays. The spacing between these subarrays is known and their structure is identical, thus satisfying the condition of rotational invariance in space.

The data model employed in the ESPRIT algorithm differs from predefined data model. Specifically, the data model used for the ESPRIT algorithm is a transposed version. This entails that the rows denote the number of antennas and the columns denote the number of snapshots. The subspace is estimated based on the covariance approach of $\boldsymbol{X}\boldsymbol{X}^H$, which corresponds to $\boldsymbol{X}^T\overline{\boldsymbol{X}}$ for the predefined data model.

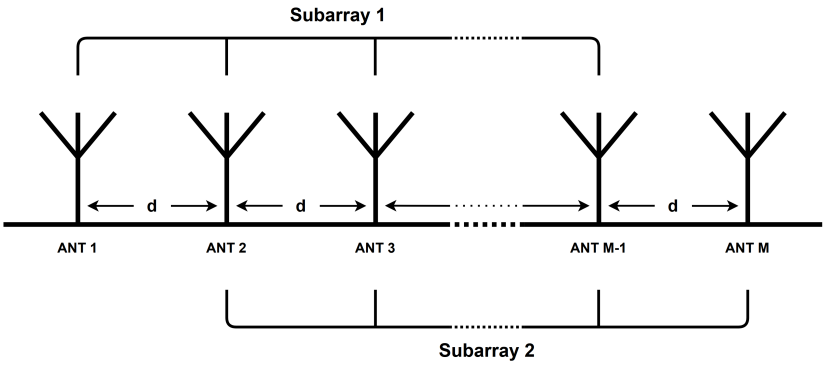

Figure 4.6: Subarrays ULA

Consider a ULA consisting of M elements, with p representing the number of signals impinging on the array. Various subarray configurations are suitable for ESPRIT. The subarrays may overlap and an antenna may be a member of both subarrays. The subarray with maximum overlap is used, such that each subarray contains $m = M - 1$ antennas as illustrated in Figure 4.6. The selection matrices for the subarrays can be given by

$$\boldsymbol{J}_1 = \begin{bmatrix} \boldsymbol{I}_m & \mathbf{0} \end{bmatrix} \in \mathbb{R}^{m \times M}$$

and

$$\boldsymbol{J}_2 = \begin{bmatrix} \mathbf{0} & \boldsymbol{I}_m \end{bmatrix} \in \mathbb{R}^{m \times M}$$

The selection matrix $\boldsymbol{J}_1$ is used to select the first m rows of the array steering matrix $\boldsymbol{A}(\vec{\theta})$, while $\boldsymbol{J}_2$ is used to select the last m rows. Due to the fixed displacement

between the two subarrays, the array steering vector of the second array $\boldsymbol{J}_2\vec{a}\left(\theta_i\right)$ is a scaled version of the array steering vector of the first subarray $\boldsymbol{J}_1\vec{a}\left(\theta_i\right)$. This can be expressed as

$$\boldsymbol{J}_1\vec{a}\left(\theta_i\right)e^{-j\frac{2\pi d}{\lambda}\sin(\theta_i)} = \boldsymbol{J}_2\vec{a}\left(\theta_i\right), \quad 1 \leq i \leq k$$

The shift-invariance property for all array steering vectors $\vec{a}\left(\theta_i\right)$ can be expressed in a compact matrix form as

$$\boldsymbol{J}_i\boldsymbol{A}\boldsymbol{\Phi} = \boldsymbol{J}_2\boldsymbol{A}$$

where $\boldsymbol{\Phi}$ represents a $p \times p$ diagonal matrix with the values $\begin{bmatrix} e^{-j\frac{2\pi d}{\lambda}\sin(\theta_1)} & \cdots & e^{-j\frac{2\pi d}{\lambda}\sin(\theta_p)} \end{bmatrix}$ on the main diagonal. These elements contain the desired direction of arrival information in their phases.

Analogous to the MUSIC algorithm, the covariance matrix can be decomposed into two distinct subspaces: the noise subspace and the signal subspace. The signal subspace is characterized by the p largest eigenvalues, while the remaining eigenvalues associated with the noise subspace. Let us denote the eigenvectors $\vec{q}_i$ that correspond to the signal subspace as $\boldsymbol{V}_s$. Thus, the signal subspace can be expressed as

$$\boldsymbol{V}_s = \begin{bmatrix} \vec{q}_i & \cdots & \vec{q}_p \end{bmatrix}$$

The columns of the array steering matrix $\boldsymbol{A}(\vec{\theta})$ span the p-dimensional signal subspace. As a result, there exists a nonsingular $p \times p$ matrix $\boldsymbol{T}$ such that $\boldsymbol{A} = \boldsymbol{V}_s\boldsymbol{T}$ is satisfied. This allows for the expression of the shift-invariance property in terms of the eigenvectors corresponding to the signal subspace as

$$\boldsymbol{J}_1\boldsymbol{V}_s\boldsymbol{T}\boldsymbol{\Phi} = \boldsymbol{J}_2\boldsymbol{V}_s\boldsymbol{T} \leftrightarrow \boldsymbol{J}_1\boldsymbol{V}_s\boldsymbol{\Psi} = \boldsymbol{J}_2\boldsymbol{V}_s$$

where $\boldsymbol{\Psi} \in \mathbb{C}^{p\times p}$ is the signal subspace rotating operator. The eigenvalues of the subspace rotating operator can be determined through its eigendecomposition, as it satisfies

$$\boldsymbol{\Psi} = \boldsymbol{T}\boldsymbol{\Phi}\boldsymbol{T}^{-1}$$

Consequently, the eigenvalues of $\boldsymbol{\Psi}$ represent estimates of the phase factors $e^{-j\frac{2\pi d}{\lambda}\sin(\theta_i)}$. Once these estimates have been obtained, the corresponding values of θ_i can be determined via the relationships

$$\alpha_i = \arg\left(e^{-j\frac{2\pi d}{\lambda}\sin\left(\theta_i\right)}\right) \text{ and } \theta_i = \arcsin\left(-\frac{\lambda}{2\pi d}\alpha_i\right), \quad 1 \leq i \leq p$$

The ESPRIT algorithm can be extended to accommodate a URA for the purpose of obtaining both azimuth and elevation [25]. Once again, it is necessary to transpose the predefined data model for a URA. Let us consider a URA that is composed of $M = M_x \cdot M_y$ antennas, with p impinging signals.

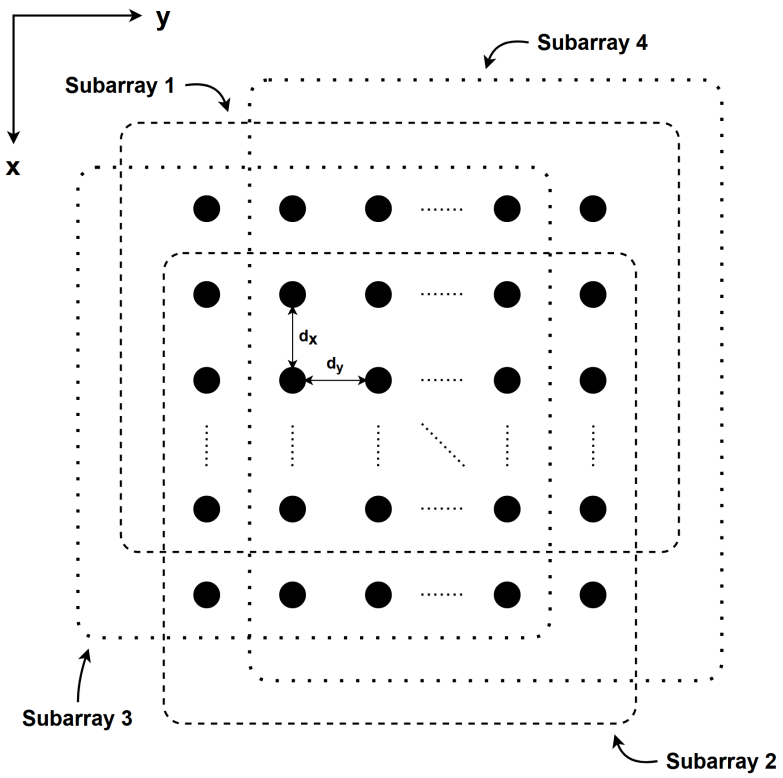

Figure 4.7: Subarrays URA

The approach for the two-dimensional problem involves decomposing it into two independent one-dimensional problems. This can be achieved by partitioning the rectangular array into two pairs of subarrays. Once again, the subarrays are selected such that they exhibit maximum overlap, as illustrated in Figure 4.7. With respect to the x-direction, the selection matrices become

$$\boldsymbol{J}_{1_{M_x}} = \begin{bmatrix} \boldsymbol{I}_{M_x-1} & \mathbf{0} \end{bmatrix}$$

and

$$\boldsymbol{J}_{2_{M_x}} = \begin{bmatrix} \mathbf{0} & \boldsymbol{I}_{M_x-1} \end{bmatrix}$$

In a comparable manner, the selection matrices in the y-direction can be described as

$$\boldsymbol{J}_{1_{M_y}} = \begin{bmatrix} \boldsymbol{I}_{M_y-1} & \mathbf{0} \end{bmatrix}^T$$

and

$$\boldsymbol{J}_{2_{M_y}} = \begin{bmatrix} \mathbf{0} & \boldsymbol{I}_{M_y-1} \end{bmatrix}^T$$

Given the array steering matrix $\boldsymbol{B}(\theta_i, \phi_i)$, the invariance relation can be expressed as

$$\boldsymbol{J}_{1_{M_x}} \boldsymbol{B}(\theta_i, \phi_i)\, e^{-j\frac{2\pi d_x}{\lambda}\cos(\theta_i)\sin(\phi_i)} = \boldsymbol{J}_{2_{M_x}} \boldsymbol{B}(\theta_i, \phi_i)$$
$$\boldsymbol{B}(\theta_i, \phi_i)\, \boldsymbol{J}_{1_{M_y}} e^{-j\frac{2\pi d_y}{\lambda}\sin(\theta_i)\sin(\phi_i)} = \boldsymbol{B}(\theta_i, \phi_i)\, \boldsymbol{J}_{2_{M_y}}$$

The data model employed for a rectangular array is defined as the column-wise stacking of the received data. To achieve this, the $vec\{\cdot\}$ operator was utilized. The same result can be achieved for the selection matrices using the Kronecker product. Specifically, the selection matrices can be represented as

$$\boldsymbol{J}_{x1} = \boldsymbol{I}_{M_y} \otimes \boldsymbol{J}_{1_{M_x}} \text{ and } \boldsymbol{J}_{x2} = \boldsymbol{I}_{M_y} \otimes \boldsymbol{J}_{2_{M_x}}$$
$$\boldsymbol{J}_{y1} = \boldsymbol{J}^T_{1_{M_y}} \otimes \boldsymbol{I}_{M_x} \text{ and } \boldsymbol{J}_{y2} = \boldsymbol{J}^T_{1_{M_y}} \otimes \boldsymbol{I}_{M_x}$$

The predefined array steering matrix, denoted as $\boldsymbol{A}(\vec{\theta}, \vec{\phi})$, satisfies the following two invariance equations

$$\boldsymbol{J}_{x1}\boldsymbol{A}\boldsymbol{\Phi}_{\boldsymbol{x}} = \boldsymbol{J}_{x2}\boldsymbol{A}$$
$$\boldsymbol{J}_{y1}\boldsymbol{A}\boldsymbol{\Phi}_{\boldsymbol{y}} = \boldsymbol{J}_{y2}\boldsymbol{A}$$

where $\boldsymbol{\Phi}_x$ and $\boldsymbol{\Phi}_y$ are the rotational operators in specified direction with the values $\begin{bmatrix} e^{-j\frac{2\pi d_x}{\lambda}\cos(\theta_1)\sin(\phi_1)} & \dots & e^{-j\frac{2\pi d_x}{\lambda}\cos(\theta_p)\sin(\phi_p)} \end{bmatrix}$ and $\begin{bmatrix} e^{-j\frac{2\pi d_y}{\lambda}\sin(\theta_1)\sin(\phi_1)} & \dots & e^{-j\frac{2\pi d_y}{\lambda}\sin(\theta_p)\sin(\phi_p)} \end{bmatrix}$ on its main diagonal, respectively. The signal subspace rotating operators, denoted by $\boldsymbol{\Psi}_x$ and $\boldsymbol{\Psi}_y$, can be determined by performing eigendecomposition. This is achievable due to the mathematical relationship

$$\boldsymbol{\Psi}_x = \boldsymbol{T}\boldsymbol{\Psi}_x\boldsymbol{T}^{-1} \text{ and } \boldsymbol{\Psi}_y = \boldsymbol{T}\boldsymbol{\Psi}_y\boldsymbol{T}^{-1}$$

As a result, the eigenvalues of $\boldsymbol{\Psi}_x$ represents estimates of the phase factors $e^{-j\frac{2\pi d_x}{\lambda}\cos(\theta_i)\sin(\phi_i)}$. Similarly, the eigenvalues of $\boldsymbol{\Psi}_y$ represents estimates of the phase factor $e^{-j\frac{2\pi d_y}{\lambda}\sin(\theta_i)\sin(\phi_i)}$. Upon obtaining these estimates, the corresponding azimuth θ_i and elevation ϕ_i can be derived as

$$\alpha_i = -\frac{\lambda}{2\pi d_x}\arg\left(e^{-j\frac{2\pi d_x}{\lambda}\cos(\theta_i)\sin(\phi_i)}\right) \text{ and } \beta_i = -\frac{\lambda}{2\pi d_y}\arg\left(e^{-j\frac{2\pi d_y}{\lambda}\sin(\theta_i)\sin(\phi_i)}\right)$$

Such that

$$\theta_i = \arg(\alpha_i + j\beta_i) \text{ and } \psi_i = \arcsin(|\alpha_i + j\beta_i|) \quad \text{for } 1 \leq i \leq p$$

4.5.1 Computational Complexity ESPRIT

The ESPRIT algorithm for a ULA can be summarized in four distinctive steps. The initial step involves calculating the spatial covariance matrix $\boldsymbol{R}$ of the sampled data.

It is important to note that the ESPRIT algorithm employs a different data model, such that calculating the covariance matrix becomes $\boldsymbol{X}^T\overline{\boldsymbol{X}}$ for the predefined data model. Given a data model $\boldsymbol{X} \in \mathbb{C}^{N\times M}$, the required number of operations is $2M^2N$.

The subsequent step involves performing eigendecomposition of the spatial covariance matrix. This decomposes the matrix into its signal subspace and noise subspace. Depending on the number of impinging signals p, the eigenvectors corresponding to the signal subspace is $\boldsymbol{V}_s \in \mathbb{C}^{M\times p}$. Using the QR algorithm, this will result in $9M^3$ operations.

The third step involves solving the invariance equation for $\boldsymbol{\Psi}$ given the signal subspace $\boldsymbol{V}_s$ and the selection matrices $\boldsymbol{J}_1 \in \mathbb{C}^{m\times M}$ and $\boldsymbol{J}_2 \in \mathbb{C}^{m\times M}$. The invariance equation can be expressed as

$$\boldsymbol{J}_1\boldsymbol{V}_s\boldsymbol{\Psi} \approx \boldsymbol{J}_2\boldsymbol{V}_s$$

The signal subspace rotating operator can be calculated using the least-squares technique such that

$$\boldsymbol{\Psi} \approx \left(\left(\boldsymbol{J}_1\boldsymbol{V}_s\right)^T\boldsymbol{J}_1\boldsymbol{V}_s\right)^{-1}\left(\boldsymbol{J}_1\boldsymbol{V}_s\right)^T\boldsymbol{J}_2\boldsymbol{V}_s$$

This requires five matrix multiplications and one matrix inversion. The first two multiplications are the selection matrices times the signal subspace. Note that the complexity of this multiplication is dependent on the number antennas in the subarrays. This requires a total of $4mMp - 2mp$ operations. The next multiplications are $\left(\boldsymbol{J}_1\boldsymbol{V}_s\right)^T\boldsymbol{J}_1\boldsymbol{V}_s$ and $\left(\boldsymbol{J}_1\boldsymbol{V}_s\right)^T\boldsymbol{J}_2\boldsymbol{V}_s$. Assuming that the translation is performed during the multiplication, a total of $4mp^2 - 2p^2$ operations are required. Next, the matrix $\left(\boldsymbol{J}_1\boldsymbol{V}_s\right)^T\boldsymbol{J}_1\boldsymbol{V}_s$ is inverted which requires $2p^3$ operations. Lastly, the last matrix multiplication is performed resulting in $2p^3 - p^2$ operations. The number operations required using the least-squares technique is $4mMp + 4mp^2 + 4p^3 - 2mp - 3p^2$.

The last step is to calculate the eigenvalues of the signal subspace rotating operator using eigendecomposition. This requires $9p^3$ operations when using QR decomposition. Afterwards, the angle θ_i can be obtained for all impinging signals p. This requires $4p$ operations, considering $-\lambda/2\pi d$ as a constant. The steps and their respective computational complexity are summarized in Table 4.7.

Table 4.7: Computational complexity ESPRIT for a ULA

Algorithm 4: ESPRIT ULA Procedure	
1. Compute the spatial covariance matrix	$2M^2N$
2. Eigendecomposition of the spatial covariance matrix	$9M^3$
3. Solving the invariance equations using the least-squares technique	$4mMp + 4mp^2 + 4p^3 - 2mp - 3p^2$
4. Eigendecomposition of the signal subspace rotating operator and computing the angles	$9p^3 + 4p$
	Total complexity: $9M^3 + 2M^2N + 4mMp + 4mp^2 + 13p^3 - 2mp - 6p^2 + 4p$

The ESPRIT algorithm for a URA, similar to that of a ULA, can be summarized in four distinctive steps. The initial step entails the calculation the spatial covariance matrix, requiring $2M^2N$ operations. In the second step, the spatial covariance matrix is decomposed into its signal subspace and noise subspace. The signal subspace is denoted by $\boldsymbol{V}_s \in \mathbb{C}^{M\times p}$, where $M = M_x \cdot M_y$ is the number of antennas comprising the array and p represents the number of impinging signals. This step requires $9M^3$ operations when using the QR algorithm.

The third step is solving the invariance equations for the signal subspace rotating operators $\boldsymbol{\Psi}_x$ and $\boldsymbol{\Psi}_y$. This is accomplished by using the signal subspace $\boldsymbol{V}_s$ and the four selection matrices: $\boldsymbol{J}_{x1}$, $\boldsymbol{J}_{x2}$, $\boldsymbol{J}_{y1}$, and $\boldsymbol{J}_{y2}$. These selection matrices have the dimensions $m_xM_y \times M$ and $m_yM_x \times M$ in the x- and y-direction, respectively. The invariance equations can be expressed as

$$\boldsymbol{J}_{x1}\boldsymbol{V}_s\boldsymbol{\Psi}_x \approx \boldsymbol{J}_{x2}\boldsymbol{V}_s$$
$$\boldsymbol{J}_{y1}\boldsymbol{V}_s\boldsymbol{\Psi}_y \approx \boldsymbol{J}_{y2}\boldsymbol{V}_s$$

In order to solve these equations, the least-square technique may be employed.

This yields the subsequent solutions:

$$\boldsymbol{\Psi}_x \approx \left(\left(\boldsymbol{J}_{x1}\boldsymbol{V}_s\right)^T \boldsymbol{J}_{x1}\boldsymbol{V}_s\right)^{-1} \left(\boldsymbol{J}_{x1}\boldsymbol{V}_s\right)^T \boldsymbol{J}_{x2}\boldsymbol{V}_s$$
$$\boldsymbol{\Psi}_y \approx \left(\left(\boldsymbol{J}_{y1}\boldsymbol{V}_s\right)^T \boldsymbol{J}_{y1}\boldsymbol{V}_s\right)^{-1} \left(\boldsymbol{J}_{y1}\boldsymbol{V}_s\right)^T \boldsymbol{J}_{y2}\boldsymbol{V}_s$$

Similar to a ULA, the computation of the signal subspace rotating operators $\boldsymbol{\Psi}_x$ and $\boldsymbol{\Psi}_y$ requires $4m_xM_yMp+4m_xM_yp^2+4p^3-2m_xM_yp-3p^2$ and $4m_yM_xMp+4m_yM_xp^2+4p^3-2m_yM_xp-3p^2$ operations respectively.

The last step is determining the azimuth and elevation. This is achieved by first performing eigendecomposition on the signal subspace rotating operators, which requires $18p^3$ operations. Afterwards, the angles can be determined. Assuming that $-\lambda/2\pi d_x$ and $-\lambda/2\pi d_y$ are constant, this requires $11p$ operations. A summary of the steps and their respective computational complexity can be found in Table 4.8.

Table 4.8: Computational complexity ESPRIT for a URA

Algorithm 4: ESPRIT URA Procedure	
1. Compute the spatial covariance matrix	$2M^2N$
2. Eigendecomposition of the spatial covariance matrix	$9M^3$
3. Solving the invariance equations using the least-squares technique	$4m_xM_yMp + 4m_yM_xMp + 4m_xM_yp^2 + 4m_yM_xp^2 + 8p^3 - 2m_xM_yp - 2m_yM_xp - 6p^2$
4. Eigendecomposition of the signal subspace rotating operator and computing the angles	$18p^3 + 4p$
	Total complexity: $9M^3 + 2M^2N + 4m_xM_yMp + 4m_yM_xMp + 4m_xM_yp^2 + 4m_yM_xp^2 + 26p^3 - 2m_xM_yp - 2m_yM_xp - 6p^2 + 11p$

4.6 Overview and Comparison

In this chapter, array signal processing techniques and their computational complexity are examined. Two methods are explored: spectral-based and parametric. The

examined spectral-based methods include the MVDR and MUSIC algorithms, while the parametric methods include the AVG and ESPRIT algorithms. A comprehensive overview of the computational complexity of these DoA estimation algorithms for both a ULA and URA is provided in Table 4.9.

Table 4.9: Overview computational complexity DoA estimation algorithms

DoA Estimation Algorithm	Complexity ULA	Complexity URA
AVG	$3NM - N + 5$	$5NM - N\left(M_x + M_y - 2\right) + 11$
MVDR	$2M^2N + M^2\left(\frac{360}{\delta} + 2N\right) + \frac{360}{\delta}M$	$2M^2N + M^2\left(\frac{64800}{\delta} + 2N\right) + \frac{64800}{\delta}M$
MUSIC	$9M^3 + M^2\left(\frac{360}{\delta} + 2N + p\right) + \frac{360}{\delta}M$	$9M^3 + M^2\left(\frac{64800}{\delta} + 2N + p\right) + \frac{64800}{\delta}M$
ESPRIT	$9M^3 + 2M^2N + 4mMp + 4mp^2 + 13p^3 - 2mp - 6p^2 + 4p$	$9M^3 + 2M^2N + 4m_xM_yMp + 4m_yM_xMp + 4m_xM_yp^2 + 4m_yM_xp^2 + 26p^3 - 2m_xM_yp - 2m_yM_xp - 6p^2 + 11p$

To compare the computational complexity of these methods, a common ground for both ULA and URA is established. It is assumed that both ULA and URA have an equal number of antenna elements (M), snapshot count (N), number of impinging signal (p), and stepsize (δ). Additionally, for a URA, an equal number of antenna elements in each direction is assumed.

With these parameters set, the dominant terms for spectral-based methods, MVDR and MUSIC, are primarily determined by the spectrum that needs to be evaluated. This is typically significantly larger than the number of antenna elements and snapshot count. For a URA compared to a ULA, the increase of the spectrum that needs to be examined is 180 times, which is reflected in the computational complexity.

In contrast, parametric methods do not require the evaluation of an entire spectrum. Their complexity is primarily determined by the snapshot count and number of antenna elements. For the AVG algorithm, the increase in computational complexity

is less than a factor of two between a ULA and URA. For the ESPRIT algorithm, this increase is even smaller, as the dominant terms $9M^3 + 2M^2N$ remain constant.

Chapter 5

Simulation

This chapter delves into the exploration and verification of DoA estimation algorithms through comprehensive simulations. The primary objective is to assess their accuracy and performance under a variety of conditions. Key parameters such as the number of snapshots, number of antenna elements, and the SNR are examined. Additionally, simulations are conducted to assess the effectiveness of frequency compensation algorithms in the presence of frequency offset and frequency drift.

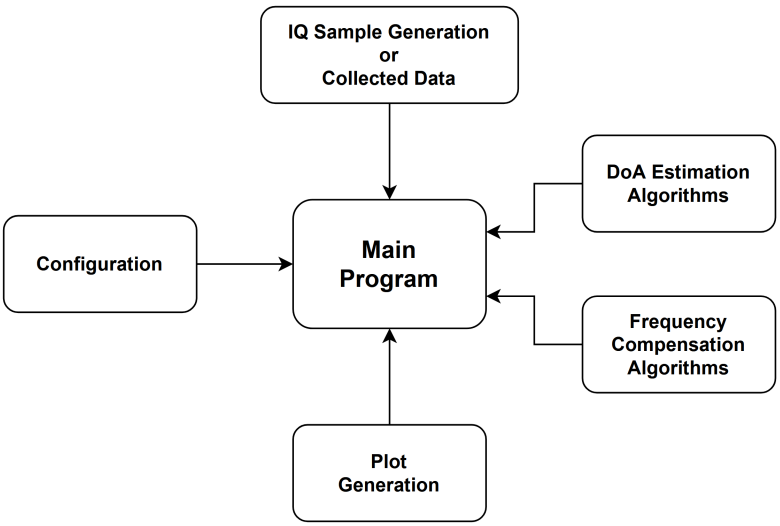

Figure 5.1: Simplified overview of the software components

Figure 5.1 offers a simplified overview of the software blocks utilized in the simulations. These blocks, coded in Python [26], form the fundamental components of the simulation process. A modular design approach has been adopted to enhance flexibility and increase reusability. The software blocks will be discussed in more depth in the subsequent sections.

5.1 IQ Sample Generation

The simulating of various DoA estimation algorithms necessitates the generation of IQ samples. A streamlined approach is adopted, focusing on the generation of these IQ samples without the need of simulating both the receiver and transmitter. Ideal IQ samples are generated and manipulated to achieve the desired results. The generation of these IQ samples is not arbitrary but strictly adheres to the Bluetooth Core Specification.

Three primary parameters outlined in the Bluetooth Core Specification influence the generation of ideal IQ samples:

1. Length of the CTE: This parameter, an integer ranging from 2 to 20, corresponds to a CTE duration from 16 to 160 µs. It can be defined as $8 \cdot k$ µs , for $k \in [2, \ldots, 20]$. The length of the CTE determines the maximum number of sample slots within a Bluetooth packet.
2. Slot duration: This parameter specifies the time of the switch and sample slots, which subsequently determines, in combination with the CTE length, the number sample slots within the CTE. The slot duration can be either 1 or 2 µs.
3. PHY mode: The PHY mode, in combination with the slot duration, determines the fixed phase difference between IQ samples from consecutive sample slots. The PHY mode can be either LE 1M PHY or LE 2M PHY.

Upon generation of the ideal IQ samples, additional parameters such as initial phase, frequency offset, frequency drift, incident angle(s), and noise can be incorporated. Assuming unity amplitude, the signal describing the IQ samples which include the PHY mode, initial phase, frequency offset, and frequency drift at a certain time t in microseconds can be described as

$$s\left(t\right) = e^{\left(\theta_{init} + 2\pi\left(mode \cdot 250 \cdot 10^3 + f_{offset} + f_{drift} \cdot t\right) \cdot t\right) j}$$

Where:

- θ_{init} represents the initial phase of the signal in radians.
- $mode$ denotes the PHY mode used, which is either 1 for LE 1M PHY or 2 for LE 2M PHY.
- f_{offset} is the frequency offset in hertz.
- f_{drift} is the frequency drift in hertz per second.

The initial phase, frequency offset, and frequency drift are all selected from a uniform distribution. The initial phase is restricted to the interval $[0, 2\pi)$ radians. The intervals for the frequency offset and drift, on the other hand, are user-defined. The values for these parameters are selected from a uniform distribution that spans the respective

intervals. Subsequently, the IQ samples can be manipulated to incorporate the incident angle. For a ULA the phase difference (ϕ_Δ) between two consecutive antenna is defined as

$$\phi_\Delta = \frac{2\pi d}{\lambda} \sin(\theta)$$

In an ideal world, the phase difference between consecutive antennas is fixed, implying that the phase difference can be multiplied with the antenna index to get the correct phase difference. The same procedure can be applied to a URA. The only difference is that the phase difference between antennas is the sum of its x- and y-direction components. This is mathematically defined as

$$\phi_{\Delta_x} = \frac{2\pi d_x}{\lambda} \cos(\theta) \sin(\phi)$$

$$\phi_{\Delta_y} = \frac{2\pi d_y}{\lambda} \sin(\theta) \sin(\phi)$$

Again, in an ideal world, these direction dependent phase differences can be added based on the antenna index in each direction.

Bluetooth provides the capability to utilize 36 channels for the transmission of packets that contain a CTE. The selection of these channels in simulation is not arbitrary but is instead drawn from a uniform distribution. This method is employed to mimic the frequency hopping technique inherent to the Bluetooth technology. As the wavelength is dependent on the channel, this will alter the phase difference between antennas in an antenna array.

Finally, AWGN can be incorporated into the IQ samples. This is to simulate real-world conditions where signals are often subject to noise. The level of noise added is contingent upon the desired SNR.

In Figure 5.2 the unwrapped arguments of the IQ samples for a 4x4 antenna array are depicted. The parameters used to generate these IQ samples are as follows: a slot duration of 2 µs, a PHY mode of LE 1M PHY, and a CTE length of 9, which corresponds to a duration of 72 µs. A total of 1000 snapshots are generated utilizing all 36 Bluetooth channels with a SNR of 15 dB. The incident angle was set at 90° azimuth and 45° elevation. No frequency offset and drift were applied in the generation of the IQ samples.

5.2 Simulation of Direction of Arrival Estimation Algorithms

The generated IQ samples, as described in the preceding section, serve as the input for the DoA estimation algorithms. This thesis includes four DoA estimation algorithms: AVG, MVDR, MUSIC, and ESPRIT. Each algorithm operates on similar

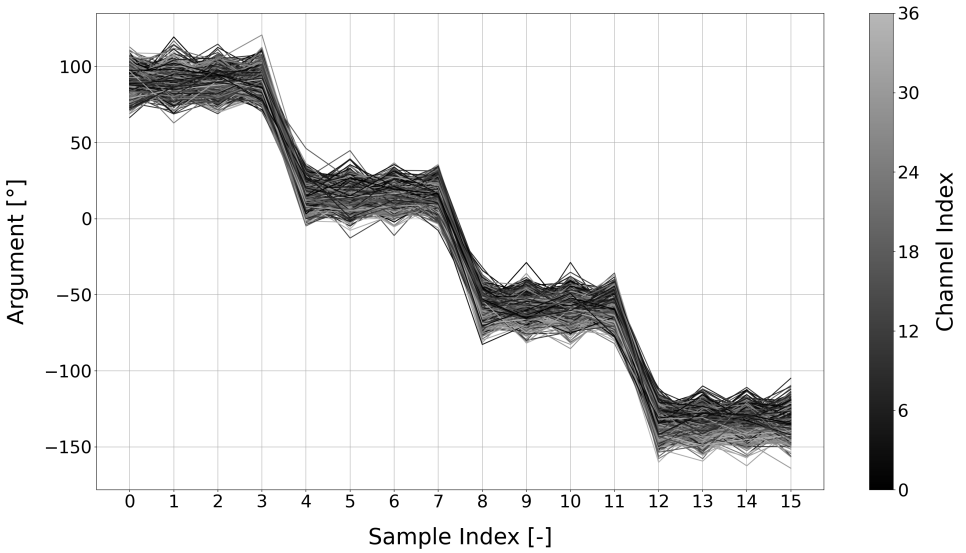

Figure 5.2: Unwrapped arguments versus sample index

parameters, which include IQ samples, wavelength and inter-element spacing. An additional parameter, the number of incident angles, is required for the algorithms MUSIC and ESPRIT. The output of these algorithms is the estimated incident angles.

The simulations are conducted under a set of assumptions and considerations. Firstly, the presence of only one impinging signal is assumed. This assumption is justified by the fact that a Bluetooth device can only synchronize with a single other Bluetooth device in both connection-oriented and connectionless mode. Secondly, only a LoS is assumed to limit the scope.

During the simulations, a slot duration of 2 µs and the PHY mode LE 1M PHY are used. These values are specifically selected as Bluetooth devices supporting the direction finding feature shall at least support this PHY mode and slot duration. Furthermore, DoA estimation algorithms only consider a single wavelength to estimate the incident angle. A wavelength of 0.122795 meters is selected, as it corresponds to the center frequency of the usable Bluetooth channels. Finally, the inter-element spacing is fixed at 0.0360 meter, matching with the inter-element spacing of the antenna array used during the field measurements.

The primary objective of these simulations is to examine the results for the key parameters: SNR, number of snapshots, and number of antenna elements. To compute the Root-Mean-Square Error (RMSE), a total of 1000 runs are executed for each result.

5.2.1 Signal-to-Noise Ratio

The SNR is a crucial factor in the successful reception of Bluetooth packets and consequently in the ability to estimating the incident angles. Unfortunately, the Bluetooth Core Specification does not explicitly define a minimum SNR. Instead, it specifies a minimum sensitivity level for which at least a Bit Error Rate (BER) of 0.1% must be achieved. This sensitivity level shall not exceed -70 dBm when using the LE Uncoded PHYs [6]. In practice, typical Bluetooth implementations achieve a receiver sensitivity level of -95 dBm or better [27]. The receiver sensitivity level can be used to approximate the minimum SNR required to achieve the defined BER. The minimum SNR can be calculated using the following formula [28]:

$$SNR_{min} = S_{min} - k_B T_0 B - NF$$

The terms $k_B T_0 B$ is also referred to as mean power of the standard noise that is available at the input of the receiver, where k_B is the Boltzmann constant, T_0 is the mean noise temperature in Kelvin, and B is the receiver bandwidth in hertz. Assuming a standard noise temperature of 290 K and a bandwidth of 1 MHz, which corresponds to the LE 1M PHY, the $k_B T_0 B$ approximates -114 dBm. The noise factor (NF) depends on the architecture of the Bluetooth device. A noise factor around 8 dB is assumed, as BLE devices in literature deviate around this value [29]. For a minimum sensitivity levels (S_{min}) of -70 dBm and -95 dBm, the minimum SNR becomes approximately 5.83 dB and -19.17 dB, respectively.

Simulations were conducted over a SNR range from -25 to 25 dB. The snapshot count was maintained at 25 throughout the simulations. The antenna array was configured in a 4x4 grid, resulting in a total of 16 antennas. The results of these simulations are depicted in Figure 5.3.

The performance of the AVG algorithm is noticeably inferior compared to the other three algorithms when the number of snapshots and antennas are held constant. The AVG algorithm's performance begins to deteriorate rapidly once the SNR falls below 10 dB. On the other hand, the other three algorithms exhibit almost identical behavior. Their performance primarily starts to decline when the SNR drops below 0 dB. This indicates that the AVG algorithm is not as robust, which limits its applicability in real-world scenarios where low SNR conditions are expected.

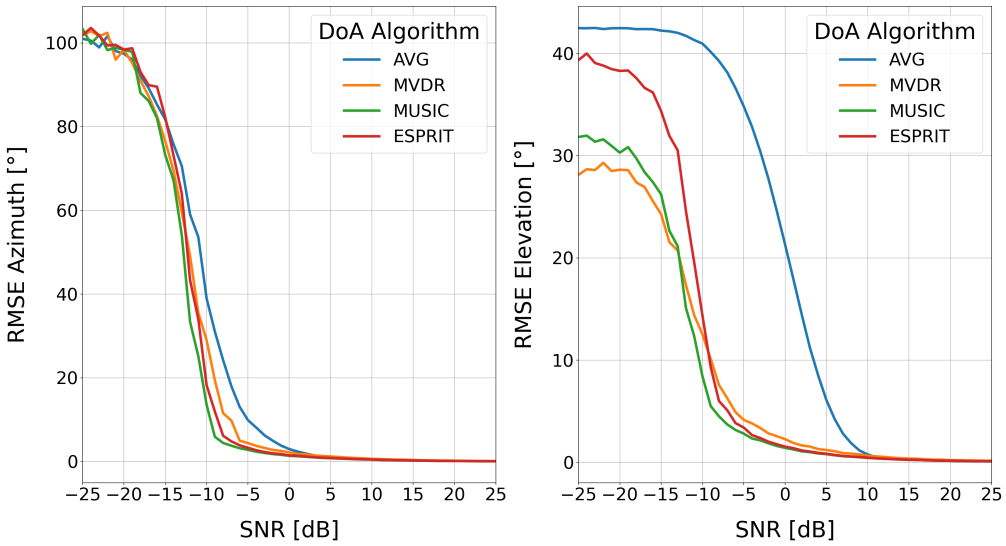

Figure 5.3: RMSE for azimuth and elevation as a function of the SNR

5.2.2 Number of Snapshots

The number of snapshots is a critical factor in accurately determining the incident angle. Increasing the number of snapshots can enhances the precision by facilitating a more accurate determination of the noise. However, this increase in snapshots inversely affects the update rate of the estimated incident angles, thereby presenting a trade-off.

Simulations were conducted to evaluate the performance of the DoA estimation algorithm in relation to the number of snapshots. The number of snapshots was varied incrementally from 1 to 100. Utilizing a 4x4 antenna array and a SNR of 5 dB, the results depicted in Figure 5.4 were obtained.

A careful analysis of the results reveal that all DoA estimation algorithms converge towards a fixed RMSE limit as the number of snapshots increases. This is particularly noticeable for the AVG algorithm, where beyond a certain threshold, an increase in the number of snapshots does not further decrease the RMSE, given that the SNR and antenna count remain constant. This limit is nearly reached for both azimuth and elevation when the number of snapshots is approximately 25 or more. Furthermore, the disparity between the RMSE for azimuth and elevation for the AVG algorithm aligns with the observation from the SNR simulations.

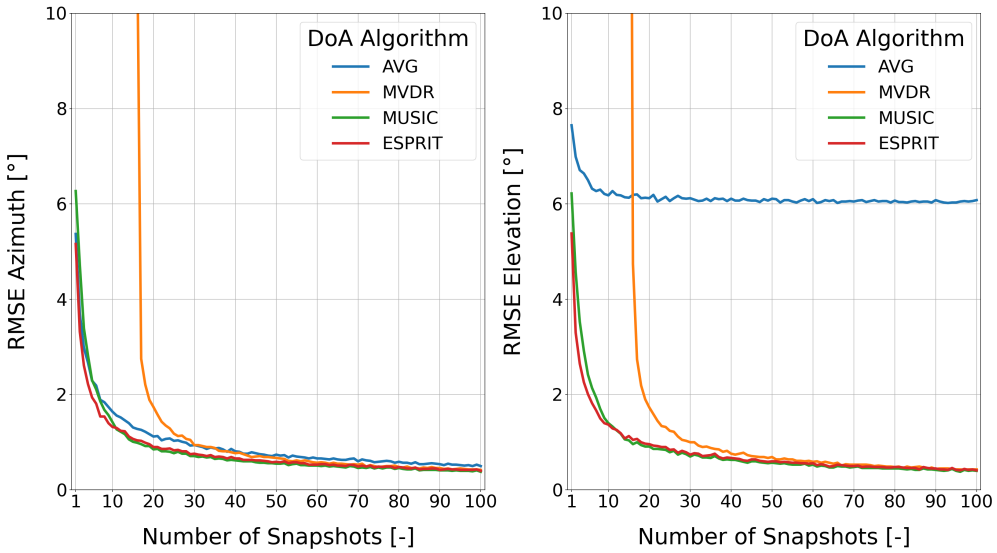

Figure 5.4: RMSE for azimuth and elevation as a function of the snapshot count

5.2.3 Number of Antennas

The final parameter under consideration is the number of antennas. The maximum number of antennas is primarily constrained by the number of available sample slots. With a slot duration of 2 µs, there are up to 38 sample slots available. This allows for a maximum antenna array consisting of 6x6 elements, assuming only antenna arrays are considered with equal number of antennas in both directions.

Simulations were conducted to evaluate the performance of the DoA estimation algorithm in relation to the number of antennas. The number of antennas was varied such that there were equal antennas in both directions, ranging from 2 to 6 antennas. With a constant snapshot count of 25 and a SNR of 5 dB, the results depicted in Figure 5.5 were obtained.

The results indicate that as the number of antennas increases, the RMSE gradually approach a fixed limit, with the exception of the MVDR algorithm. This pattern is similar to the simulation where the number of snapshots is altered. The limit is influenced by the SNR and the number of snapshots. During these simulations, it is assumed that the antennas are ideal, which implies that no imperfections of the antennas are taken into consideration. Consequently, resulting only in an augmentation of samples for each snapshot.

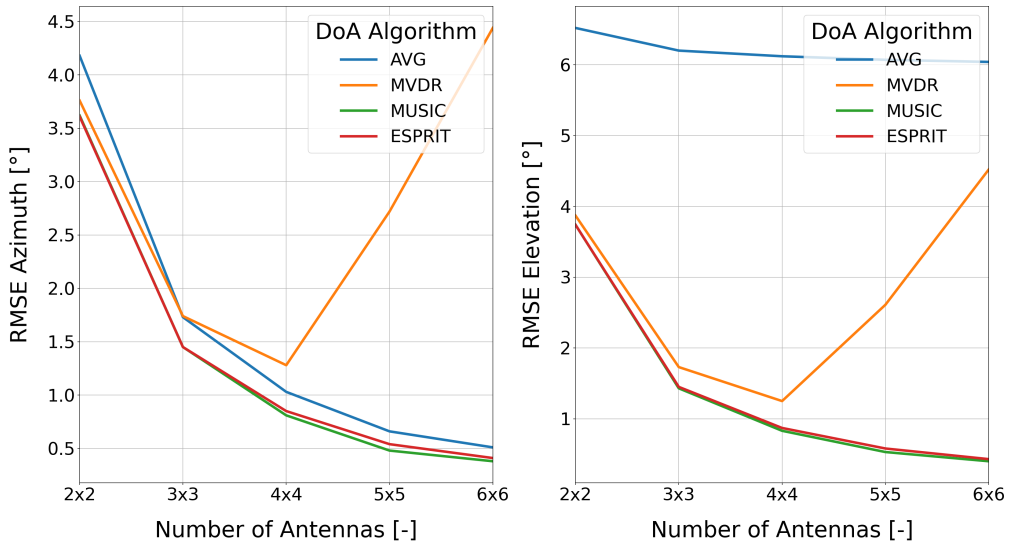

Figure 5.5: RMSE for azimuth and elevation as a function of the number of antennas

5.3 Evaluation of Frequency Compensation through Simulation

A series of simulations have been conducted to evaluate the effectiveness of frequency compensation algorithms in the presence of frequency offset and drift. Initially, the algorithms are evaluated in presence of only frequency offset. As per the Bluetooth Core Specification, the deviation in the center frequency during a Bluetooth packet is not permitted to exceed ±150 kHz. Figure 5.6 offers a visual representation of the unwrapped arguments of the generated IQ samples for a single antenna element when a frequency offset is applied. The applied frequency offset has a uniform distribution, with offsets ranging from 48 kHz to 52 kHz. In addition, a total of 1000 Bluetooth packets are depicted, each with a SNR of 30 dB.

During the reference period, eight IQ samples are collected from the reference antenna at an interval of 1 µs. These reference samples serve as a basis for estimating the frequency offset. Three frequency offset compensation algorithms - Median, Average, and Linear Least Squares (LLS) - are evaluated using these reference samples. Additionally, the LLS algorithm is also assessed using the initial four data samples, corresponding to the sample indices 0, 1, 2, and 3. The resulting RMSE for these algorithms, when applied to either the reference or data samples, is depicted in Figure 5.7.

The LLS algorithm outperforms both the Median and Average algorithms when only reference samples are used. The improvement over the Average algorithm

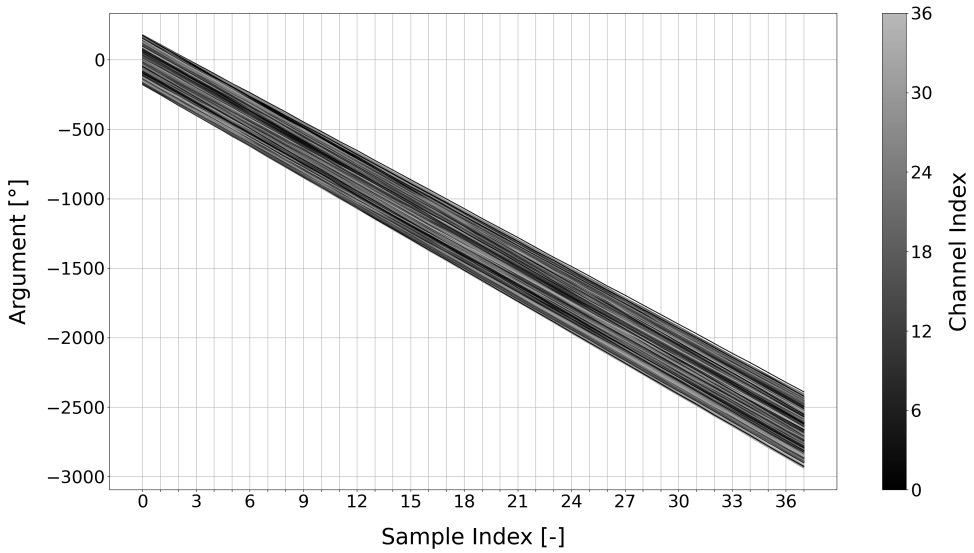

Figure 5.6: Unwrapped arguments with frequency offset

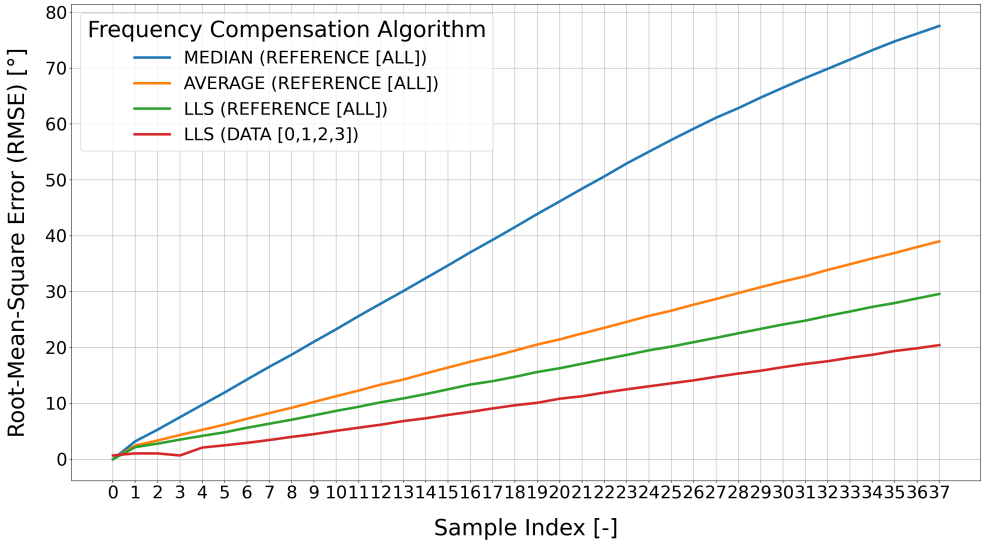

Figure 5.7: Performance of the Average, Median, and LLS frequency compensation algorithms across sample indices

is relatively small, around 10° in the best-case scenario, while the improvement compared to the Median algorithm is almost 50°. Interestingly, substituting data samples for reference samples in the LLS algorithm further improve the results. However, even in this scenario, the worst-case RMSE is still approximately 20°. Despite these improvements, the RMSE continues to rise for all algorithms as the sample index increases. This suggests that using sample indices at the start of

the CTE is insufficient for accurately determining the frequency offset in a noisy environment.

In an attempt to further improve on these results, the sample indices at the end of the CTE are also taken into consideration. Given its superior performance, only the LLS algorithm is employed for this simulation. Three distinct sets of samples are used. In the first set, only data samples corresponding to the sample indices 0, 1, 36, and 37 are used. The second set is similar but also includes all reference samples. It should be noted that the last reference sample (reference sample index 7) is identical to the first data sample (data sample index 0), hence, to prevent duplication of IQ samples, the first data sample is excluded. The third set is akin to the second set, but only the reference samples corresponding to the sample indices 0 and 7 are considered.

Figure 5.8a shows the performance of LLS algorithm for the three datasets. The performance of the three sets exhibits a close correlation, making it evident that the utilization of a larger number of samples yields better results. As the sample index increases, the performance of the datasets begins to converge. This convergence is due to the use of identical sample indices at the end, specifically sample index 36 and 37. This is in contrasts with the start sample indices, where the number of samples used varies per dataset. Consequently, a trade-off emerges between the number of samples used for frequency compensation and those used for estimating the incident angles. However, it is noteworthy that increasing the number of samples does not significantly enhance the performance. The maximum improvement observed between the three datasets is a mere approximately 0.2°.

The superior algorithm and dataset are applied to correct the IQ samples of the 1000 Bluetooth packets. This involves using the LLS algorithm with all reference samples and data samples corresponding to the sample indices 1, 36, and 37. The unwrapped argument resulting from this correction is depicted in Figure 5.8b. The frequency offset is effectively eliminated in this process, leaving only observable noise.

The Bluetooth specifies also specify a maximum frequency drift of 400 Hz/µs, with a maximum drift of ±50 kHz within a Bluetooth packet. To evaluate the performance of the algorithms under these conditions, frequency drift is added to each packet. This drift is uniformly distributed between 75 and 100 Hz/µs and is added in addition to the frequency offset. In this scenario, a constant frequency drift throughout the CTE is assumed.

The frequency drift is applied to the 1000 Bluetooth packets. When applying the LLS algorithm with the three predefined datasets, the RMSE as depicted Figure 5.9 was observed. The results reveal a parabolic shape after frequency compensation. This outcome aligns with expectations, as only samples at the start and end of

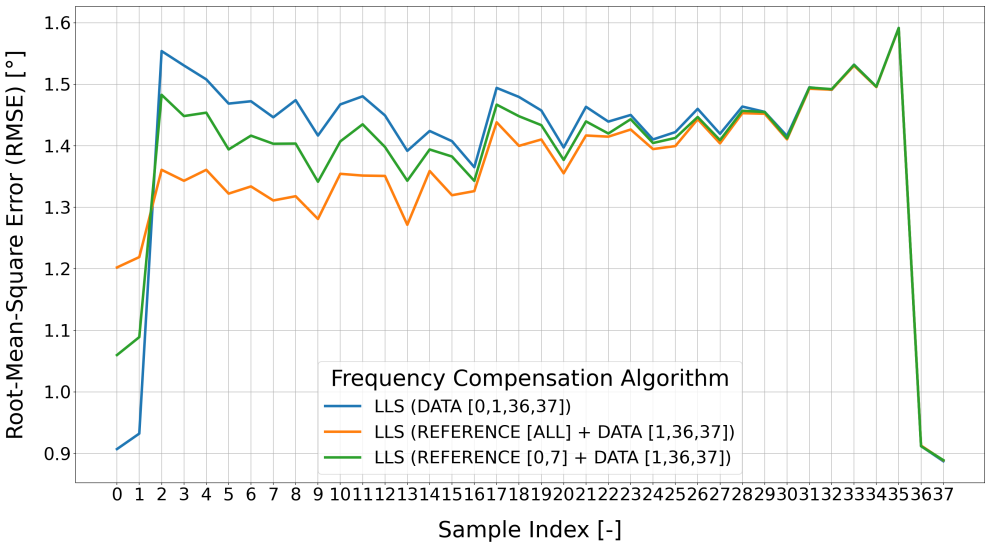

(a) Performance of the LLS algorithm using the three datasets (frequency offset)

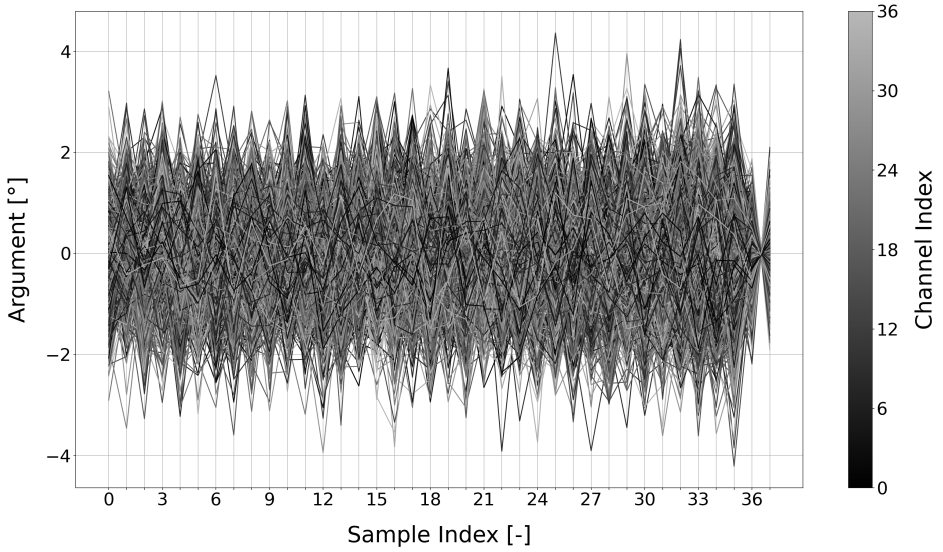

(b) Unwrapped arguments after frequency compensation with the LLS algorithm

Figure 5.8: Performance comparison and unwrapped arguments for the three datasets (frequency offset)

the CTE are used, thereby allowing only for linear interpolation. This essentially allows exclusively for the determination and correction of frequency offset. For a more precise estimation of the frequency drift, quadratic interpolation is required. This implies that samples, preferably uniformly distributed, throughout the CTE are necessary.

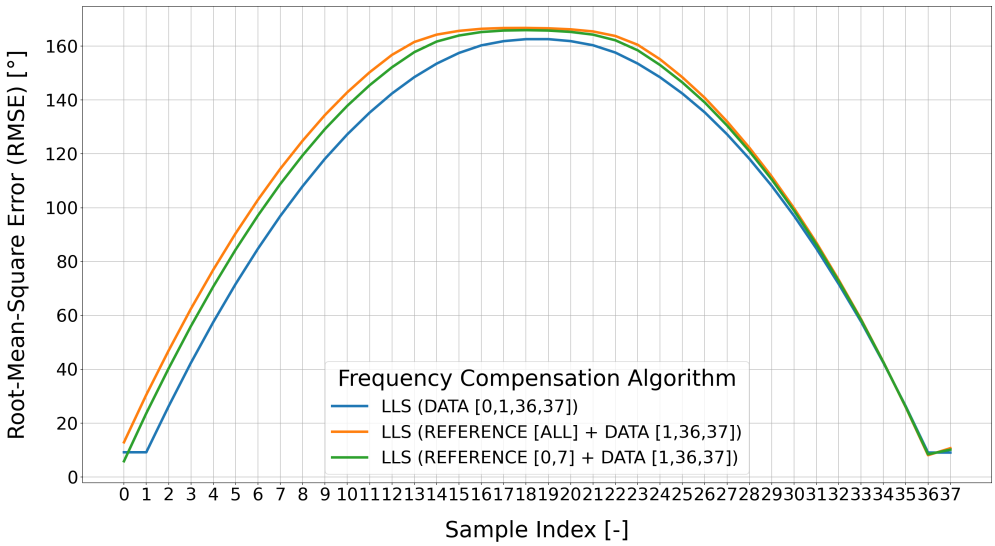

(a) Performance of the LLS algorithm using three datasets (frequency offset and drift)

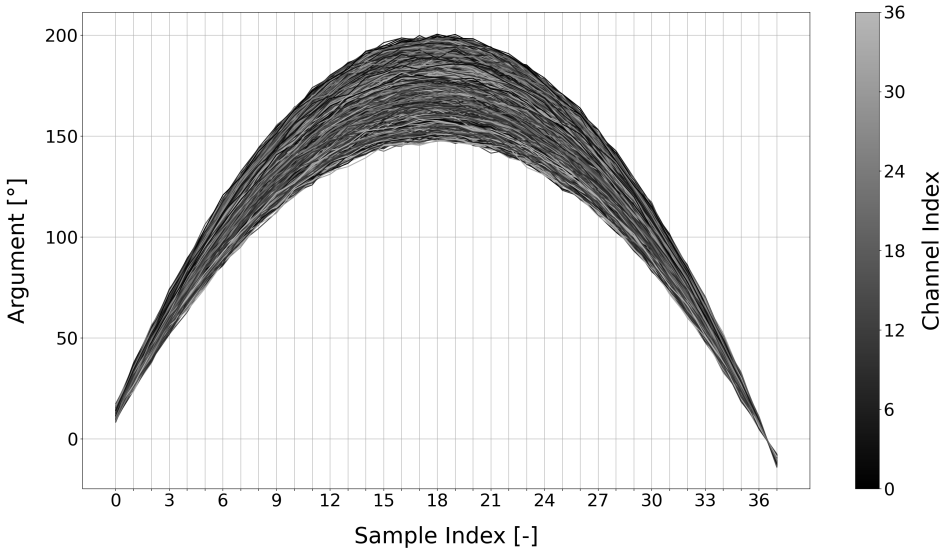

(b) Unwrapped argument after frequency compensation with the LLS algorithm

Figure 5.9: Performance comparison and unwrapped arguments for the three datasets (frequency offset and drift)

5.4 Conclusion

This chapter has presented a comprehensive evaluation of the performance of four DoA estimation algorithms, considering three key parameters: SNR, snapshot count, and number of antennas. The generation of IQ samples, in compliance with the Bluetooth Core Specification, was explained. Rather than simulating both transmit-

ter and receiver, the IQ samples were manipulated to yield the desired results.

The performance of the AVG algorithm was noted to deteriorate when the SNR dropped below 10 dB during the simulation. A similar trend was observed for the other three DoA estimation algorithms, whose performance began to decline when the SNR fell below 0 dB. The snapshot count was held constant at 25 for these simulations, and a 4x4 antenna array was used.

It was observed that the RMSE converged to a fixed limit as either the snapshot count or number of antennas increased. Beyond approximately 25 snapshots, no further improvement in RMSE was observed when using a 4x4 antenna array and a SNR of 5 dB. The number of antennas is limited by the sample slots defined by the Bluetooth Core Specification, leading to improvements across all antenna configurations. Although, these improvements diminish as the number of antennas increases.

The chapter also assess the impact of frequency offset and drift. Three frequency compensation algorithms - Average, Median, and LLS - were evaluated. The LLS algorithm proved to be superior. However, it was concluded that the reference samples alone are insufficient to accurately determine the frequency offset. Instead, samples at the start and end of the CTE are required.

A RMSE of less than 2.0° was achieved after frequency compensation using the LLS algorithm with all reference samples and data samples corresponding to the sample indices 1, 36, and 37. This result was obtained under the conditions where a SNR of 30 dB was used and a frequency offset uniformly selected in the range of 48 to 52 kHz.

The frequency compensation algorithms were found to be ineffective when frequency drift is present due to their reliance on linear interpolation. Consequently, in instances where frequency drift is present, a parabolic shape was observed upon applying these algorithms.

Chapter 6

Measurement Setups and Results

In the previous chapters, the DoA estimation algorithms and theories behind direction finding and Bluetooth itself are introduced. Furthermore, simulations are performed to provide an evaluation of the expected performance and behavior of the algorithms. In this chapter measurement setups used for field measurements are described. This includes the hardware, software, and information about the setup and data collection. Afterwards, the collected data is evaluated.

6.1 Hardware and Software for Data Collection

In the process of data collection, a variety of hardware components were utilized. In this section the hardware and software components used for data collection are discussed.

Primary Anchor: BG22-RB4191A
The primary anchor used is the BG22-RB4191A, a 4x4 dual polarized antenna array from Silicon Labs [30]. This antenna array is specifically designed for evaluation and development purposes using the direction finding feature introduced in Bluetooth 5.1.

At the core of this antenna array is the EFR32BG22 wireless System-on-Chip (SoC) from Silicon Labs [31]. Alongside the hardware components, Silicon Labs has developed a Python package known as PyBGAPI [32]. This package provides a means to interface with the SoC via a serial interface. In this setup, the SoC is responsible for running the Bluetooth stack and handling all low-level operations related to Bluetooth communication. On the other hand, the application runs on a separate host device, such as a PC. A debug adapter board is required to let the host device communicate with the SoC on the antenna array.

(a) Top view (b) Bottom view

Figure 6.1: Antenna array BG22-RB4191A

Secondary Anchor: CHW1010-ANT2-1.0

The secondary anchor utilized is the CHW1010-ANT2-1.0 antenna array from CoreHW [33]. This is a 4x4 antenna array composed of patch antennas. The selection of these antennas is facilitated by SP16T antenna switch, which is incorporated on the antenna array. An external Bluetooth transceiver, which can be connected using a U.FL connector, is required for this system.

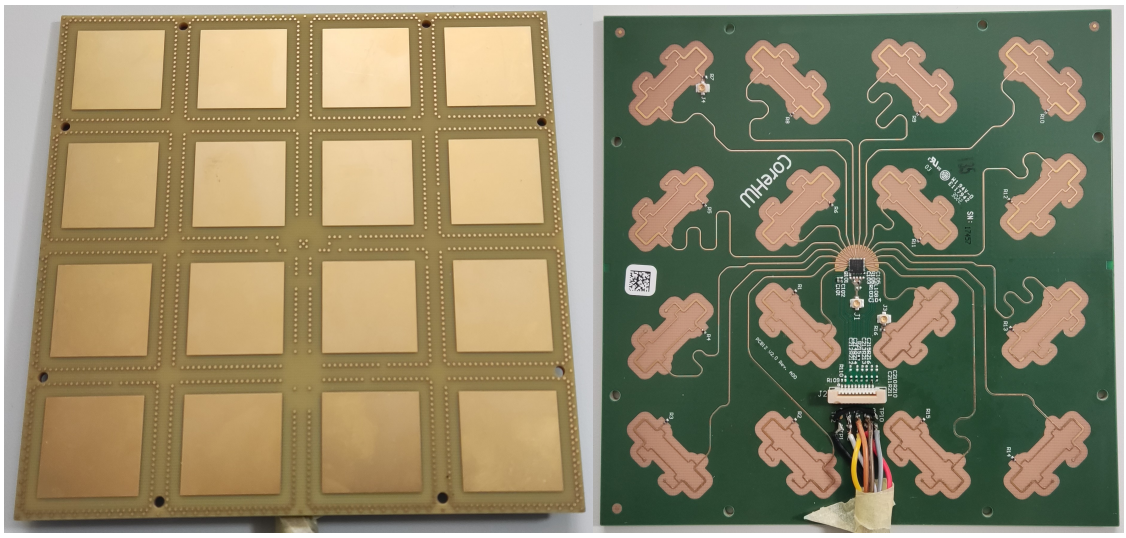

(a) Top view (b) Bottom view

Figure 6.2: Antenna array CHW1010-ANT2-1.0

Tag: SLTB010A

As tag the SLTB010A from Silicon Labs is utilized [34]. This development board is also centered around the ERF32BG22 Wireless SoC. It can be powered via either the micro USB connector or a CR2032 coin cell. The SLTB010A contains a ceramic PCB antenna, with its reference design and radiation pattern depicted below.

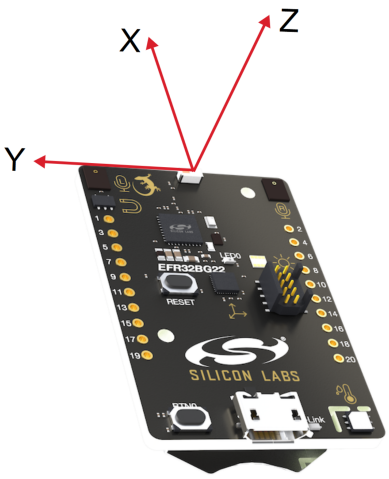

(a) SLTB010A

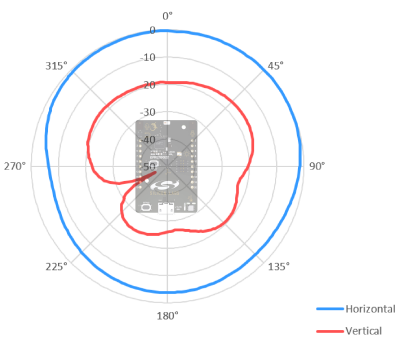

(b) Radiation pattern - XY

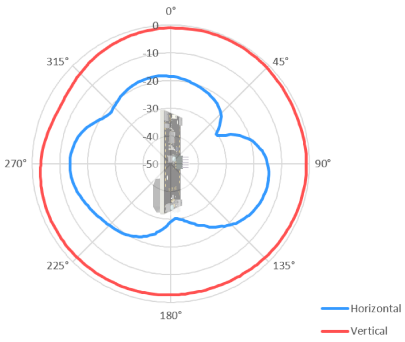

(c) Radiation pattern - XZ

Figure 6.3: SLTB010A with normalized radiation pattern [35]

6.2 Experimental Setups

In order to gather the necessary data for analysis, measurements are conducted in two distinct environments. The initial setup was the anechoic chamber at the University of Twente. The final setup, where the concluding measurements are conducted, was located in the anechoic chamber at ASTRON.

Experimental Setup at University of Twente

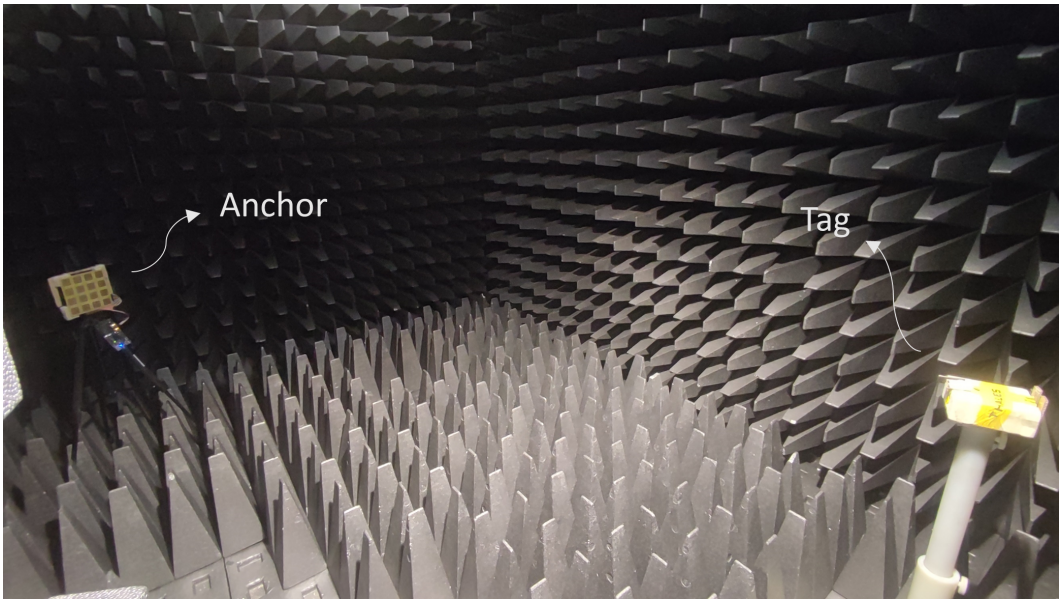

Figure 6.4: Measurement setup University of Twente

The initial experiments and measurements were conducted in the anechoic chamber at the University of Twente. As depicted in Figure 6.4, the measurement setup consists of two main components: the anchor and the tag.

The anchor, depicted on the left side of Figure 6.4, is mounted to a camera tripod. This setup allows for the rotation of the anchor to modify the angle of incident as needed. Two types of antenna arrays, namely BG22-RB4191A and CHW1010-ANT2-1.0, are utilized for the anchor. The anchor is connected to a debugger, which in turn is connected via a USB cable to a laptop outside the chamber. This connection facilitates not only the configuration of the anchor but also enables immediate processing of the captured IQ samples.

The tag, depicted on the right side of Figure 6.4, is mounted to an adjustable pedestal. The SLTB010A is used for the tag. Both the tag and anchor are positioned at equal height, ensuring that the tag aligns with the center of the antenna array. Furthermore, careful attention has been paid to align their polarizations.

Experimental Setup at ASTRON

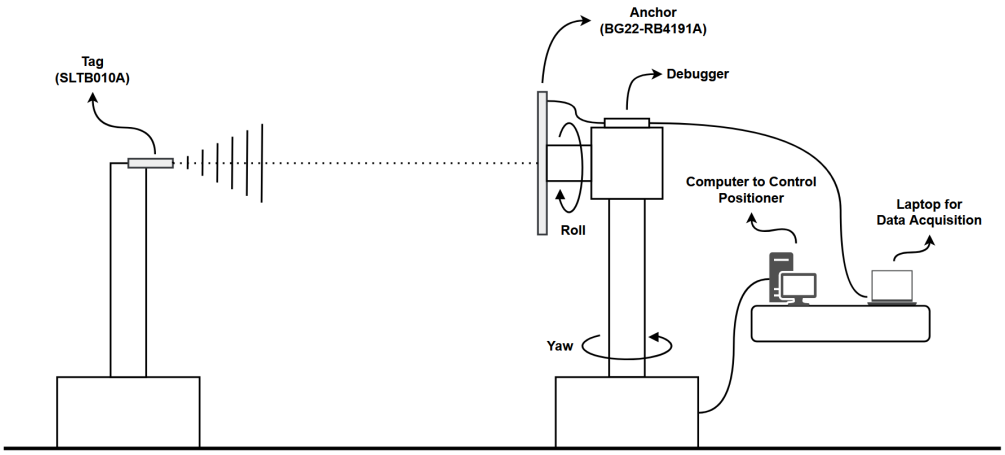

Figure 6.5: Measurement setup ASTRON

For the final measurements, the anechoic chamber at ASTRON was made available. This chamber is equipped with a positioner that allows the incident angle to be adjusted precisely. The positioner operates based on a roll-over-yaw mechanism, which allows for the adjustment of both roll and yaw angles within a range of -90° to 90°.

Considering that the DoA estimation algorithms yield the estimated azimuth (θ) and elevation (ϕ), a translation between these systems is necessary. For azimuth in the range of $0° \leq \theta \leq 180°$ and elevation in the range of $0° \leq \phi \leq 90°$, the conversion to roll and yaw angles can be accomplished using the following formulas:

$$yaw = \phi$$
$$roll = \theta - 90°$$

For azimuth in the range of $-180° \leq \theta \leq 0°$ and elevation in the range of $0° \leq \phi \leq 90°$, the conversion can be achieved using:

$$yaw = -\phi$$
$$roll = \theta + 90°$$

The antenna array is mounted onto the positioner such that its x-axis is oriented towards the tag and its z-axis towards the ceiling, as depicted in Figure 6.5 and Figure 6.6. Similarly, the tag is positioned such that its x-axis is oriented towards the center of the antenna array and the z-axis points to the ceiling. In this configuration, the horizontal port of the dual polarized antenna array aligns with the polarization of the tag. The procedure for aligning the tag and anchor can be found in Appendix A.

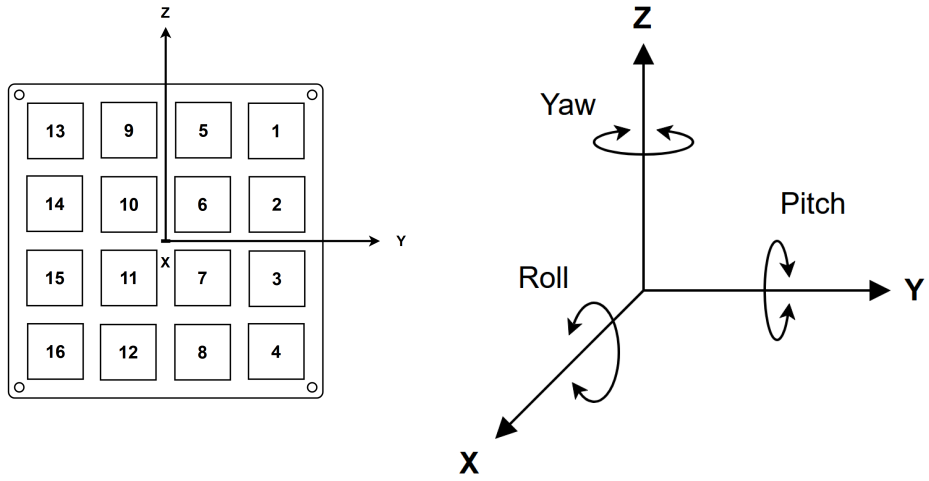

(a) Antenna array with coordinate axes (b) Roll, pitch, and yaw

Figure 6.6: Antenna array with corresponding roll, pitch, and yaw

6.3 Data Collection

During the data collection process at ASTRON, certain parameters are maintained constant throughout the measurements. These parameters include a slot duration of 2 µs and the PHY mode LE 1M PHY, both of which are mandatory for any Bluetooth device that supports the direction finding feature. A slot duration of 2 µs allows for a maximum of 38 sample slots per CTE. Additionally, all 36 Bluetooth channels are used, over which transmission of packets containing a CTE is allowed.

The data collection process primarily involves three types of measurements. The first measurement is conducted to verify the effectiveness of frequency compensation in eliminating frequency offset and drift. During this measurements, 1000 Bluetooth packets are captured using only the reference antenna ANT13. Both the horizontal and vertical ports are used, and the transmits powers of 8.5, 2.0, and -8.5 dBm are used. The subsequent measurements, namely antenna compensation measurements and data measurements, will be elaborated upon in the following sections.

6.4 Antenna Compensation Measurements

The objective of the antenna compensation measurements is to acquire data that can be used for antenna compensation. For these measurements both ports, horizontal and vertical, are used. A total of 1000 Bluetooth packets are captured on each port, covering all 36 Bluetooth channels. The measurements are conducted

for the transmit powers 8.5, 2.0, and -8.5 dBm.

The incident angles are adjusted while preserving the polarization alignment, which implies a roll of 0 degrees. This corresponds to an azimuth of either +90 or -90 degrees. The elevation is varied according to a predetermined sequence: 0, 15, 30, 45, 60, 75, and 85 degrees. To avoid redundancy, data is collected at an elevation of 0 degrees only once, resulting in a total of 13 unique incident angles.

To optimize the use of the available 38 sample slots, the following antenna switching pattern is employed:

[ANT13, ANT13, ANT13, ANT13, ANT14, ANT14, ANT15, ANT15, ANT16, ANT16, ANT9, ANT9, ANT10, ANT10, ANT11, ANT11, ANT12, ANT12, ANT5, ANT5, ANT6, ANT6, ANT7, ANT7, ANT8, ANT8, ANT1, ANT1, ANT2, ANT2, ANT3, ANT3, ANT4, ANT4, ANT13, ANT13, ANT13, ANT13]

The collected data is stored in a pickle file using the specific naming convention:

comp_data_[date]_pkts_[packets]_pol_[polarization]_az_[azimuth]_el_[elevation]_pwr_[power]_whole_antenna.pkl

The variables within the square brackets are set according to the specified value. Where:

- Date: The date when the data was obtained in the format YYYY_MM_DD.
- Packets: The number of Bluetooth packets obtained.
- Polarization: Can be either “HORIZ” or “VERT” for horizontal and vertical port, respectively.
- Azimuth: The azimuth angle in degrees.
- Elevation: The elevation angle in degrees.
- Power: The transmit power of the tag. Must be divided by ten to obtain the original transmit power in dBm.

The pickle module [36] is used for serialization and deserialization of Python objects. Each pickle file contains four Python objects:

1. Data: The IQ samples obtained during the sample slots.
2. Reference: The IQ samples obtained during the reference period.
3. Channel: Channel index at which each Bluetooth packet is obtained.
4. RSSI: The Received Signal Strength Indicator (RSSI) for each Bluetooth packet.

6.5 Data Measurements

The final set of measurements, referred to as data measurements, share similarities to the antenna compensation measurements. Both ports and identical transmit

powers are utilized. However, a distinction lies in the number of captured Bluetooth packets. For these measurements, only 500 packets are captured, as opposed to 1000, across the 36 Bluetooth channels.

During the data measurements, adjustments are made to both azimuth and elevation. This change in azimuth results in a misalignment of the antennas' polarization. The elevation is varied according to a predetermined sequence: 0, 15, 30, 45, 60, 75, and 85 degrees. Conversely, the azimuth angles are adjusted according to the sequency: -75, -60, -45, -30, -15, -5, 5, 15, 30, 45, 60, and 75 degrees. This results in a total of 84 unique incident angles.

A slightly different antenna switching pattern is also employed:

[ANT13, ANT13, ANT13, ANT14, ANT15, ANT16, ANT9, ANT10, ANT11, ANT12, ANT5, ANT6, ANT7, ANT8, ANT1, ANT2, ANT3, ANT4, ANT13, ANT14, ANT15, ANT16, ANT9, ANT10, ANT11, ANT12, ANT5, ANT6, ANT7, ANT8, ANT1, ANT2, ANT3, ANT4, ANT13, ANT13, ANT13, ANT13]

The collected data is stored in a pickle file. The naming convention is similar to the antenna compensation measurements with the exception that the prefix "comp_" is omitted.

6.6 Frequency Compensation

The effectiveness of frequency compensation on captured IQ samples is evaluated utilizing the same antenna throughout the entire duration of the CTE. These measurements are conducted at ASTRON, where a total of 1000 Bluetooth packets are captured at each transmit power level, exclusively using the reference antenna ANT13.

In Figure 6.7, the unwrapped arguments of the unprocessed IQ samples, transmitted at a power level of 8.5 dBm, are plotted against their corresponding sample indices. A prominent frequency offset is observed, characterized by the linear behavior exhibited by the unwrapped arguments. This frequency offset remains consistent across all channel indices, indicating its independence from the center frequency used.

Upon applying the superior frequency compensation algorithm, namely the LLS algorithm with the three data sets as mentioned in Chapter 5.3, the results depicted in Figure 6.8 are obtained. A key observation is that only frequency offset plays a significant role. In contrast, the frequency drift appears to be either unnoticeable or entirely absent in the results. This observation is supported by the absence of a visible parabolic curve.

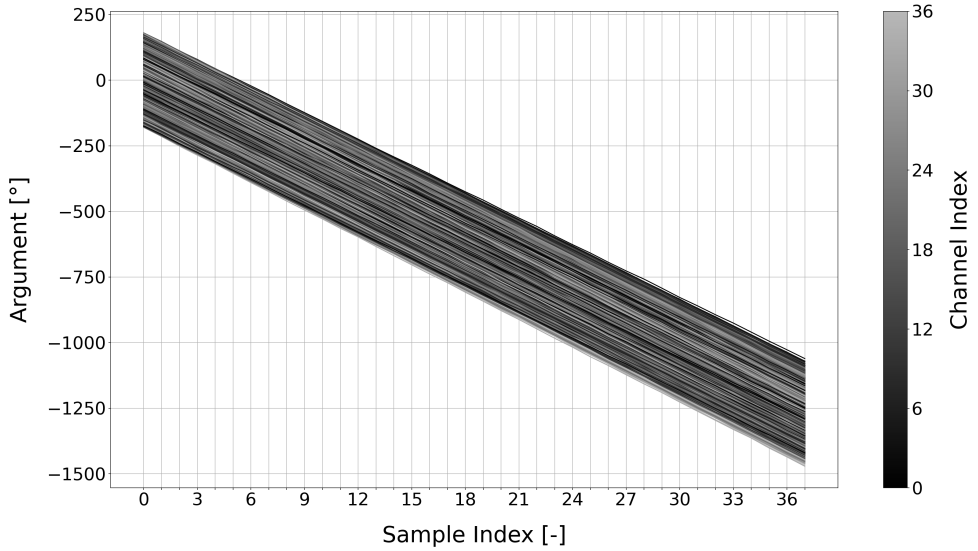

Figure 6.7: Unwrapped arguments of the reference antenna ANT13

When the LLS algorithm is employed with all reference samples and the data sample corresponding to the sample indices 1, 36, and 37, it consistently yields the lowest RMSE. Hence, this specific algorithm configuration is utilized throughout this thesis when frequency compensation is applied, unless otherwise stated.

Comparable results are obtained for the transmit powers 2.0 and -8.5 dBm. The LLS algorithm, with the same sample indices, continues to yield the lowest RMSE across all transmit powers. The only noticeable difference is an increase in RMSE as the transmit power decreases. This is to be expected as a decrease in signal strength leads to a corresponding decrease in SNR for a fixed environment.

6.7 Evaluation of All Incident Angles

As a measure of validation, the data collected during the antenna compensation measurements and data measurements are evaluated. This evaluation primarily focusses on the performance of the antenna array across all incident angles.

Prior to the evaluation, frequency compensation is applied to the data, rendering it usable. From this data, a single snapshot is extracted for each collected Bluetooth packet, with each snapshot corresponding to a single sample on each antenna. This results in a total of 1000 snapshots per incident angle for the antenna compensation measurements.

The results of this evaluation are visually represented in Figure 6.9. To maintain clarity and simplicity, only the results obtained from the MUSIC algorithm are

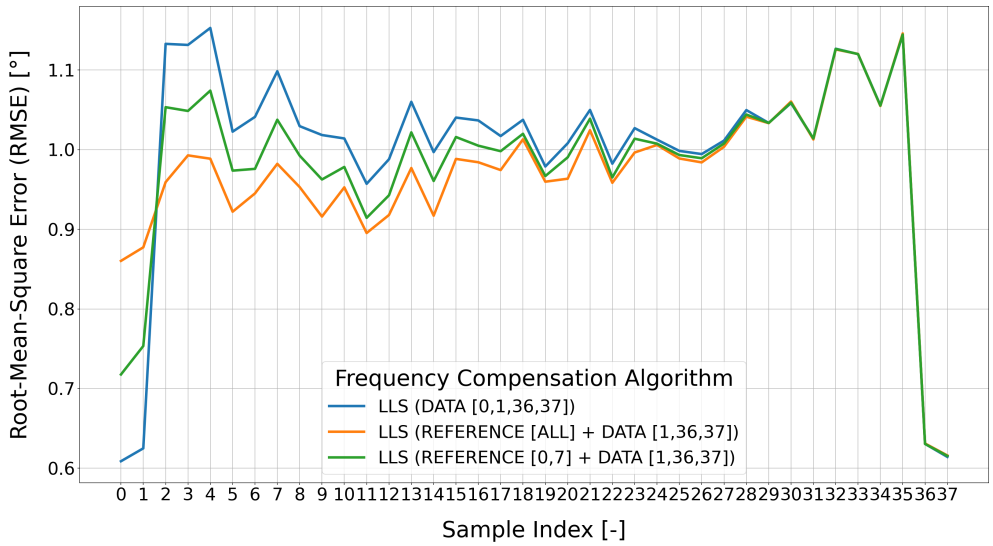

(a) Performance frequency compensation algorithms

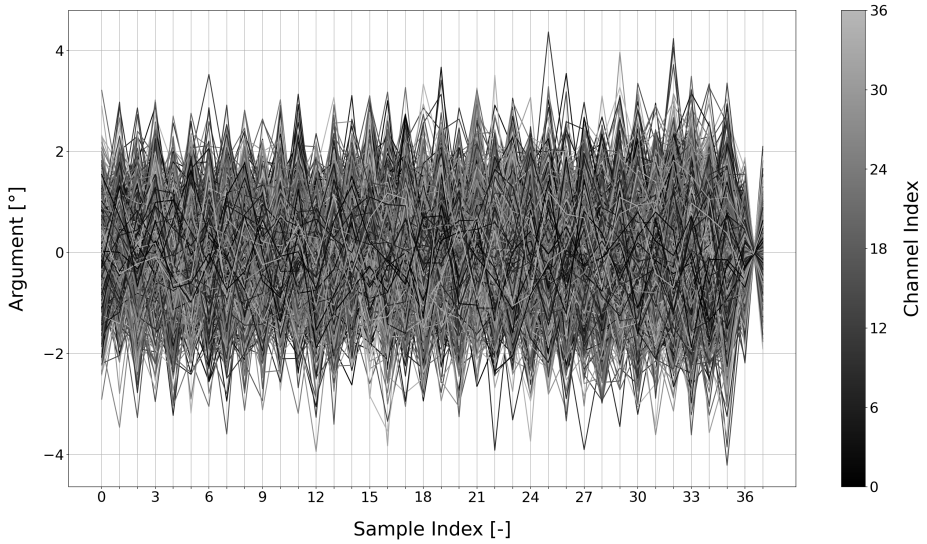

(b) Unwrapped argument after applying LLS (REFERENCE [ALL] + DATA [1,36,37])

Figure 6.8: Performance comparison frequency compensation algorithms and unwrapped arguments

displayed due to its slightly superior performance. However, the estimated incident angles for all four DoA estimation algorithms are available in the Appendix B.

These results consider only a transmit power of 8.5 dBm and horizontal polarization. The choice of horizontal polarization was made due to its consistent alignment throughout the measurements. For the azimuth errors, the incident angle corresponding to an elevation of 0° is excluded. The potential misalignment between

the tag and anchor can produce any azimuth angle. For the elevation errors, the incident angles corresponding to an elevation of 75° and 85° are excluded. The returned estimated incident angles reach their maximum of 90°, providing no additional information.

All 36 Bluetooth channels are used during the data collection, with each channel corresponding to a distinct wavelength. Given that the DoA estimation algorithms consider a single wavelength for estimating the incident angle and assuming a uniform distribution across all channels, the central wavelength is selected for use. This corresponds to a wavelength of 0.122795 meters.

The azimuth error appears to converge as the elevation increases. Upon examination of the estimated azimuth provided in Appendix B, it becomes evident that the combined estimated azimuth approaches 180° as the elevation increases. This trend suggests a potential misalignment between the tag and anchor. On the other hand, the elevation error increases as the elevation increases. This is an anticipated outcome considering that the antenna array employs dual polarized patch antennas.

Interestingly, an equal offset seems to exist between the elevations of 15°, 30°, 45° and 60° for both azimuth angles. The difference in error ranges from a minimum of 3.96° to a maximum of 4.35°. The mean elevation offset error is 2.08°, which closely matches the elevation error found at an elevation of 0°.

A similar analysis is conducted for the data measurements, with the primary distinction that both horizontal and vertical ports are utilized. The outcomes are visually represented in Figure 6.10 for the horizontal port and Figure 6.11 for the vertical port. The estimated incident angles for all four DoA estimation algorithms can be found in Appendix B. Another notable difference is that the data consists of 500 captured Bluetooth packets instead of 1000 packets. Since one snapshot is extracted per Bluetooth packet, a total of 500 snapshots are available. Once again, the azimuth error corresponding to an elevation of 0° and the elevation errors corresponding to elevations of 75° and 85° are excluded.

A significant performance discrepancy is observed between the horizontal and vertical ports, with the vertical port outperforming the horizontal port in nearly all conducted measurements. The azimuth errors observed on the horizontal port are to be expected due to the roll changes that occur when altering the azimuth. This results to a misalignment between the anchor and tag. As the azimuth approaches 0°, a misalignment in polarization occurs, leading in an expected drop in performance. Similar patterns are observable for the elevation error at larger elevation angles, although the impact on the elevation of 30° or less is relatively insignificant.

In stark contrast, the results obtained from the vertical port remain relative constant across all azimuth angles. As the azimuth deviates from 0°, a misalignment in polarization occurs. This effect is only marginally noticeable for the azimuth of ±75°.

The elevation error, contrary to expectations, improves as the azimuth diverge from 0°.

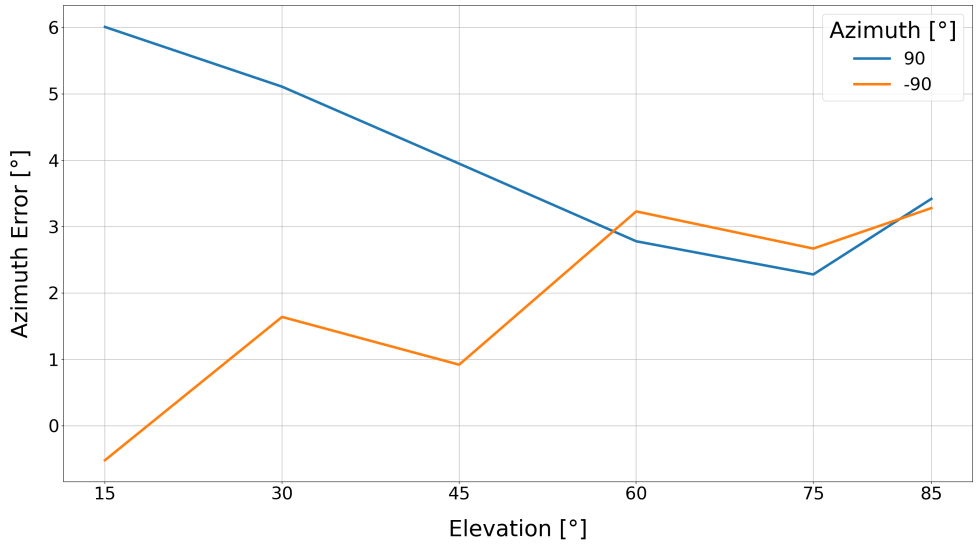

(a) Error in azimuth

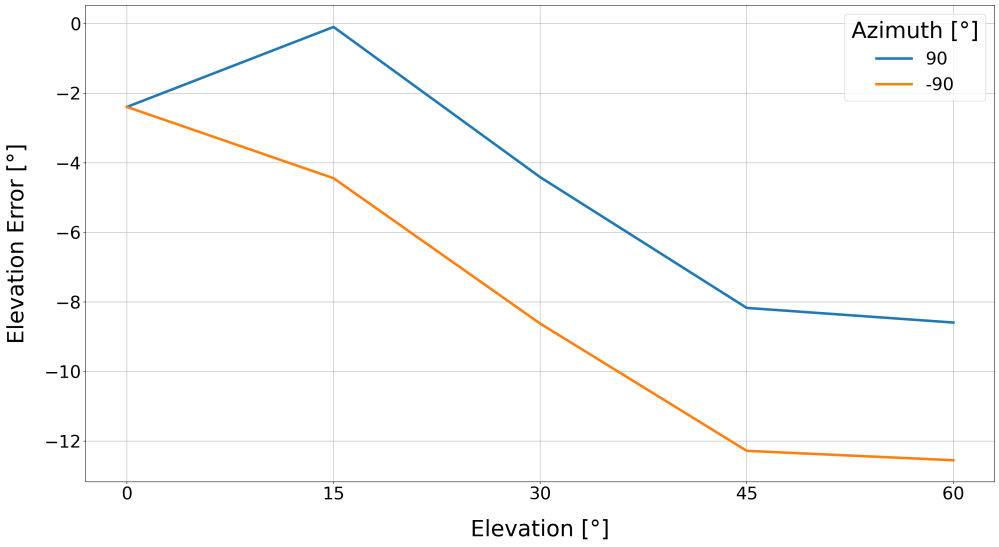

(b) Error in elevation

Figure 6.9: Azimuth and elevation error antenna compensation measurements horizontal port

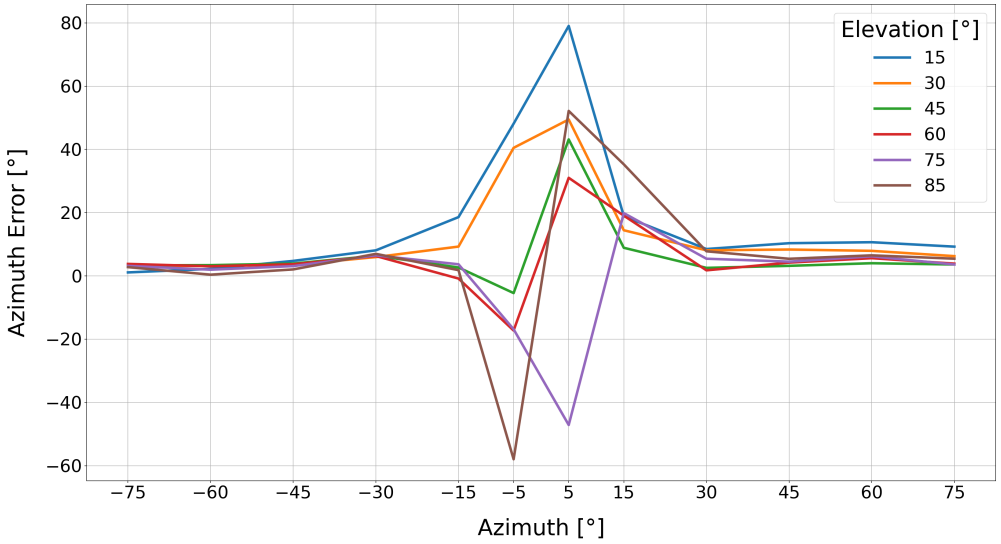

(a) Error in azimuth

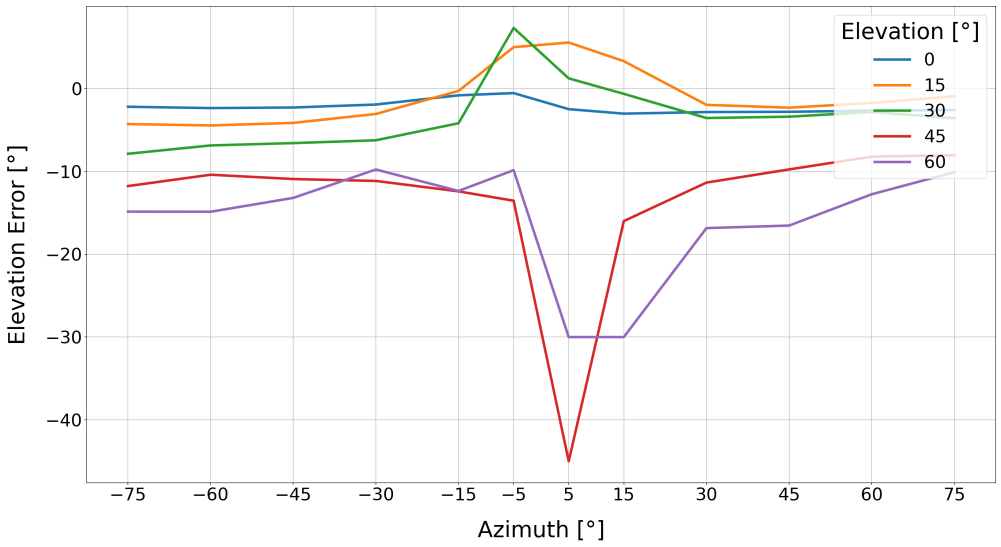

(b) Error in elevation

Figure 6.10: Azimuth and elevation error data measurement horizontal port

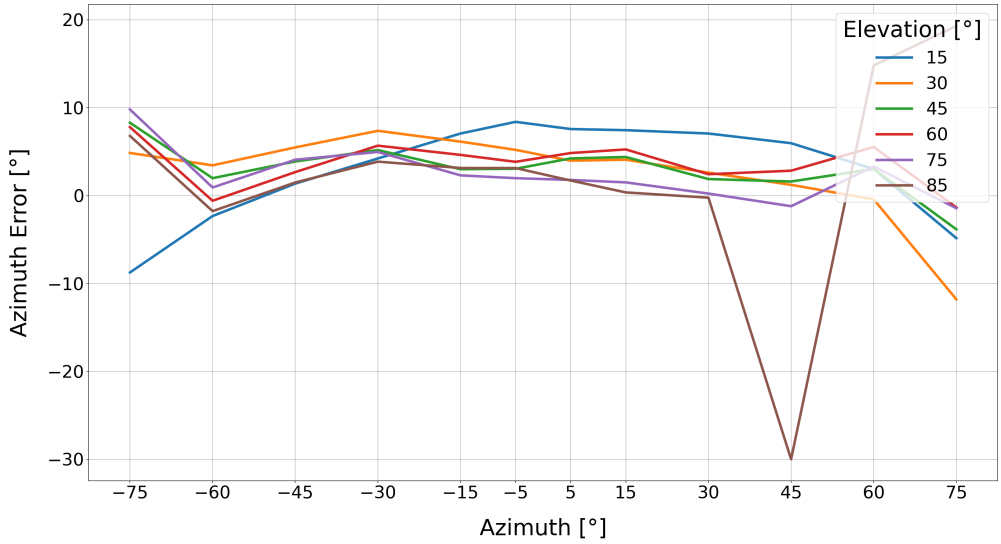

(a) Error in azimuth

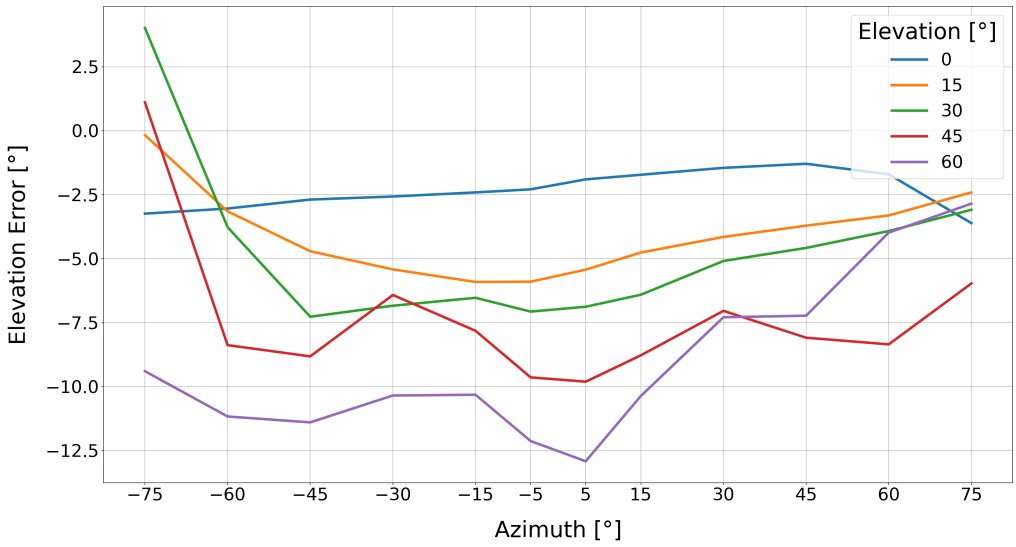

(b) Error in elevation

Figure 6.11: Azimuth and elevation error data measurements vertical port

6.8 Results Parameter Sweep

The measurements conducted in the anechoic chamber at ASTRON are designed to allow for variations in the number of snapshots, number of antennas, and the SNR. This section assesses the impact of these parameters on IQ samples obtained from a real-world antenna array. For these parameters, an alignment in polarization of

the anchor and tag is used. Two incident angles are used, specifically azimuth 90° at an elevation of 15° and 45°, to verify if there is any discrepancy between incident angles. The results are obtained after frequency compensation is applied.

Number of Snapshots

The first parameter evaluated is the number of snapshots. A total of 1000 Bluetooth packet are obtained, with a single snapshots per Bluetooth packet, resulting in a total of 1000 available snapshots. The transmit power used is -8.5 dBm. The range of snapshots spanned from 1 to 100 with a step size of one. The data is partitioned into chunks of the desired length for each snapshot. The results for an azimuth of 90° at an elevation of 15° and 45° are depicted in Figure 6.12a and Figure 6.12b, respectively.

The results for the MVDR are truncated to observe the behavior of the other DoA estimation algorithms at a lower snapshot count. It can be observed that all DoA estimation algorithms perform similarly, except for the MVDR at a low snapshot count. The performance limit of the other algorithms is already reached when the snapshot count is below 10, indicating a high SNR even for a lowest transmit power of -8.5 dBm.

Number of Antennas

Next, the number of antennas is varied while maintaining a constant transmit power of -8.5 dBm. A snapshot count of 25 is used, as increasing the snapshot count yield similar performance. The antenna array used has a 4x4 configuration, which is therefore the largest square antenna array configuration possible. The 4x4 antenna array also facilitates the creation of two other square antenna array configurations, namely 2x2 and 3x3. For the 2x2 configuration, the inner antennas ANT10, ANT6, ANT11, and ANT7 are used to preserve the same center as the 4x4 configuration. However, maintaining the same center is not feasible for the 3x3 configuration. Therefore, the antennas ANT10, ANT6, ANT2, ANT11, ANT7, ANT3, ANT12, ANT8, and ANT4 are used. The results obtained are depicted in Figure 6.13.

As can be seen, antenna configurations with fewer antennas outperforms larger ones in all instances. This contradicts the theory that a greater number of antennas should provide a more accurate estimation of the incident angle. Several factors contribute to this unexpected outcome. Firstly, the real-world measurements are not ideal, as evidenced by the observed misalignment between the anchor and tag. Secondly, the antennas used are not identical. For the 2x2 configuration, only the inner antennas with approximately equal mutual coupling are used. In contrast, both inner and outer antennas are used for the other configurations. Lastly, a high SNR was noted, suggesting that a smaller number of antennas may be sufficient for ac-

curately estimating the incident angle.

Signal-to-Noise Ratio

The final parameter adjusted is the SNR. Given the difficulty in determining the SNR when introducing noise to the measurement setup, the transmit power is varied instead. The transmit power used are 8.5, 2.0, and -8.5 dBm, corresponding to an average RSSI of -53.58, -60.82, and -71.36 dBm respectively for an elevation of 15°. For an elevation of 45°, the average RSSI of -52.01, -58.99, and -69.33 dBm was observed respectively. The 1000 snapshots are partitioned in chunks of 25 snapshots. Using all 16 antennas from the antenna array, the results shown in Figure 6.14 are obtained.

Each DoA estimation algorithm demonstrates a slight improvement when the transmit power is increased. In addition, a nearly constant RMSE offset can be observed among the algorithms. However, these improvements and the offsets are minimal and thus can be considered negligible. This primarily suggests that the SNR is too high to observe a significant improvement in the estimation of the incident angle.

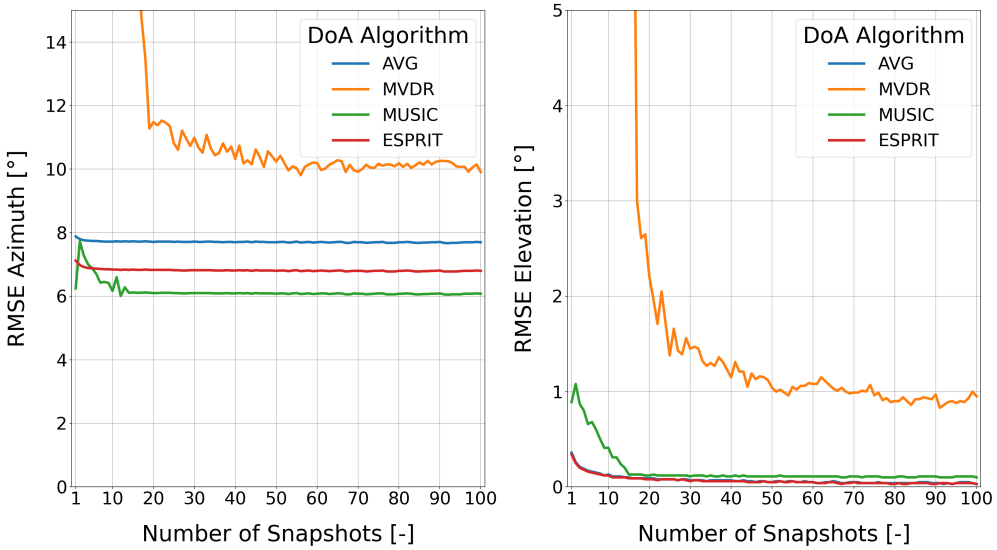

(a) Azimuth 90° and elevation 15°

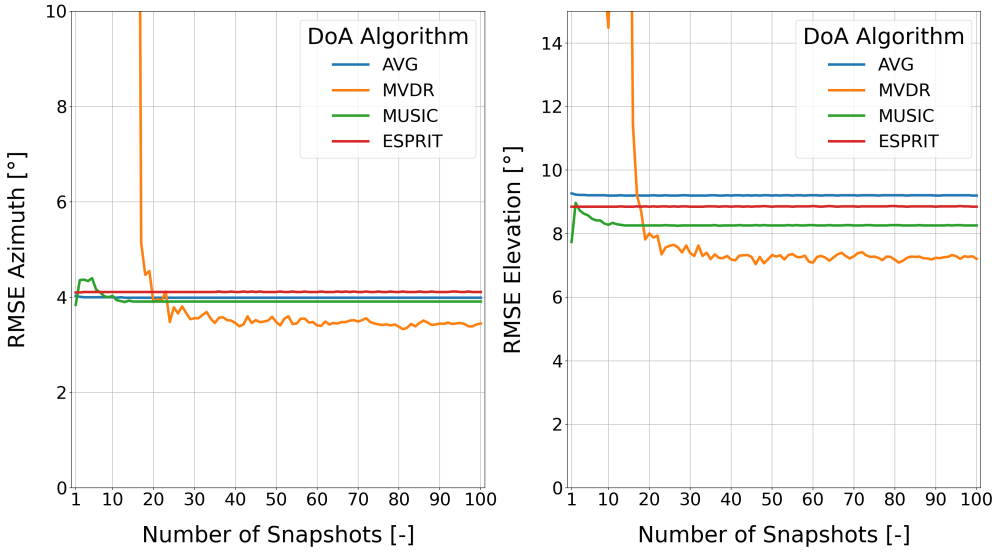

(b) Azimuth 90° and elevation 45°

Figure 6.12: RMSE versus snapshot count

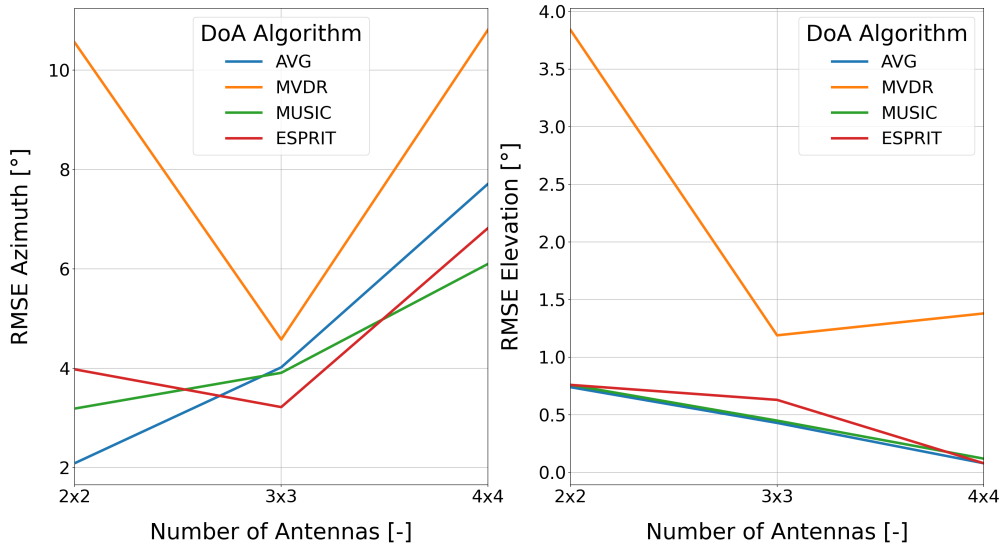

(a) Azimuth 90° and elevation 15°

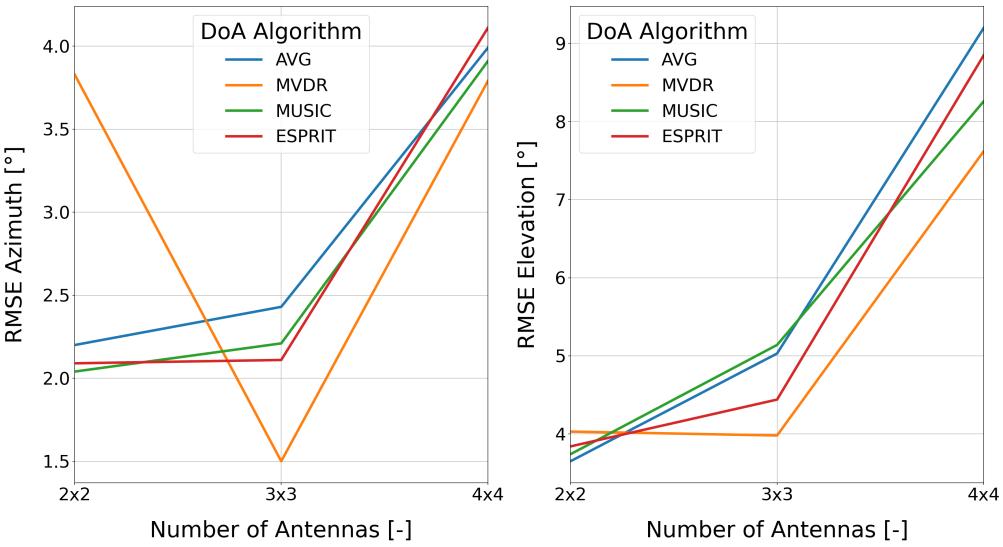

(b) Azimuth 90° and elevation 45°

Figure 6.13: RMSE versus number of elements in the antenna array

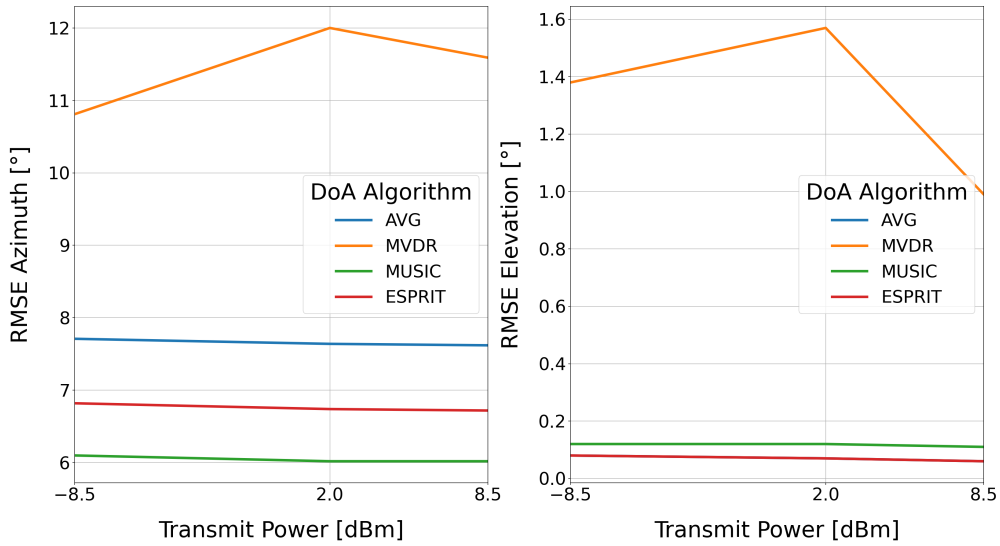

(a) Azimuth 90° and elevation 15°

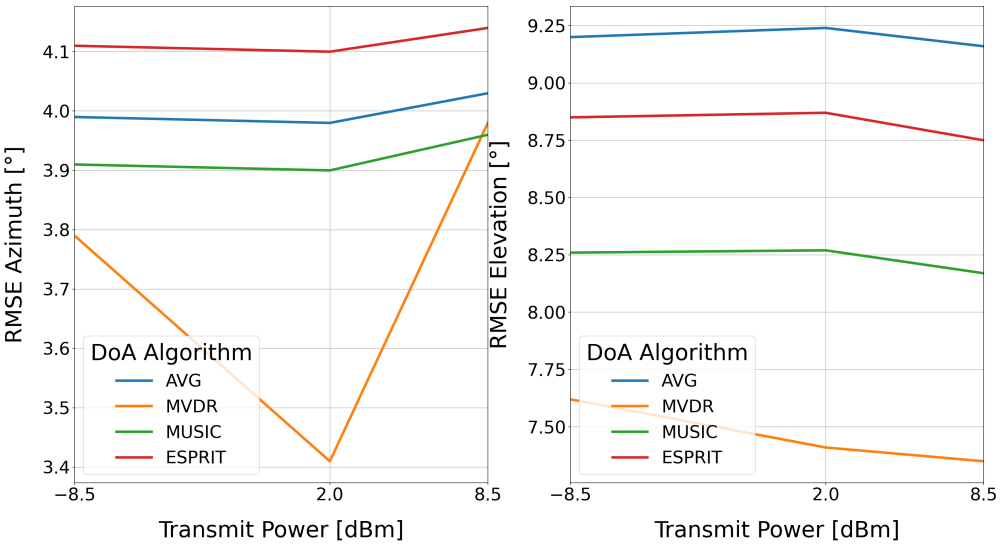

(b) Azimuth 90° and elevation 45°

Figure 6.14: RMSE versus transmit power

6.9 Antenna Compensation

During the measurements performed in the anechoic chamber at the University of Twente, a significant spread in the unwrapped arguments was observed after frequency compensation. Figure 6.15 depicts the spread on the antenna elements of the BG22-RB4191A for 1000 Bluetooth packets. These results were obtained at an

incident angle of 0° azimuth and 0° elevation with the switching pattern:

[ANT1, ANT1, ANT1, ANT1, ANT2, ANT2, ANT3, ANT3, ANT4, ANT4, ANT5, ANT5, ANT6, ANT6, ANT7, ANT7, ANT8, ANT8, ANT9, ANT9, ANT10, ANT10, ANT11, ANT11, ANT12, ANT12, ANT13, ANT13, ANT14, ANT14, ANT15, ANT15, ANT16, ANT16, ANT1, ANT1, ANT1, ANT1]

The measurements were conducted with the polarization of the anchor and tag aligned. To ensure consistency in the argument spread from these measurements, a power cycle was performed by disconnecting and reconnecting power. The results confirmed that the arguments spread was not affected by the power cycle.

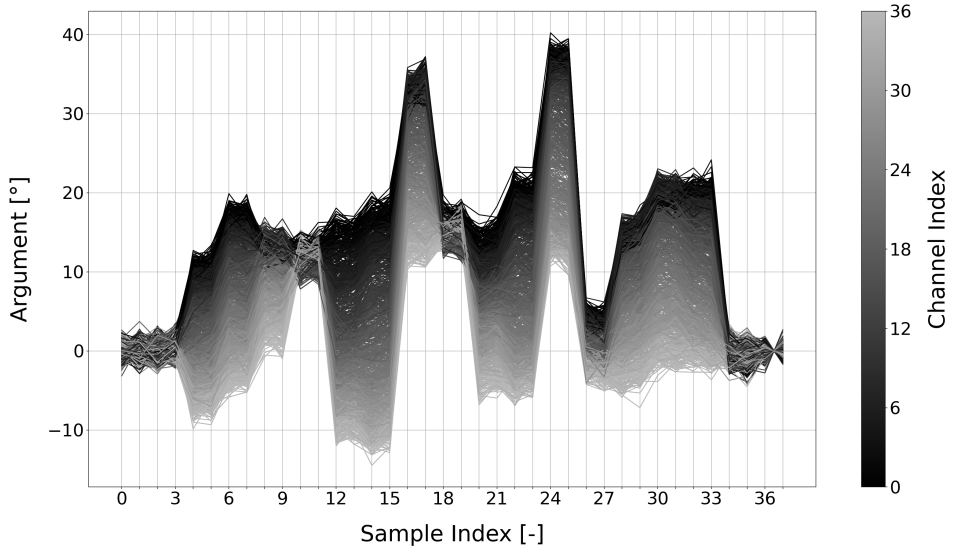

Figure 6.15: Argument spread of data from anechoic chamber University of Twente

To ascertain that these observations were specific to a particular antenna array, an additional antenna array, designated as CHW1010-ANT2-1.0, was tested under similar conditions. Comparable results were obtained for this antenna array, thereby confirming the consistency of the observation across different antenna arrays. However, for the subsequent results and analysis exclusively the antenna array from Silicon Labs was used. This was primarily due to the length mismatch in transmission line between the inner and outer antenna elements of the CHW1010-ANT2-1.0.

To mitigate the argument spread present in the results, two methods of antenna compensation are introduced. The first method is termed as antenna deviation compensation. In this approach, the mean argument is computed for each antenna within the array across all Bluetooth channels. Subsequently, an average is calculated for each Bluetooth channel. This average is then subtracted from the mean

value to yield the desired deviation value. The outcome of this process is an antenna compensation matrix with dimensions equivalent to the number of antennas in the array by the number of channel indices.

The second method is antenna deviation and mean compensation. This method extends upon the first method of antenna compensation by incorporating mean compensation. Ideally, an elevation angle of 0° should result in no phase difference between antennas in an array. However, this is dependent on the time that the signal is sampled. Therefore, to accurately apply this compensation, first frequency compensation is applied. This aligns the samples taken at the antennas closely to 0°. Consequently, a compensation matrix with identical dimensions is obtained, but now it includes both deviation and mean compensation.

To verify the impact of antenna compensation on the estimated incident angles, data collected during the antenna compensation measurements was used. This data is selected to once again keep the polarization aligned. Figure 6.16 shows the spread of the unwrapped angles at an elevation angle of 0°. A significant decrease in spread can be observed. Moreover, the gradient, characterized by lower frequency at the upper end and higher frequencies at the lower end of the spread, is no longer present. The discontinuities observed between the antenna elements can be attributed to a minor misalignment between the anchor and tag.

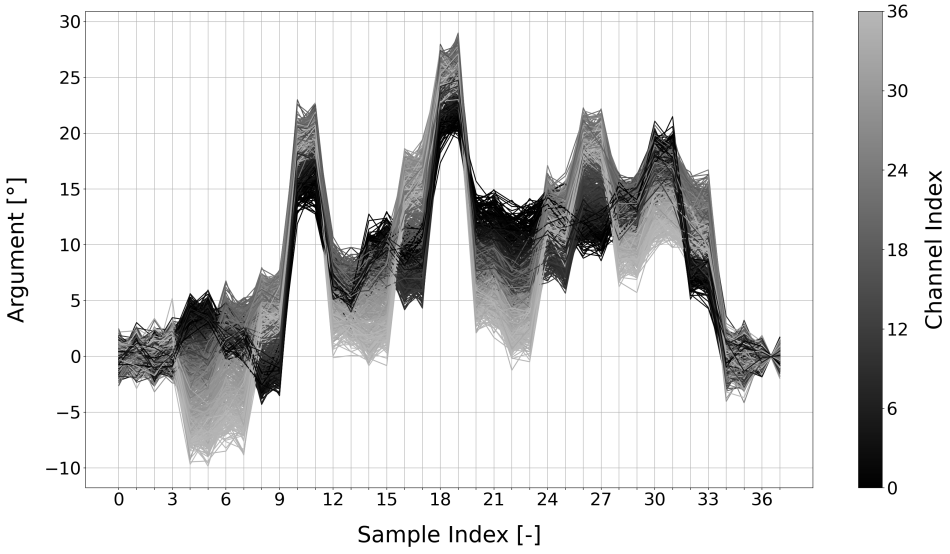

Figure 6.16: Argument spread in final measurements

In the first experiment, antenna deviation compensation is applied and the difference between the estimated incident angles with only frequency compensation and those with both frequency compensation and antenna deviation compensation is calculated. The results of this calculation can be found in Table 6.1. It is evident

that the improvement for the DoA estimation algorithms AVG, MUSIC, and ESPRIT is within a range of -0.24° and 0.18°, which is negligible. However, upon examination of the MVDR algorithms, it is apparent that while improvements are more substantial, they are predominantly negative.

Table 6.1: Comparison frequency compensation versus frequency compensation and antenna deviation compensation

Reference Angles		AVG		MVDR		MUSIC		ESPRIT	
Az.	El.	Az.	El.	Az.	El.	Az.	El.	Az.	El.
90	15	0.04	0.02	1.92	-0.15	0.06	0.00	0.08	0.01
90	30	0.00	0.01	1.06	1.04	-0.03	-0.02	-0.03	-0.02
90	45	0.01	-0.17	0.48	0.43	0.00	0.00	0.01	0.00
90	60	0.01	-0.16	1.00	0.00	-0.01	0.03	-0.01	0.05
90	75	-0.01	0.14	0.19	0.00	0.00	0.00	0.02	0.00
90	85	-0.01	-0.24	-0.82	0.00	-0.02	0.00	0.00	0.00
-90	85	0.00	0.14	-0.80	0.00	-0.01	0.00	-0.01	0.00
-90	75	-0.01	-0.15	-0.13	0.00	0.01	0.00	0.01	0.00
-90	60	0.01	0.18	-1.73	-4.01	0.00	0.01	-0.01	-0.01
-90	45	0.00	-0.01	1.50	-4.71	0.02	-0.02	0.03	-0.02
-90	30	-0.01	-0.01	-0.14	-0.86	-0.01	0.01	-0.01	0.00
-90	15	-0.02	0.00	-1.86	0.55	0.00	-0.01	0.00	-0.02

Next, the same procedure is applied, but this time with antenna deviation and mean compensation instead of only antenna deviation compensation. The results can be found in Table 6.2. This time patterns can be detected. When examining only the elevation, improvements can be almost exclusively found for an azimuth of -90°. This approximately corresponds to the average elevation offset of 2.08°, which corresponds to the misalignment of the anchor and tag. Similar results can be observed for the azimuth. The first experiment is also performed for the transmit powers 2.0 and -8.5 dBm. Again, similar results were observed.

In the second and final experiment, the snapshot count was altered. For the first experiment, 1000 snapshots corresponding to 1000 Bluetooth packets were used. This allowed for a more accurate determination of the incident angle as it includes multiple times all Bluetooth channels. For this experiment, a snapshot count from the list [1, 2, 3, 4, 5, 6, 7, 8, 9, 10, 20, 30, 40, 50] was used. This allowed for the partitioning of the 1000 snapshots in the desired chunk size to get the RMSE. The

Table 6.2: Comparison frequency compensation versus frequency compensation and antenna deviation and mean compensation

Reference Angles		AVG		MVDR		MUSIC		ESPRIT	
Az.	El.	Az.	El.	Az.	El.	Az.	El.	Az.	El.
90	15	4.57	-2.41	6.40	-3.09	3.49	-2.23	4.20	-2.13
90	30	2.07	-2.90	3.96	-1.57	1.73	-2.73	2.11	-2.72
90	45	1.41	-3.63	2.55	-3.39	1.18	-4.00	1.61	-4.86
90	60	1.18	0.53	2.42	-7.72	0.94	-7.56	1.27	-10.87
90	75	1.15	-1.18	2.29	0.00	0.93	0.00	1.12	0.00
90	85	1.13	-3.34	1.31	0.00	1.06	0.00	1.13	0.00
-90	85	-1.04	3.90	-1.92	0.00	-0.97	0.00	-1.02	0.00
-90	75	-1.01	5.30	-1.64	0.00	-0.96	0.00	-1.26	0.00
-90	60	-1.14	-0.52	-3.55	2.05	-1.19	6.21	-1.36	6.59
-90	45	-1.33	2.77	0.14	0.25	-1.31	3.87	-1.68	3.91
-90	30	-1.91	2.99	-1.87	1.44	-1.81	2.83	-2.06	3.20
-90	15	-1.67	2.54	-2.75	2.59	-1.77	2.47	-0.10	3.10

focus was solely on the performance of the antenna deviation compensation to exclude any misalignment and to only examine the spread. The results for all incident angles are provided in Appendix C. The improvement is observed to range between -0.58° and 0.53°. With the total range slightly exceeding 1°, these improvements are also deemed negligible due to the lack of consistency. It is evident that the compensation is more substantial with fewer snapshots and decreases as the number of snapshots increases.

6.10 Conclusion

The evaluation of frequency compensation algorithms was assessed using captured IQ samples from the same antenna. A prominent frequency offset, independent of the center frequency, was observed in the unwrapped angles. In contrast, the unwrapped angles exhibit no noticeable frequency drift. Upon applying the LLS algorithm to these unwrapped angles, a RMSE of less than 1.2° was achieved at a transmit power of 8.5 dBm. This demonstrated the adequacy of the LLS algorithm for frequency compensation, particularly in scenarios characterized by the presence of frequency offset.

Following this, the data collected at all incident angles from the measurements conducted at ASTRON were evaluated. The incident angles were estimated using the data available at each respective angle. Two distinct measurements were performed: antenna compensation measurements and data measurements.

For the antenna compensation measurements, the focus was exclusively on the horizontal port due to the alignment in polarization between the tag and anchor. The azimuth error was observed to converge to approximately 3° as the elevation increased, indicating a misalignment between tag and anchor. The elevation error was found to increase with the elevation, a phenomenon attributed to the radiation pattern of the patch antennas among other factors. Additionally, a fixed elevation error offset was identified, corresponding to a mean of 2.08°, closely matching the elevation error found at an elevation of 0°.

In contrast, for the data measurements, both horizontal and vertical ports were evaluated. For the horizontal port, as the azimuth approaches 0°, a decline in performance was observed. This decline coincides with an increase in the misalignment in polarization between the tag and anchor. A significant performance discrepancy was observed between the horizontal and vertical port, with the vertical port outperforming the horizontal port in nearly all incident angles. The underlying cause of this discrepancy remains unidentified.

Subsequently, the influence of the three key parameters - number of snapshots, number of antennas, and SNR - on the precision of the estimated incident angle was assessed. It was observed that the majority of DoA estimation algorithms reach their performance limit at a snapshot count of less than 10. This suggests that the SNR is excessively high, even for the lowest transmit power of -8.5 dBm. Interestingly, the MVDR exhibited a different behavior, requiring a substantially higher number of snapshots to estimate the incident angle accurately.

When considering the number of antennas, configurations with fewer antennas unexpectedly outperformed larger ones in all instances. This outcome contradicts theoretical expectations. However, several factors contribute to this unexpected outcome. These factors include the misalignment of the tag and anchor, as well as the antennas used in each configuration.

When the SNR was varied by adjusting the transmit power, negligible improvements were observed for all DoA estimation algorithms as the transmit power increases. This once again indicates a high SNR for all transmit powers.

Finally, measurements conducted at the University of Twente revealed a significant spread in unwrapped arguments after frequency compensation. Two methods of antenna compensation were introduced and applied, leading to both a decrease and increase in spread. However, most improvements for the DoA estimation algorithms were negligible. More substantial improvements were observed with the

MVDR algorithm, but they were predominantly negative. The effectiveness of the compensation method varied depending on the snapshot count and transmit power. A primary cause of the negligible improvements is that the methods are applied to the antenna compensation measurements, which already revealed a significant reduction in the spread.

Chapter 7

Discussion

In Chapter 5, an evaluation of DoA algorithms were conducted through simulation, assuming a single impinging signal. However, it is crucial to consider that in real-world scenarios, the deployment of multiple tags and anchors is typical. This can lead to the collision of Bluetooth packets. Furthermore, the 2.4 GHz ISM band is shared by a multitude of devices and protocols, which can potentially lead to interference. As a result, it becomes virtually impossible to completely avoid collisions and interference. In order to mitigate this issue, Bluetooth technology employs a technique known as AFH. This technique facilitates the distribution of Bluetooth packets across the entire frequency spectrum. Given that multiple snapshots are captured, a diverse range of channels is utilized. This effectively reduces the probability of collisions and interference. In addition, Bluetooth technology provides the capability to maintain a channel map. This feature allows for the exclusion of channels from the usable channels if they are found to be prone to errors. Therefore, further enhancing the robustness and reliability of the system in real-world scenarios. Given the advanced features and capabilities of Bluetooth technology designed to mitigate interference, it is reasonable to assume a single impinging signal.

In Chapter 6.7 a significant discrepancy was observed between the error in elevation and azimuth for the antenna compensation measurements. The issue with the measurement setup at ASTRON is that the center of rotation does not coincide with the center of the antenna array. A top view sketch of the setup is provided in Figure 7.1.

The antenna array was mounted onto a tube, which subsequently was inserted into and secured to the positioner as described in Appendix A. Due to the inherent design of the positioner, there is a misalignment between the center of the antenna array and the center of rotation. This misalignment leads to a discrepancy between the set elevation angle and the actual elevation angle. It is important to note that this error influences only the elevation angle, as it is contingent on the yaw. The azimuth remains unaffected as it is solely dependent on the roll.

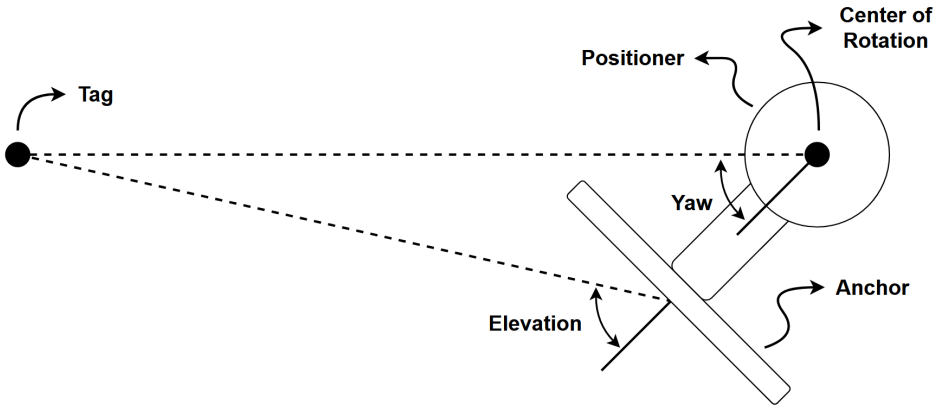

Figure 7.1: Top view sketch measurement setup ASTRON

The distance between the tag and center of rotation is approximately 3 meters. The exact distance between the center of the antenna array and center of rotation remains uncertain but is estimated to be within a range of 10 to 40 cm. Consequently, Table 7.1 has been constructed to estimate the actual elevation angle for various distances between the center of the antenna array and center of rotation for a set of elevation angles.

Table 7.1: Set elevation versus actual elevation

Elevation [°]	Center antenna array to center of rotation [cm]			
	10	20	30	40
15	15.5	16.1	16.6	17.3
30	31.0	32.0	33.1	34.3
45	46.4	47.8	49.4	50.9
60	61.7	63.4	65.2	67.1
75	76.9	78.7	80.7	82.6
85	86.9	88.8	89.3	87.3

When accounting for the elevation angle offset, it becomes evident that misalignment of the centers has a significant impact. This impact however decreases as the elevation angle increases.

Upon analyzing the results for frequency compensation, it was observed that the empirical measurements primarily exhibit frequency offset, with no discernible evidence of frequency drift. As a result, during the simulation phase, no algorithms were proposed or implemented with the objective of compensating for frequency drift. Nonetheless, a reference was made regarding potential compensation strate-

gies in the event of frequency drift. Additionally, graphical representations were included to illustrate the expected parabolic curve in the event of a constant frequency drift scenario. The height of this curve is dependent on the magnitude of the frequency drift, highlighting the potential implications of frequency drift.

Upon comparing the results derived from the simulation and real-world data for parameters such as the number of snapshots, number of antennas, and SNR, several notable differences were observed. The range in transmit powers was found to be insufficient to achieve a wide range of SNRs. Initially, the lowest transmit power of -27.5 dBm was included. Unfortunately, during the final measurements, Bluetooth packets could not be properly received at this transmit power and it was therefore omitted. The high SNR is primarily evident in the plot of the transmit power, as the improvements when increasing the transmit power are negligible, indicating that the limit has already been reached. This is further confirmed when altering the snapshot count, where a few snapshots are sufficient to reach the limit. Consequently, it is challenging to ascertain where exactly the real-world data aligns with the simulations. Moreover, in the simulations, factors such as mutual coupling between antennas and other imperfections are not accounted for.

In an effort to understand why the performance of the MVDR deteriorates at a low snapshot count for the real-world data, the spectrum of the MVDR was examined. In Figure 7.2 the spectrum of the MVDR is shown for a snapshot count of 10 with an incident angle of 90° azimuth and 45° elevation. As can be observed, the spectrum contains multiple peaks. Although there is a peak at the incident angle, this peak is lower than some of the other peaks. Therefore, an incorrect incident angle is returned. By increasing the number of snapshots, the other peaks diminish while the peak corresponding to the correct incident angle is amplified.

During the simulations of the four DoA estimation algorithms, a significant difference in RMSE between the azimuth and elevation was observed for the AVG algorithm. These simulations utilized an incident angle of 90° azimuth and 45° elevation to ensure consistency with the conducted measurements. The limitation of this incident angle is that only the elevation is noticeable and can be estimated using the average phase difference in the y-direction. This stands in contrast to the azimuth, where the average phase difference in both directions can be used to estimate the azimuth. Changing the azimuth to allow for a phase difference observable in both directions resulted in an improvement in the RMSE of the elevation. This is due to the fact that the elevation angle can be estimated from the average phase difference in both directions. Furthermore, reducing the elevation angle also improves the accuracy. As the elevation angle approaches 0°, irrespective of the azimuth, the phase difference between antennas converges to 0°.

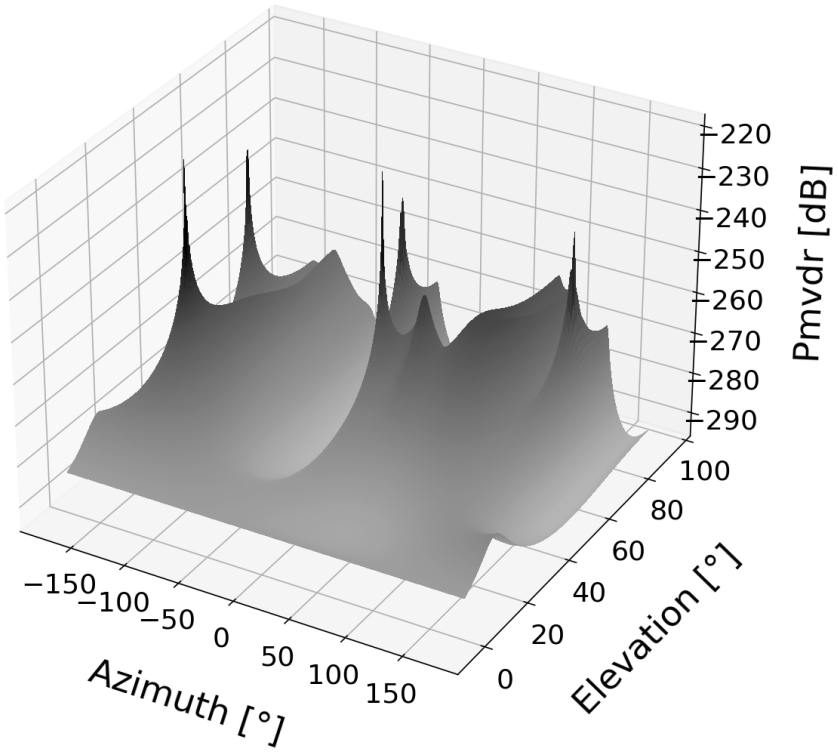

Figure 7.2: MVDR spectrum antenna compensation measurements

Chapter 8

Conclusions

This research aimed to assess the performance of a URA within the context of Bluetooth technology. Four research questions were formulated for this purpose:

1. Based solely on the Bluetooth Core Specifications, what are the unique configurations of tags and anchors, and what rate can the angle of incidence be estimated?
2. How do computational costs of DoA estimation algorithms compare between ULA and URA?
3. Considering the Bluetooth technology, what accuracy is theoretical achievable using DoA estimation algorithms in combination with a URA and how does this compare to the accuracy of commercially available URAs?
4. What techniques can be used to reduce the argument spread between Bluetooth packets on different channels, and how do they affect the accuracy?

In addressing the first research question, a total of eight unique configurations were identified. These configurations are a combination of the communication mode, direction finding method, and antenna composition. The communication mode can be either connectionless or connection-oriented. The direction finding method can be either AoA or AoD. As for the antenna composition, it can be arranged in two ways: either the tag is equipped with a single antenna and the anchor with an array of antennas, or vice versa. Each configuration presents its own set of advantages and disadvantages, offering a range of options for different application scenarios.

The rate at which samples can be collected to estimate the angle of incident was found to be dependent on the communication mode. In the connectionless mode, after synchronization, the minimum time between two packets containing a CTE is the length of the packet (*AUX_CHAIN_IND*) plus 300 µs (T_MAFS). In the connection-oriented mode, once a connection is established, this minimum time is dependent on the length of two packet (*LL_CTE_REQ* and *LL_CTE_RSP*) plus twice 150 µs (T_IFS). When the device allows only for a single packet to be transmitted

each interval, the minimum time is 7.5 ms for both communication modes.

In relation to the second research question, four DoA estimation algorithms were examined: AVG, MVDR, MUSIC, and ESPRIT. These algorithms can be categorized into two methods: spectral-based and parametric. MVDR and MUSIC fall under spectral-based methods, while AVG and ESPRIT are classified as parametric methods. The computational complexity of these four DoA estimation algorithms was explored in detail in Chapter 4.

The dominant factors in the computational complexity of spectral-based methods are tied to the exploration of the entire spectrum. When comparing a ULA to a URA, the spectrum that needs to be examined is increased by a factor of 180, which is reflected in the computational complexity. On the other hand, the computational complexity of parametric methods is primarily dependent on the snapshot count and the number of elements in the antenna array. For the AVG algorithm, the increase in computational complexity, when comparing a ULA to a URA, is less than a factor of two. The increase for the ESPRIT algorithm is even lower as the dominant terms remain the same.

Regarding the third research question, the performance of the DoA estimation algorithms was evaluated through simulation using three key parameters: SNR, snapshot count, and the number of antennas. All algorithms, except for the AVG, demonstrated comparable performance, which began to decline when the SNR dropped below 0 dB at a snapshot count of 25 and a 4x4 antenna array configuration. The AVG algorithm's performance was found to be dependent on the incident angle and started to degrade when it fell below 10 dB in the worst-case scenario.

When examining the snapshot count and number of antennas, these parameters were observed to approach a limit set by the SNR. For a SNR of 5 dB and a 4x4 antenna array configuration, this limit was reached after approximately 25 snapshots. The MVDR algorithm was observed to require more snapshots to accurately determine the incident angle. Moreover, it was noted that the RMSE of the MVDR algorithm starts to increase once it goes beyond a 4x4 antenna array configuration. The precise cause behind this behavior remains unclear.

The same three key parameters were evaluated using the data from the field measurements. However, a significant frequency offset was detected in the collected data, rendering it unusable without correction. The LLS algorithm was found to deliver the best performance, with a RMSE of less than $1.2°$ at a transmit power of 8.5 dBm, using all the reference samples and the data samples corresponding to the sample indices 1, 36, and 37.

For the collected data, it was found that the transmit powers was insufficient to achieve an appropriate range of SNRs, in contrast to the simulations. This was further confirmed by the observation that the limit was reached with a low snapshot

count. The MVDR algorithm is an exception, as it required at least 20 snapshots to approach the limit. Furthermore, the misalignment between tag and anchor and antenna composition used yielded counterintuitive results. Instead of an improvement in performance, a degradation was noted as the number of antennas increased.

Regarding the fourth research question, two methods of antenna compensation were proposed to reduce the spread observed in the unwrapped arguments. These methods are termed as antenna deviation compensation and antenna deviation and mean compensation. The former computes the deviation to the mean argument of each antenna across all Bluetooth channels, while the latter extends upon the first method by also consider the mean argument. Both methods produce an antenna compensation matrix with dimensions corresponding to the number of antennas by number of channel indices.

After applying the first method, negligible improvements were found in the range -0.24° and 0.18° for the AVG, MUSIC, and ESPRIT algorithms. For the MVDR algorithm, the improvements were more substantial, although they were predominantly negative. The second method exhibited a larger range in improvements, but primarily highlighted the misalignment between the tag and anchor. This emphasizes the importance of a properly alignment between the tag and anchor. These results were obtained using all one thousand snapshots.

A final experiment was conducted to investigate the relationship between the improvements and the number of snapshots. Although the range increased by more than double, ranging between -0.58° and 0.53°, the improvements remained minor. As the number of snapshots decreased, the improvements increased, suggesting that the improvements are dependent on the snapshots count.

In conclusion, this thesis has explored the performance of a URA within the context of Bluetooth technology. It has identified eight unique configurations, with update rates based on the communication mode, and has conducted a comparative analysis of DoA estimation algorithms. Moreover, it has proposed methods to reduce argument spread between Bluetooth packets. The findings underscore the influence of several factors on the algorithms' performance and highlights the necessity for precise alignment in antenna setups.

8.1 Recommendations

The research conducted has not only provided insightful findings but also created opportunities for future explorations. The following aspects could be considered for further investigation:

- Impact of realistic indoor environments on the DoA estimation accuracy. IPSs, a primary application of Bluetooth localization, are subject to many sources of

imperfections such as multipath propagation, interference from other tags and devices, and non-ideal antenna characteristics. These factors can degrade the performance of DoA estimation algorithms and should be taken into account in future simulations and experiments.

- Comparison of DoA estimation algorithms. Numerous existing and emerging DoA estimation algorithms offer varying advantages and disadvantages in terms of computational complexity, robustness, and resolution. Evaluating the performance of these algorithms under the same conditions as those used in this thesis could provide valuable insight into identify the most effective algorithm for Bluetooth localization.
- Exploration of different antenna configurations and types for DoA estimation. This thesis primarily focused on a URA with an array configuration featuring an equal number of elements in each direction. However, other configurations such as UCA and L-shaped array may offer different computational complexities and performance levels for DoA estimation. Additionally, the type of antenna used can also influence the performance of DoA estimation and should be considered in future work.

Bibliography

[1] F. Dwiyasa and M.-H. Lim, “A survey of problems and approaches in wireless-based indoor positioning,” in *2016 International Conference on Indoor Positioning and Indoor Navigation (IPIN)*, 2016, pp. 1–7.

[2] M. Jason, “New Trends in Bluetooth Location Services Solutions,” 11 Apr. 2023. [Online]. Available: https://www.bluetooth.com/blog/new-trends-in-bluetooth-location-services-solutions/

[3] B. S. I. Group, “Direction Finding.” [Online]. Available: https://www.bluetooth.com/learn-about-bluetooth/feature-enhancements/direction-finding/

[4] M. Woolley, “Bluetooth Direction Finding a Technical Overview,” 13 Oct. 2021. [Online]. Available: https://www.bluetooth.com/blog/new-trends-in-bluetooth-location-services-solutions/

[5] ——, “Introducing: The Bluetooth Low Energy Primer,” 19 May 2022. [Online]. Available: https://www.bluetooth.com/blog/introducing-the-bluetooth-low-energy-primer/

[6] B. S. I. Group, “Bluetooth core specification v5.3,” 13 Jul. 2021. [Online]. Available: https://www.bluetooth.com/specifications/specs/core-specification-5-3/

[7] R. Natarajan, P. Zand, and M. Nabi, “Analysis of coexistence between ieee 802.15.4, ble and ieee 802.11 in the 2.4 ghz ism band,” in *IECON 2016 - 42nd Annual Conference of the IEEE Industrial Electronics Society*, 2016, pp. 6025–6032.

[8] M. Woolley, “Bluetooth Core Specification Version 5.1 feature overview,” 9 Dec. 2020. [Online]. Available: https://www.bluetooth.com/bluetooth-resources/bluetooth-core-specification-v5-1-feature-overview/

[9] C. A. Balanis, *Antenna Theory: Analysis and Design*. Wiley-Interscience, 2016.

[10] M. Zatman, “How narrow is narrowband? [adaptive array signal processing],” in *Conference Record of the Thirty-First Asilomar Conference on Signals, Systems and Computers (Cat. No.97CB36136)*, vol. 2, 1997, pp. 1341–1345 vol.2.

[11] G. B. Thomas, *Thomas’ calculus Early Transcendentals: Pearson New International Edition*. Pearson Education Limited, Jul. 2013.

[12] M. Viberg and H. Krim, “Two decades of statistical array processing,” in *Conference Record of the Thirty-First Asilomar Conference on Signals, Systems and Computers (Cat. No.97CB36136)*, vol. 1, 1997, pp. 775–777 vol.1.

[13] Y. Li, S.-L. Hu, J. Wang, and Z.-H. Huang, “An introduction to the computational complexity of matrix multiplication,” *Journal of the Operations Research Society of China*, vol. 8, 12 2019.

[14] E. S. Quintana, G. Quintana, X. Sun, and R. van de Geijn, “A note on parallel matrix inversion,” *SIAM Journal on Scientific Computing*, vol. 22, no. 5, pp. 1762–1771, 2001.

[15] M. Mrinal, “Galois theory and the abel-ruffini theorem,” 2019. [Online]. Available: https://api.semanticscholar.org/CorpusID:207980247

[16] J. Dongarra and F. Sullivan, “Guest editors introduction to the top 10 algorithms,” *Computing in Science & Engineering*, vol. 2, no. 01, pp. 22–23, jan 2000.

[17] P. Arbenz, “The QR Algorithm.” [Online]. Available: https://people.inf.ethz.ch/arbenz/ewp/Lnotes/chapter4.pdf

[18] J. Capon, “High-resolution frequency-wavenumber spectrum analysis,” *Proceedings of the IEEE*, vol. 57, no. 8, pp. 1408–1418, 1969.

[19] T. Kiong, B. S., J. Paw, I. D. P. Krishnan, and S. Darzi, “Minimum variance distortionless response beamformer with enhanced nulling level control via dynamic mutated artificial immune system,” *The Scientific World Journal*, vol. 2014, p. 164053, 06 2014.

[20] R. Schmidt, “Multiple emitter location and signal parameter estimation,” *IEEE Transactions on Antennas and Propagation*, vol. 34, no. 3, pp. 276–280, 1986.

[21] P. Gupta and S. Kar, “Music and improved music algorithm to estimate direction of arrival,” in *2015 International Conference on Communications and Signal Processing (ICCSP)*, 2015, pp. 0757–0761.

[22] S. Pillai and B. Kwon, “Performance analysis of music-type high resolution estimators for direction finding in correlated and coherent scenes,” *IEEE Transactions on Acoustics, Speech, and Signal Processing*, vol. 37, no. 8, pp. 1176–1189, 1989.

[23] M. G. Porozantzidou and M. T. Chryssomallis, “Azimuth and elevation angles estimation using 2-d music algorithm with an l-shape antenna,” in *2010 IEEE Antennas and Propagation Society International Symposium*, 2010, pp. 1–4.

[24] R. Roy and T. Kailath, “Esprit-estimation of signal parameters via rotational invariance techniques,” *IEEE Transactions on Acoustics, Speech, and Signal Processing*, vol. 37, no. 7, pp. 984–995, 1989.

[25] M. Haardt, M. Zoltowski, C. Mathews, and J. Nossek, “2d unitary esprit for efficient 2d parameter estimation,” in *1995 International Conference on Acoustics, Speech, and Signal Processing*, vol. 3, 1995, pp. 2096–2099 vol.3.

[26] “Python.” [Online]. Available: https://www.python.org/

[27] M. Jason, “3 Key Factors That Determine the Range of Bluetooth,” 17 Oct. 2019. [Online]. Available: https://www.bluetooth.com/blog/3-key-factors-that-determinethe-range-of-bluetooth/

[28] “Receiver sensitivity / noise.” [Online]. Available: http://www.tscm.com/rcvr_sen.pdf

[29] B. Park and K. Kwon, “2.4-ghz bluetooth low energy receiver employing new quadrature low-noise amplifier for low-power low-voltage iot applications,” *IEEE Transactions on Microwave Theory and Techniques*, vol. 69, no. 3, pp. 1887–1895, 2021.

[30] “Bluetooth Dual Polarized antenna array Radio Board - Silicon Labs.” [Online]. Available: https://www.silabs.com/development-tools/wireless/bluetooth/bg22-rb4191a-bg22-bluetooth-dual-polarized-antenna-array-radio-board

[31] “Series 2 Bluetooth Low Energy SOC - Silicon Labs.” [Online]. Available: https://www.silabs.com/wireless/bluetooth/efr32bg22-series-2-socs

[32] “bybgapi 1.2.0.” [Online]. Available: https://pypi.org/project/pybgapi/

[33] “Antenna Module ANT2 - CoreHW.” [Online]. Available: https://www.corehw.com/antenna-array-ant2/

[34] “Bluetooth Thunderboard Kit - Silicon Labs.” [Online]. Available: https://www.silabs.com/development-tools/thunderboard/thunderboard-bg22-kit

[35] “UG415: Thunderboard EFR32BG22 User’s Guide - Silicon Labs.” [Online]. Available: https://www.silabs.com/documents/public/user-guides/ug415-brd4184a-user-guide.pdf

[36] “pickle — Python object serialization.” [Online]. Available: https://docs.python.org/3/library/pickle.html

Appendix A

Alignment and Mounting Mechanism of Tag and Anchor

To establish the desired incident angle, it is essential to align the tag and anchor. The tag is mounted onto an adjustable pedestal, while the anchor is mounted onto a tube that can be inserted into the positioner.

An alignment mechanism, consisting of a transparent nylon thread and two disks, is used. Each disk is designed with a central hole of varying diameter. One hole matches the diameter of the thread, while the other is slightly larger. These disks can be secured to both sides of the positioner. The thread is passed through both disks and attached to the section of the pedestal where the tag will be mounted. When the thread aligns with the center of the disk, it indicates that the tag is aligned with the center of the anchor. This alignment process is sketched in Figure A.1, while Figure A.2 provides a view of the actual setup.

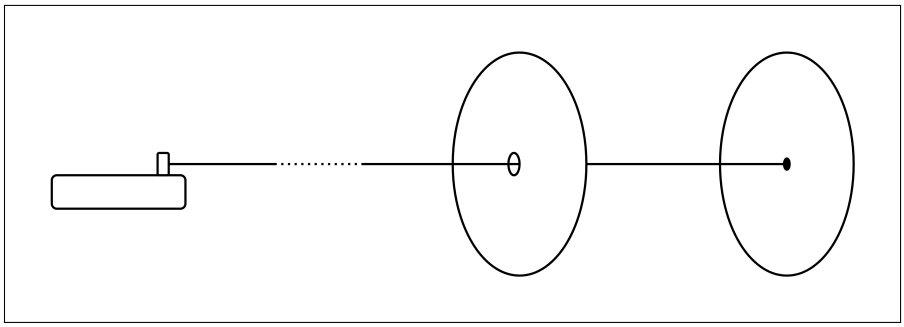

Figure A.1: Alignment mechanism of the tag and anchor using a nylon thread and two disks

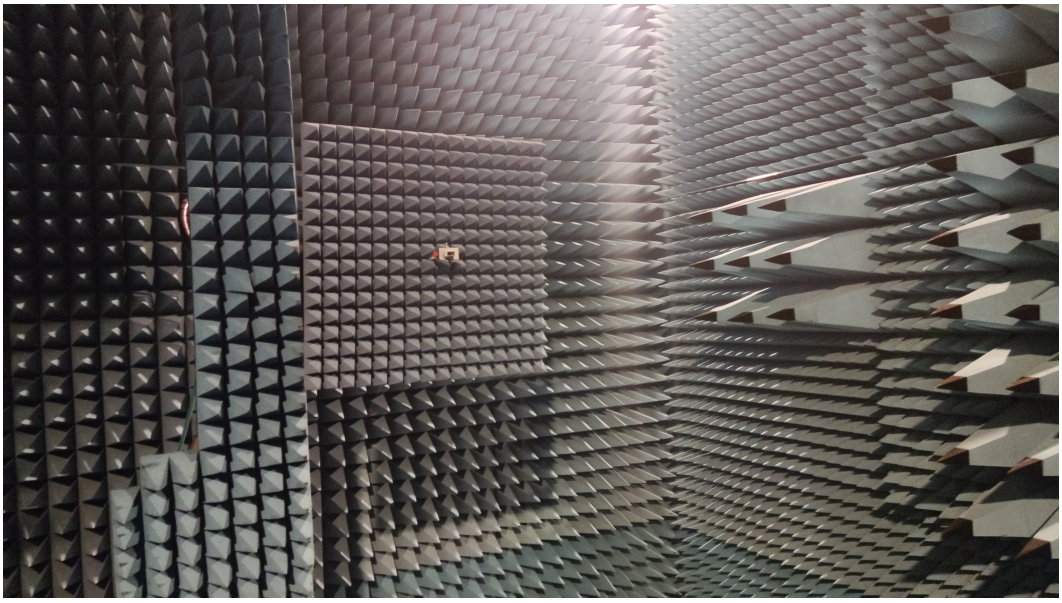

(a) Pedestal

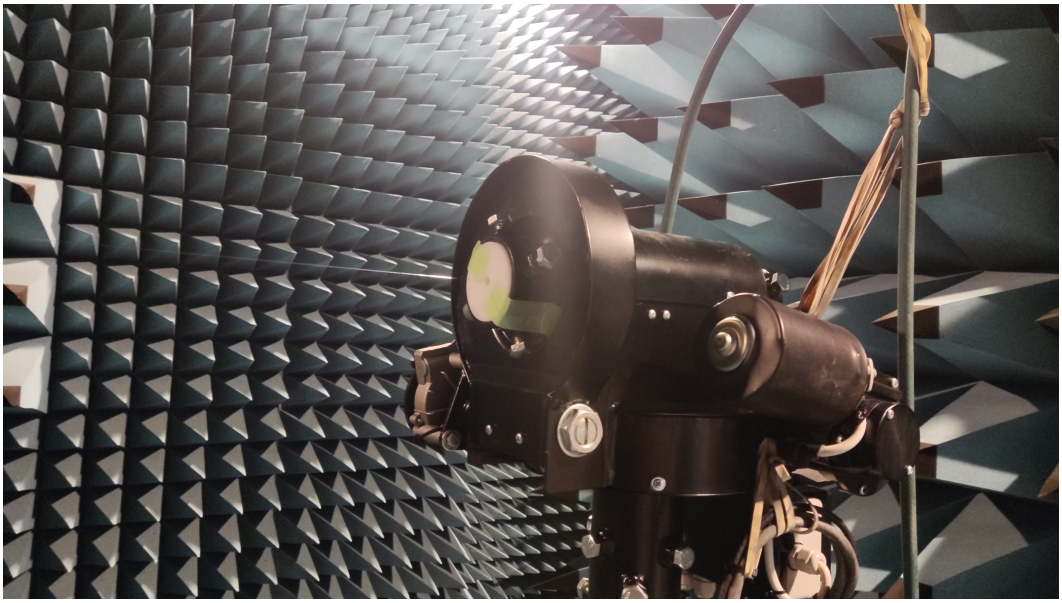

(b) Positioner

Figure A.2: Alignment process of tag and anchor

The anchor and debugger are secured to a backplane, as depicted in Figure A.3. This assembly is subsequently attached to the tube that is inserted into the positioner. A level is utilized to ensure that the polarization of the tag aligns with the horizontal port of the anchor.

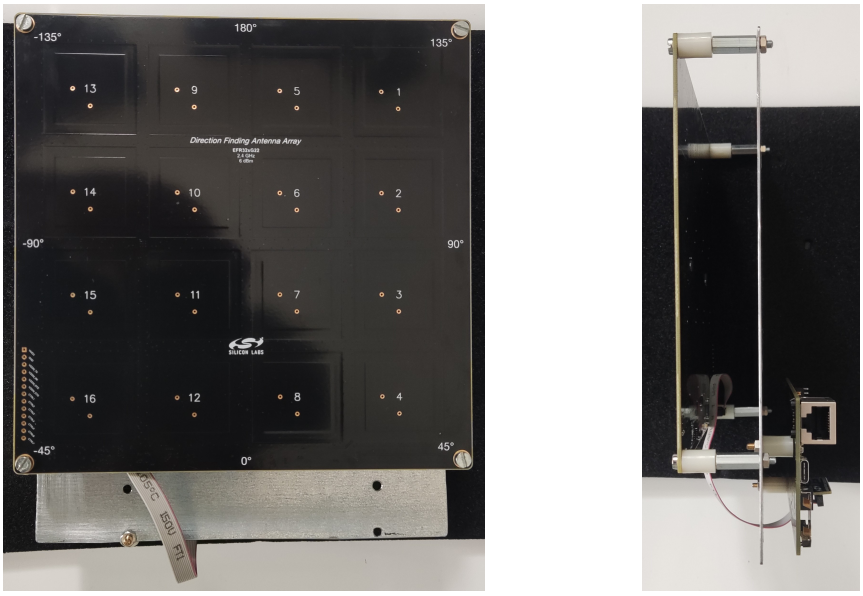

(a) Top view (b) Side view

Figure A.3: Assembly of the anchor and debugger to the backplane

Appendix B

Estimated Incident Angles

A detailed overview of the estimated incident angles obtained from all four DoA estimation algorithms are provided. For the antenna compensation measurements only the horizontal port is provided. The estimated incident angles can be found in Table B.1, Table B.2, and Table B.3, for the transmit powers 8.5, 2.0, and -8.5 dBm, respectively.

In case of the data measurements, both horizontal and vertical ports are used. Table B.4, Table B.5, and Table B.6 present the estimated incident angles for the horizontal polarization. The estimated incident angles for the vertical port are presented in Table B.7, Table B.8, and Table B.9. The transmit powers for the data measurements are consistent with those used for the antenna compensation measurements.

Table B.1: Estimated incident angles antenna compensation measurements (transmit power 8.5 dBm and horizontal port)

Reference Angles		AVG		MVDR		MUSIC		ESPRIT	
Az.	El.	Az.	El.	Az.	El.	Az.	El.	Az.	El.
±90	0	-65.08	2.65	-57.50	2.86	-71.29	2.39	-70.53	2.74
90	15	82.39	15.02	79.47	15.10	83.99	15.09	83.29	15.01
-90	15	-89.10	19.31	-90.02	19.79	-89.48	19.44	-88.64	19.53
90	30	84.68	34.83	83.64	34.81	84.89	34.41	84.94	34.45
-90	30	-91.48	38.70	-92.16	38.60	-91.64	38.62	-91.07	39.13
90	45	85.98	54.16	86.66	52.14	86.05	53.17	85.85	53.75
-90	45	-91.07	56.79	-93.91	54.58	-90.92	57.28	-90.79	58.31
90	60	86.83	62.10	87.42	69.32	87.22	68.59	87.07	70.44
-90	60	-93.51	63.02	-92.48	68.99	-93.23	72.55	-92.75	74.35
90	75	87.26	62.96	87.58	90.00	87.72	90.00	87.01	0.00
-90	75	-93.02	62.09	-92.29	90.00	-92.67	90.00	-91.82	0.00
90	85	85.73	57.03	88.40	90.00	86.58	90.00	85.21	0.00
-90	85	-93.87	59.17	-92.60	90.00	-93.28	90.00	-92.16	0.00

Table B.2: Estimated incident angles antenna compensation measurements (transmit power 2.0 dBm and horizontal port)

Reference Angles		AVG		MVDR		MUSIC		ESPRIT	
Az.	El.	Az.	El.	Az.	El.	Az.	El.	Az.	El.
±90	0	-65.09	2.66	-59.93	3.03	-71.30	2.40	-70.57	2.75
90	15	82.37	15.02	79.32	15.62	83.99	15.10	83.28	14.99
-90	15	-89.10	19.33	-89.64	19.97	-89.47	19.45	-88.63	19.54
90	30	84.66	34.76	83.55	34.12	84.87	34.35	84.93	34.38
-90	30	-91.46	38.74	-91.90	38.70	-91.61	38.65	-91.01	39.17
90	45	86.02	54.24	86.94	51.56	86.11	53.27	85.90	53.88
-90	45	-91.07	56.81	-93.99	54.74	-90.91	57.30	-90.77	58.32
90	60	86.86	62.14	87.04	68.70	87.25	68.63	87.10	70.48
-90	60	-93.55	62.95	-91.86	70.29	-93.25	72.57	-92.79	74.39
90	75	87.23	62.87	87.16	90.00	87.70	90.00	86.99	0.00
-90	75	-93.02	62.12	-92.11	90.00	-92.67	90.00	-91.80	0.00
90	85	85.72	57.06	88.36	90.00	86.56	90.00	85.22	0.00
-90	85	-93.90	59.26	-92.62	90.00	-93.30	90.00	-92.17	0.00

Table B.3: Estimated incident angles antenna compensation measurements (transmit power -8.5 dBm and horizontal port)

Reference Angles		AVG		MVDR		MUSIC		ESPRIT	
Az.	El.	Az.	El.	Az.	El.	Az.	El.	Az.	El.
±90	0	-64.84	2.69	-73.37	2.65	-71.08	2.43	-70.16	2.77
90	15	82.31	15.02	79.99	15.87	83.93	15.10	83.21	14.99
-90	15	-89.12	19.34	-90.08	19.81	-89.50	19.47	-88.66	19.56
90	30	84.71	34.78	83.85	34.58	84.92	34.36	84.99	34.39
-90	30	-91.48	38.70	-91.58	38.68	-91.62	38.61	-91.04	39.14
90	45	86.01	54.20	86.59	52.28	86.09	53.26	85.89	53.85
-90	45	-91.07	56.86	-93.66	55.10	-90.91	57.35	-90.77	58.35
90	60	86.88	62.21	87.24	69.20	87.26	68.56	87.12	70.37
-90	60	-93.53	62.90	-91.75	69.06	-93.23	72.56	-92.76	74.33
90	75	87.29	62.92	87.45	90.00	87.75	90.00	87.02	0.00
-90	75	-93.00	62.01	-92.70	90.00	-92.65	90.00	-91.80	0.00
90	85	85.64	55.89	87.83	90.00	86.57	90.00	85.21	0.00
-90	85	-93.96	59.12	-93.35	90.00	-93.35	90.00	-92.18	0.00

Table B.4: Estimated incident angles data measurements (transmit power 8.5 dBm and horizontal port)

Reference Angles		AVG		MVDR		MUSIC		ESPRIT	
Az.	El.	Az.	El.	Az.	El.	Az.	El.	Az.	El.
75	0	-65.39	2.78	-43.10	3.54	-70.60	2.58	-69.28	2.87
60	0	-62.74	2.82	-47.19	3.89	-66.99	2.65	-65.78	2.92
45	0	-65.87	2.96	-67.90	2.43	-70.94	2.79	-68.09	3.06
30	0	-71.44	3.09	-76.77	2.51	-80.92	2.82	-75.55	3.21
15	0	-94.80	2.99	-100.59	3.13	-110.55	3.01	-103.07	2.99
5	0	-123.58	2.59	-147.82	3.40	-117.27	2.47	-115.52	2.23
-5	0	-133.70	0.59	18.46	0.88	-176.10	0.53	-116.38	0.86
-15	0	-44.79	0.95	-46.10	1.95	-33.93	0.80	-52.77	1.23
-30	0	-44.84	2.03	-45.90	2.65	-43.80	1.91	-49.76	2.22
-45	0	-51.45	2.43	-40.90	2.55	-52.14	2.27	-56.53	2.56
-60	0	-58.56	2.52	-62.42	2.45	-60.60	2.34	-63.54	2.64
-75	0	-64.38	2.40	-76.08	2.60	-68.73	2.18	-69.34	2.48
75	15	64.28	15.95	63.60	16.44	65.75	15.91	64.93	15.79
60	15	47.78	16.77	46.97	16.72	49.35	16.72	48.10	16.57
45	15	32.52	17.42	31.95	16.28	34.66	17.29	32.59	17.09
30	15	19.07	17.89	19.40	16.75	21.50	16.95	17.21	16.55
15	15	-18.50	8.22	-68.36	6.95	-3.88	11.67	-11.95	12.00
5	15	-81.48	8.26	-81.42	5.05	-74.03	9.42	-69.55	8.63
-5	15	-57.03	7.53	-53.59	11.20	-53.13	9.98	-60.96	7.90
-15	15	-27.24	16.18	-30.32	16.42	-33.59	15.27	-32.16	12.11
-30	15	-35.68	18.92	-29.40	20.44	-38.08	18.05	-36.85	16.15
-45	15	-48.31	19.54	-43.60	20.71	-49.74	19.13	-49.27	18.17
-60	15	-61.21	19.68	-59.14	19.34	-62.22	19.44	-62.15	19.04
-75	15	-75.13	19.31	-74.90	19.43	-76.10	19.27	-75.64	19.25
75	30	68.32	33.61	69.14	33.16	68.75	33.57	68.57	33.22
60	30	50.69	32.61	54.28	32.84	52.08	32.81	50.85	32.15
45	30	34.38	33.39	40.18	30.92	36.66	33.38	34.42	32.88
30	30	19.52	34.75	26.15	32.87	21.91	33.54	17.46	32.77
15	30	-10.44	24.37	-69.50	12.10	0.57	30.62	-11.76	29.88
5	30	-55.49	12.15	-87.12	13.61	-44.45	28.75	-47.07	24.94
-5	30	19.16	10.21	-26.45	56.88	-45.49	22.66	39.88	12.96
-15	30	-22.56	30.65	-27.14	48.89	-24.27	34.17	-9.81	24.13

Continuation of Table B.4

Reference Angles		AVG		MVDR		MUSIC		ESPRIT	
Az.	El.	Az.	El.	Az.	El.	Az.	El.	Az.	El.
-30	30	-33.05	37.26	-39.70	40.41	-35.95	36.23	-33.90	31.40
-45	30	-46.23	36.95	-52.81	40.08	-48.50	36.57	-47.70	33.84
-60	30	-62.21	36.90	-64.95	37.91	-63.19	36.85	-63.09	35.80
-75	30	-77.72	38.04	-78.70	38.65	-78.11	37.86	-77.82	38.03
75	45	71.41	53.84	71.93	53.15	71.40	53.04	71.34	53.58
60	45	55.69	53.77	57.94	54.14	55.99	53.20	55.65	53.57
45	45	40.99	55.73	44.65	57.05	41.82	54.75	40.93	55.34
30	45	27.12	55.79	28.49	50.68	27.46	56.34	26.57	56.06
15	45	4.25	29.46	139.16	69.73	6.11	60.99	-4.91	53.06
5	45	-78.06	10.11	143.35	90.00	-38.15	90.00	-64.80	34.84
-5	45	4.29	3.90	-7.74	56.03	0.43	58.53	18.15	37.71
-15	45	-20.88	39.52	-20.97	54.68	-17.66	57.40	-15.37	48.71
-30	45	-35.59	54.40	-38.40	52.29	-36.39	56.14	-35.77	51.75
-45	45	-48.45	55.49	-51.16	55.45	-48.90	55.91	-48.60	53.22
-60	45	-63.40	55.32	-64.61	53.20	-63.40	55.39	-63.77	54.59
-75	45	-78.31	55.90	-79.76	56.13	-78.33	56.76	-78.51	57.62
75	60	70.53	67.52	71.51	69.12	71.12	70.08	71.61	73.26
60	60	54.31	73.81	55.01	71.51	54.40	72.75	54.79	73.81
45	60	40.02	75.81	42.45	75.16	40.80	76.53	39.31	75.26
30	60	28.95	69.28	27.83	71.55	28.24	76.84	26.99	77.35
15	60	-1.70	38.38	1.03	61.83	-4.05	90.00	-12.24	0.00
5	60	-11.69	17.70	-68.07	36.84	-26.01	90.00	-14.25	55.08
-5	60	23.99	24.62	-129.30	22.77	12.27	69.84	14.72	49.81
-15	60	-23.25	41.52	-19.62	76.35	-14.16	72.35	-21.32	61.67
-30	60	-36.55	65.42	-35.28	68.20	-36.28	69.76	-36.02	67.76
-45	60	-47.80	73.29	-48.19	71.45	-48.68	73.19	-48.24	70.84
-60	60	-63.30	74.52	-63.26	72.12	-63.04	74.86	-63.79	75.03
-75	60	-78.21	63.73	-80.00	69.20	-78.79	74.85	-79.11	78.83
75	75	71.41	53.84	71.93	53.15	71.40	53.04	71.34	53.58
60	75	52.75	0.00	54.69	90.00	53.82	90.00	53.11	0.00
45	75	38.01	0.00	42.95	90.00	40.49	90.00	37.08	0.00
30	75	25.46	58.06	115.58	9.93	24.57	90.00	16.65	75.12
15	75	-4.21	34.66	135.99	55.63	-4.86	90.00	-11.76	75.87
5	75	31.77	11.15	133.45	69.86	52.13	90.00	39.48	54.47
-5	75	0.30	22.41	-86.20	4.82	11.86	90.00	0.67	41.28

Continuation of Table B.4

Reference Angles		AVG		MVDR		MUSIC		ESPRIT	
Az.	El.	Az.	El.	Az.	El.	Az.	El.	Az.	El.
-15	75	-24.82	43.20	-24.48	73.82	-18.67	68.86	-25.08	59.10
-30	75	-38.06	73.96	-41.25	78.66	-36.49	90.00	-37.07	80.58
-45	75	-47.45	0.00	-49.41	90.00	-48.10	90.00	-47.97	0.00
-60	75	-60.87	0.00	-61.28	90.00	-61.96	90.00	-62.38	0.00
-75	75	-76.38	64.82	-78.61	90.00	-78.17	90.00	-78.22	0.00
75	85	67.15	77.32	71.39	90.00	69.56	90.00	69.63	0.00
60	85	52.97	0.00	54.61	90.00	53.50	90.00	53.05	0.00
45	85	38.24	0.00	133.52	7.22	39.59	90.00	37.22	0.00
30	85	20.87	39.91	106.57	5.38	22.22	90.00	19.83	62.45
15	85	-13.53	19.81	143.40	63.91	-20.27	90.00	-29.17	73.92
5	85	-38.85	24.33	132.75	58.74	-47.16	90.00	-41.76	70.76
-5	85	27.60	40.24	-55.70	17.33	52.97	90.00	40.61	64.48
-15	85	-21.24	43.24	-23.98	90.00	-16.82	90.00	-18.63	54.85
-30	85	-38.49	0.00	-37.03	90.00	-36.97	90.00	-38.79	0.00
-45	85	-47.03	0.00	-49.09	90.00	-47.05	90.00	-47.33	0.00
-60	85	-57.21	0.00	-63.24	90.00	-60.39	90.00	-60.63	0.00
-75	85	-74.62	62.17	-81.28	90.00	-77.77	90.00	-77.24	0.00

End of Table B.4

Table B.5: Estimated incident angles data measurements (transmit power 2.0 dBm and horizontal port)

Reference Angles		AVG		MVDR		MUSIC		ESPRIT	
Az.	El.	Az.	El.	Az.	El.	Az.	El.	Az.	El.
75	0	-66.09	2.78	-53.40	3.12	-71.40	2.57	-70.02	2.87
60	0	-63.36	2.82	-50.97	3.80	-67.85	2.65	-66.44	2.92
45	0	-65.81	2.95	-60.90	2.66	-70.97	2.77	-68.11	3.05
30	0	-70.32	3.06	-78.48	2.52	-80.10	2.80	-74.88	3.18
15	0	-95.45	3.09	-105.69	3.76	-111.12	3.08	-103.86	3.05
5	0	-122.86	2.58	-146.96	3.31	-117.24	2.47	-115.85	2.25
-5	0	-138.36	0.59	4.80	1.01	177.90	0.54	-118.72	0.80
-15	0	-43.17	1.03	-36.90	1.80	-33.95	0.88	-52.95	1.30
-30	0	-44.28	2.06	-42.10	2.45	-42.86	1.94	-49.37	2.26

Continuation of Table B.5

Reference Angles		AVG		MVDR		MUSIC		ESPRIT	
Az.	El.	Az.	El.	Az.	El.	Az.	El.	Az.	El.
-45	0	-51.86	2.43	-35.90	2.74	-52.70	2.28	-56.89	2.56
-60	0	-57.75	2.56	-61.31	2.60	-59.64	2.37	-62.74	2.67
-75	0	-63.71	2.42	-80.26	2.72	-67.91	2.21	-68.59	2.50
75	15	64.40	15.91	61.78	16.13	65.88	15.87	65.02	15.76
60	15	47.87	16.78	47.24	16.23	49.44	16.73	48.19	16.56
45	15	32.51	17.41	30.91	16.56	34.67	17.28	32.59	17.07
30	15	19.06	17.88	17.79	16.75	21.51	16.94	17.20	16.54
15	15	-17.50	8.30	-41.11	7.17	-3.71	11.68	-11.85	12.01
5	15	-81.44	8.32	-78.54	5.22	-73.99	9.46	-70.05	8.73
-5	15	-56.23	7.81	-68.66	9.82	-52.38	10.16	-59.88	8.00
-15	15	-27.30	16.15	-29.02	16.42	-33.71	15.25	-32.27	12.09
-30	15	-35.72	18.90	-31.70	18.58	-38.12	17.99	-36.82	16.01
-45	15	-48.32	19.55	-44.33	18.55	-49.72	19.14	-49.21	18.11
-60	15	-61.25	19.70	-59.49	18.96	-62.26	19.45	-62.11	19.02
-75	15	-75.11	19.32	-75.52	19.58	-76.07	19.28	-75.60	19.26
75	30	68.26	33.52	68.32	33.03	68.71	33.49	68.53	33.11
60	30	50.79	32.64	53.18	32.97	52.15	32.83	50.95	32.18
45	30	34.42	33.38	39.36	30.91	36.68	33.38	34.48	32.90
30	30	19.57	34.67	23.99	32.30	21.91	33.49	17.63	32.73
15	30	-10.47	24.44	-35.90	12.23	0.47	30.57	-11.98	29.86
5	30	-55.01	12.23	-89.69	14.19	-44.58	28.59	-47.36	24.53
-5	30	18.85	10.17	-25.76	56.18	-46.66	22.18	40.83	12.73
-15	30	-22.73	30.35	-29.88	47.13	-24.55	34.25	-10.35	24.07
-30	30	-33.02	37.26	-39.63	39.70	-35.92	36.19	-33.86	31.30
-45	30	-46.27	36.96	-53.99	38.77	-48.56	36.44	-47.81	33.38
-60	30	-62.21	36.92	-66.57	37.52	-63.21	36.77	-63.19	35.65
-75	30	-77.79	38.07	-78.89	37.32	-78.13	37.89	-77.82	38.15
75	45	71.39	53.80	71.91	52.42	71.38	53.03	71.32	53.56
60	45	55.82	53.84	57.98	54.88	56.09	53.26	55.78	53.63
45	45	40.94	55.72	44.85	57.10	41.79	54.73	40.89	55.32
30	45	27.06	55.65	28.69	49.79	27.40	56.21	26.49	55.95
15	45	5.14	29.56	141.54	63.11	6.32	61.03	-4.85	53.22
5	45	-76.48	10.05	141.55	79.43	-37.99	90.00	-63.15	34.54
-5	45	9.73	3.11	-8.38	59.59	0.83	58.32	20.41	35.79
-15	45	-20.73	39.30	-19.31	55.68	-17.60	57.44	-15.29	48.64

Continuation of Table B.5

Reference Angles		AVG		MVDR		MUSIC		ESPRIT	
Az.	El.	Az.	El.	Az.	El.	Az.	El.	Az.	El.
-30	45	-35.54	54.49	-38.25	52.53	-36.40	56.26	-35.76	51.78
-45	45	-48.43	55.48	-51.01	54.31	-48.87	55.85	-48.59	53.08
-60	45	-63.38	55.29	-64.60	54.61	-63.36	55.33	-63.72	54.53
-75	45	-78.35	55.99	-79.42	55.45	-78.32	56.82	-78.48	57.71
75	60	70.52	67.49	71.33	69.42	71.13	70.08	71.61	73.27
60	60	54.31	73.81	54.53	71.28	54.39	72.74	54.78	73.78
45	60	40.03	75.71	42.47	76.11	40.79	76.47	39.29	75.20
30	60	29.00	69.67	28.54	70.25	28.37	76.93	27.12	77.35
15	60	-1.88	38.49	-0.25	71.61	-4.21	90.00	-12.26	0.00
5	60	-10.97	17.68	139.76	73.28	-26.21	90.00	-13.83	54.27
-5	60	22.59	25.05	-14.29	90.00	11.90	70.01	13.35	50.74
-15	60	-23.16	41.62	-20.23	77.11	-14.12	72.31	-21.30	61.77
-30	60	-36.63	65.61	-35.22	69.28	-36.37	69.95	-36.16	67.96
-45	60	-47.80	73.23	-48.34	71.01	-48.69	73.14	-48.24	70.79
-60	60	-63.33	74.47	-63.27	72.09	-63.08	74.88	-63.83	75.05
-75	60	-78.19	63.73	-78.58	70.47	-78.74	74.83	-79.06	78.79
75	75	71.39	53.80	71.91	52.42	71.38	53.03	71.32	53.56
60	75	52.79	0.00	54.36	90.00	53.86	90.00	53.18	0.00
45	75	37.81	0.00	42.56	90.00	40.33	90.00	36.83	0.00
30	75	25.51	58.09	121.43	11.04	24.62	90.00	16.71	75.03
15	75	-4.66	34.56	138.19	58.97	-4.99	90.00	-11.29	76.78
5	75	32.86	10.96	133.79	71.81	51.76	90.00	36.91	53.47
-5	75	0.52	22.38	-133.15	78.29	11.88	90.00	0.92	41.54
-15	75	-24.78	43.16	-23.79	71.88	-18.66	68.98	-25.12	59.17
-30	75	-37.98	74.08	-40.30	81.31	-36.41	90.00	-36.98	80.60
-45	75	-47.45	0.00	-49.75	90.00	-48.09	90.00	-47.94	0.00
-60	75	-60.89	0.00	-61.68	90.00	-61.97	90.00	-62.39	0.00
-75	75	-76.41	64.61	-78.20	90.00	-78.21	90.00	-78.26	0.00
75	85	67.13	76.99	71.12	90.00	69.58	90.00	69.62	0.00
60	85	53.06	0.00	55.16	90.00	53.58	90.00	53.14	0.00
45	85	38.29	0.00	134.43	7.07	39.64	90.00	37.25	0.00
30	85	20.86	39.28	108.68	5.26	22.34	90.00	20.15	62.08
15	85	-14.94	19.89	143.68	58.48	-20.26	90.00	-29.42	74.93
5	85	-37.52	23.93	133.57	59.87	-47.42	90.00	-42.56	72.07
-5	85	27.85	40.22	-24.18	33.52	53.14	90.00	40.98	64.97

Continuation of Table B.5

Reference Angles		AVG		MVDR		MUSIC		ESPRIT	
Az.	El.	Az.	El.	Az.	El.	Az.	El.	Az.	El.
-15	85	-21.17	43.33	-24.78	79.53	-16.65	90.00	-18.93	55.74
-30	85	-38.43	0.00	-36.71	90.00	-36.97	90.00	-38.78	0.00
-45	85	-47.03	0.00	-48.79	90.00	-47.05	90.00	-47.33	0.00
-60	85	-57.18	0.00	-63.14	90.00	-60.37	90.00	-60.60	0.00
-75	85	-74.49	62.03	-80.68	90.00	-77.71	90.00	-77.16	0.00

End of Table B.5

Table B.6: Estimated incident angles data measurements (transmit power -8.5 dBm and horizontal port)

Reference Angles		AVG		MVDR		MUSIC		ESPRIT	
Az.	El.	Az.	El.	Az.	El.	Az.	El.	Az.	El.
75	0	-65.04	2.78	-47.90	3.32	-70.25	2.58	-68.88	2.86
60	0	-62.69	2.83	-49.20	3.91	-66.97	2.65	-65.88	2.93
45	0	-65.56	2.96	-65.10	2.68	-70.66	2.79	-67.96	3.06
30	0	-70.52	3.06	-76.02	2.52	-80.23	2.80	-74.93	3.19
15	0	-95.12	3.02	-109.28	3.38	-110.77	3.03	-103.15	3.02
5	0	-123.40	2.56	-130.10	3.67	-116.79	2.44	-114.74	2.20
-5	0	-137.98	0.61	-15.70	1.16	-178.10	0.56	-118.85	0.86
-15	0	-43.86	0.97	-33.32	1.80	-34.38	0.83	-52.94	1.27
-30	0	-44.43	2.08	-40.90	2.57	-43.13	1.97	-49.52	2.28
-45	0	-51.47	2.47	-34.03	2.42	-52.15	2.30	-56.62	2.60
-60	0	-58.01	2.55	-53.02	2.37	-60.01	2.37	-63.06	2.67
-75	0	-64.03	2.44	-77.31	2.31	-68.05	2.21	-68.81	2.52
75	15	64.45	15.92	62.19	16.39	65.96	15.87	65.09	15.76
60	15	47.78	16.77	45.74	16.57	49.29	16.73	48.06	16.55
45	15	32.54	17.42	31.79	17.06	34.72	17.29	32.60	17.08
30	15	19.03	17.93	18.20	16.86	21.51	16.98	17.09	16.58
15	15	-13.83	8.44	-20.93	9.54	-3.61	11.67	-11.72	11.99
5	15	-81.33	8.27	-88.81	7.31	-74.06	9.43	-70.21	8.71
-5	15	-58.03	7.63	-79.23	11.19	-53.58	10.14	-60.94	8.07
-15	15	-27.10	16.28	-30.78	19.40	-33.08	15.46	-31.93	12.27
-30	15	-35.82	18.88	-33.72	18.09	-38.15	17.96	-37.03	16.00

Continuation of Table B.6

Reference Angles		AVG		MVDR		MUSIC		ESPRIT	
Az.	El.	Az.	El.	Az.	El.	Az.	El.	Az.	El.
-45	15	-48.26	19.56	-45.20	19.19	-49.64	19.14	-49.18	18.11
-60	15	-61.16	19.70	-60.12	19.51	-62.18	19.45	-62.08	19.04
-75	15	-75.07	19.31	-75.34	19.59	-76.05	19.26	-75.63	19.25
75	30	68.27	33.59	69.18	33.36	68.69	33.54	68.53	33.16
60	30	50.81	32.62	53.69	33.01	52.18	32.83	50.97	32.15
45	30	34.36	33.44	38.69	31.06	36.63	33.43	34.37	32.92
30	30	19.54	34.66	22.56	32.13	21.87	33.49	17.57	32.72
15	30	-10.23	24.46	1.31	24.71	0.66	30.60	-11.68	29.83
5	30	-54.56	11.67	-89.62	13.29	-44.93	28.24	-47.24	24.38
-5	30	16.42	9.15	-2.29	40.03	-45.82	22.76	38.44	12.35
-15	30	-19.97	29.31	-22.31	44.65	-23.26	34.14	-8.11	24.78
-30	30	-33.12	37.23	-37.58	40.46	-36.00	36.14	-33.85	31.29
-45	30	-46.30	36.94	-53.00	38.92	-48.60	36.42	-47.84	33.35
-60	30	-62.20	36.94	-66.26	37.47	-63.22	36.78	-63.21	35.64
-75	30	-77.76	38.03	-78.97	37.91	-78.11	37.84	-77.81	38.08
75	45	71.38	53.79	71.68	52.97	71.38	53.03	71.32	53.55
60	45	55.70	53.80	57.75	53.65	55.99	53.23	55.66	53.59
45	45	40.89	55.72	44.49	56.79	41.74	54.71	40.84	55.31
30	45	27.18	55.83	26.93	53.05	27.44	56.34	26.52	56.08
15	45	4.51	27.93	59.76	18.68	4.36	61.08	-7.94	55.97
5	45	-70.93	9.05	135.22	90.00	-39.11	90.00	-59.16	39.04
-5	45	8.17	4.44	1.81	62.76	0.44	58.48	17.92	38.27
-15	45	-20.79	39.40	-7.75	59.22	-17.72	57.28	-15.51	48.95
-30	45	-35.46	54.22	-35.87	54.49	-36.34	56.04	-35.67	51.72
-45	45	-48.44	55.53	-50.57	55.14	-48.90	55.93	-48.61	53.13
-60	45	-63.36	55.27	-64.08	55.05	-63.33	55.29	-63.69	54.51
-75	45	-78.35	55.96	-79.31	55.82	-78.30	56.80	-78.46	57.70
75	60	70.50	67.45	71.42	69.88	71.11	70.03	71.59	73.20
60	60	54.31	73.97	53.93	72.81	54.38	72.87	54.78	73.89
45	60	40.03	75.52	43.00	78.59	40.79	76.28	39.29	75.01
30	60	29.09	69.16	27.46	72.85	28.33	77.07	27.09	77.56
15	60	-2.01	37.36	-13.34	70.99	-4.46	90.00	-12.51	0.00
5	60	-9.32	18.16	141.75	70.55	-26.40	90.00	-14.23	56.45
-5	60	24.04	25.78	-26.12	69.19	13.02	71.12	15.48	50.78
-15	60	-22.98	41.56	-19.06	72.94	-14.12	72.17	-21.16	61.70

Continuation of Table B.6

Reference Angles		AVG		MVDR		MUSIC		ESPRIT	
Az.	El.	Az.	El.	Az.	El.	Az.	El.	Az.	El.
-30	60	-36.62	65.62	-34.40	68.72	-36.37	69.99	-36.15	67.99
-45	60	-47.77	73.11	-48.70	72.12	-48.67	73.05	-48.23	70.71
-60	60	-63.30	74.42	-63.55	73.92	-63.06	74.93	-63.80	75.10
-75	60	-78.19	63.67	-78.68	70.21	-78.74	74.77	-79.06	78.70
75	75	71.38	53.79	71.68	52.97	71.38	53.03	71.32	53.55
60	75	52.67	0.00	53.88	90.00	53.73	90.00	53.04	0.00
45	75	37.91	0.00	41.04	90.00	40.30	90.00	36.80	0.00
30	75	25.65	58.64	22.26	90.00	24.66	90.00	16.75	75.01
15	75	-4.80	34.13	141.23	61.22	-4.98	90.00	-11.27	80.59
5	75	26.92	9.98	128.81	78.11	51.60	90.00	43.73	55.47
-5	75	1.09	22.60	16.77	80.00	12.10	90.00	2.88	43.36
-15	75	-24.64	42.89	-26.07	63.92	-18.53	68.89	-24.95	59.16
-30	75	-38.01	74.06	-39.30	76.94	-36.42	90.00	-36.96	80.94
-45	75	-47.47	0.00	-48.02	90.00	-48.14	90.00	-48.00	0.00
-60	75	-60.82	0.00	-61.94	90.00	-61.94	90.00	-62.36	0.00
-75	75	-76.41	64.62	-78.08	90.00	-78.22	90.00	-78.26	0.00
75	85	67.09	76.76	69.97	90.00	69.55	90.00	69.62	0.00
60	85	52.89	0.00	54.47	90.00	53.51	90.00	53.06	0.00
45	85	38.28	0.00	39.50	90.00	39.62	90.00	37.23	0.00
30	85	21.31	39.15	93.62	5.14	22.17	90.00	19.75	62.47
15	85	-18.74	20.35	151.04	59.22	-21.25	90.00	-29.70	78.44
5	85	-32.51	23.44	134.09	55.22	-49.24	90.00	-45.44	0.00
-5	85	28.73	39.27	-16.81	48.19	54.44	90.00	41.62	63.70
-15	85	-20.33	42.28	-25.36	67.75	-16.44	90.00	-18.42	55.52
-30	85	-38.48	0.00	-34.89	90.00	-36.95	90.00	-38.79	0.00
-45	85	-47.04	0.00	-47.92	90.00	-47.09	90.00	-47.38	0.00
-60	85	-57.21	0.00	-62.16	90.00	-60.45	90.00	-60.69	0.00
-75	85	-74.50	61.87	-80.91	90.00	-77.71	90.00	-77.19	0.00

End of Table B.6

Table B.7: Estimated incident angles data measurements (transmit power 8.5 dBm and vertical port)

Reference Angles		AVG		MVDR		MUSIC		ESPRIT	
Az.	El.	Az.	El.	Az.	El.	Az.	El.	Az.	El.
75	0	90.68	3.30	92.00	2.87	88.08	3.61	93.84	3.22
60	0	56.24	1.18	-89.90	-0.33	49.25	1.70	50.80	1.85
45	0	11.55	0.98	-100.62	1.24	16.58	1.29	23.12	1.33
30	0	-5.99	1.25	-51.90	1.02	-0.96	1.45	3.20	1.52
15	0	-11.28	1.52	-22.10	1.32	-6.57	1.72	-4.38	1.84
5	0	-13.72	1.68	-19.90	1.69	-9.45	1.90	-7.41	2.07
-5	0	-24.23	2.09	-30.90	2.70	-21.76	2.29	-21.06	2.45
-15	0	-28.87	2.20	-24.90	2.63	-27.18	2.41	-25.53	2.57
-30	0	-34.37	2.34	-20.99	3.00	-33.42	2.57	-30.60	2.75
-45	0	-37.05	2.44	-36.10	3.73	-38.27	2.69	-36.26	2.89
-60	0	-36.88	2.68	-30.76	3.72	-42.69	3.04	-42.50	3.15
-75	0	-43.33	3.04	-43.64	3.01	-51.36	3.24	-61.81	2.72
75	15	80.67	18.49	70.56	15.57	79.84	17.41	98.27	17.02
60	15	59.78	17.90	52.46	17.09	56.97	18.31	62.61	17.65
45	15	41.33	17.99	37.70	17.74	39.03	18.71	41.95	18.04
30	15	24.15	18.38	19.33	20.10	22.93	19.15	24.47	18.23
15	15	7.96	19.06	2.80	21.52	7.55	19.76	7.90	18.70
5	15	-2.65	19.80	-7.19	21.47	-2.58	20.43	-2.82	19.30
-5	15	-14.21	20.54	-13.40	21.29	-13.40	20.90	-14.20	19.47
-15	15	-23.16	20.70	-21.74	22.36	-22.07	20.91	-23.25	19.39
-30	15	-35.62	20.29	-32.89	21.78	-34.23	20.42	-35.90	18.90
-45	15	-48.06	19.34	-44.34	21.33	-46.37	19.71	-48.46	18.53
-60	15	-59.95	17.47	-56.47	19.51	-57.68	18.15	-59.36	17.24
-75	15	-69.19	13.58	-70.62	16.13	-66.26	15.17	-67.36	13.89
75	30	86.45	30.85	69.67	36.28	86.80	33.09	95.51	31.68
60	30	62.69	34.99	53.02	35.08	60.42	33.92	62.79	33.40
45	30	46.05	34.59	39.60	34.58	43.77	34.58	45.58	33.66
30	30	28.85	34.48	22.04	35.94	27.38	35.09	28.53	33.84
15	30	11.51	35.76	8.43	37.34	10.91	36.41	10.93	35.41
5	30	1.34	36.21	0.65	39.27	1.02	36.88	0.31	36.14
-5	30	-10.56	36.29	-8.16	37.95	-10.21	37.07	-11.27	36.13
-15	30	-21.98	35.83	-17.86	39.16	-21.15	36.53	-22.58	35.33

Continuation of Table B.7

Reference Angles		AVG		MVDR		MUSIC		ESPRIT	
Az.	El.	Az.	El.	Az.	El.	Az.	El.	Az.	El.
-30	30	-38.42	36.55	-36.47	36.71	-37.38	36.84	-39.45	34.82
-45	30	-51.84	37.81	-48.25	37.49	-50.49	37.27	-51.96	34.92
-60	30	-63.03	35.85	-57.46	37.70	-63.45	33.77	-61.69	31.34
-75	30	-82.35	23.36	-73.24	31.91	-79.86	25.98	-76.56	20.33
75	45	74.77	33.68	74.74	50.96	78.83	50.97	74.61	43.44
60	45	56.21	50.83	56.55	48.77	56.96	53.35	55.27	52.48
45	45	44.32	52.32	40.90	50.22	43.39	53.09	43.87	52.22
30	45	28.61	51.02	25.90	49.06	28.11	52.04	28.50	50.80
15	45	10.31	53.38	9.39	52.44	10.60	53.78	10.40	53.35
5	45	0.49	54.75	0.40	54.77	0.76	54.81	0.75	54.71
-5	45	-8.13	54.39	-9.09	55.81	-8.06	54.64	-7.90	54.38
-15	45	-18.48	52.21	-18.17	54.42	-18.01	52.82	-18.20	51.88
-30	45	-36.44	51.25	-35.53	53.25	-35.19	51.42	-36.62	50.05
-45	45	-49.76	54.84	-47.92	56.44	-48.89	53.82	-50.05	52.79
-60	45	-56.81	46.55	-59.45	51.36	-61.99	53.38	-61.49	51.20
-75	45	-84.07	33.78	-74.80	40.26	-83.30	43.89	-87.75	36.44
75	60	70.42	33.61	72.11	49.85	76.34	62.85	71.77	56.59
60	60	55.13	61.87	51.66	59.09	54.46	63.98	51.19	61.28
45	60	42.97	67.20	40.54	64.28	42.16	67.23	41.86	66.44
30	60	28.34	66.61	27.81	65.73	27.56	67.29	28.30	66.28
15	60	9.85	67.92	10.34	70.16	9.74	70.37	9.68	69.87
5	60	0.20	68.24	1.32	73.62	0.15	72.92	0.27	72.96
-5	60	-8.85	69.00	-8.16	72.34	-8.85	72.13	-8.18	71.35
-15	60	-19.43	69.68	-18.65	72.25	-19.64	70.32	-19.08	69.03
-30	60	-36.00	69.10	-35.11	70.16	-35.69	70.35	-35.63	68.99
-45	60	-47.95	70.03	-47.40	67.56	-47.68	71.40	-47.65	69.50
-60	60	-58.42	60.34	-59.88	67.23	-59.42	71.17	-59.52	66.98
-75	60	-58.51	21.38	-80.59	70.86	-82.80	69.40	-86.23	48.11
75	75	72.90	43.67	-151.46	56.57	76.43	77.20	75.43	64.81
60	75	54.13	56.78	53.13	66.15	56.68	76.00	54.18	73.53
45	75	44.09	75.26	36.88	84.47	46.20	90.00	45.73	0.00
30	75	31.54	0.00	26.44	90.00	29.76	90.00	29.02	0.00
15	75	14.84	68.77	13.51	90.00	13.49	90.00	12.80	0.00
5	75	3.61	62.86	3.38	90.00	3.21	90.00	3.18	0.00
-5	75	-7.71	66.43	-7.10	90.00	-6.99	90.00	-6.80	0.00

Continuation of Table B.7

Reference Angles		AVG		MVDR		MUSIC		ESPRIT	
Az.	El.	Az.	El.	Az.	El.	Az.	El.	Az.	El.
-15	75	-17.59	86.59	-16.79	90.00	-17.31	90.00	-16.98	0.00
-30	75	-35.87	0.00	-35.31	90.00	-34.97	90.00	-35.31	0.00
-45	75	-49.82	0.00	-47.42	90.00	-49.09	90.00	-49.91	0.00
-60	75	-59.86	68.73	-58.36	90.00	-60.93	84.77	-59.64	76.56
-75	75	-78.81	24.26	140.61	67.07	-84.81	90.00	-84.23	68.46
75	85	54.59	71.63	56.07	90.00	55.69	90.00	55.55	0.00
60	85	44.96	0.00	43.13	90.00	45.18	90.00	45.86	0.00
45	85	74.87	40.82	-155.33	56.86	74.99	90.00	76.35	75.19
30	85	33.42	0.00	150.74	50.61	30.23	90.00	28.73	0.00
15	85	16.77	62.88	12.22	90.00	14.63	90.00	13.22	0.00
5	85	3.93	59.40	2.44	90.00	3.28	90.00	2.20	0.00
-5	85	-8.91	67.34	-7.01	90.00	-8.14	90.00	-7.64	0.00
-15	85	-19.63	75.72	-16.42	90.00	-18.15	90.00	-17.47	0.00
-30	85	-34.41	0.00	-31.63	90.00	-33.87	90.00	-33.50	0.00
-45	85	-46.12	0.00	-46.56	90.00	-46.50	90.00	-46.09	0.00
-60	85	-55.39	67.20	-56.87	90.00	-58.24	90.00	-56.28	84.35
-75	85	-63.90	11.01	152.81	60.23	-81.80	90.00	-70.20	60.64

End of Table B.7

Table B.8: Estimated incident angles data measurements (transmit power 2.0 dBm and vertical port)

Reference Angles		AVG		MVDR		MUSIC		ESPRIT	
Az.	El.	Az.	El.	Az.	El.	Az.	El.	Az.	El.
75	0	90.86	3.28	95.96	3.37	88.47	3.58	94.37	3.22
60	0	57.01	1.15	55.10	0.63	49.75	1.66	51.60	1.82
45	0	10.60	0.99	-89.10	-0.02	15.60	1.32	22.97	1.35
30	0	-5.99	1.27	-18.90	1.60	-0.67	1.48	3.71	1.55
15	0	-10.60	1.52	3.90	1.45	-5.90	1.72	-3.30	1.85
5	0	-14.47	1.69	-2.90	1.67	-9.98	1.91	-7.83	2.07
-5	0	-24.31	2.11	-22.90	2.65	-21.81	2.30	-21.05	2.47
-15	0	-28.85	2.17	-23.10	3.02	-27.09	2.37	-25.22	2.53
-30	0	-34.76	2.37	-26.23	3.10	-33.71	2.59	-30.91	2.77

Continuation of Table B.8

Reference Angles		AVG		MVDR		MUSIC		ESPRIT	
Az.	El.	Az.	El.	Az.	El.	Az.	El.	Az.	El.
-45	0	-36.75	2.46	-37.10	3.61	-38.00	2.72	-35.98	2.92
-60	0	-37.33	2.68	-34.10	3.53	-42.95	3.05	-42.86	3.15
-75	0	-43.29	3.05	-45.51	3.14	-51.25	3.27	-61.59	2.75
75	15	80.72	18.52	70.47	16.16	79.92	17.42	98.31	17.05
60	15	59.76	17.91	52.68	17.37	56.92	18.31	62.60	17.66
45	15	41.28	17.91	37.35	17.86	38.99	18.64	41.93	17.97
30	15	24.07	18.34	19.40	20.03	22.89	19.11	24.44	18.20
15	15	7.87	19.09	3.41	21.24	7.51	19.78	7.87	18.71
5	15	-2.67	19.82	-7.73	21.79	-2.59	20.45	-2.85	19.31
-5	15	-14.23	20.53	-12.98	21.66	-13.43	20.89	-14.23	19.46
-15	15	-23.17	20.71	-21.80	22.40	-22.07	20.91	-23.25	19.39
-30	15	-35.63	20.31	-34.06	22.27	-34.28	20.45	-35.93	18.92
-45	15	-47.98	19.27	-44.75	21.93	-46.34	19.64	-48.51	18.47
-60	15	-59.75	17.46	-57.16	19.54	-57.57	18.16	-59.28	17.26
-75	15	-69.70	13.62	-72.92	16.99	-66.76	15.21	-67.96	13.94
75	30	86.62	30.39	67.31	35.88	86.89	33.29	95.55	31.86
60	30	62.76	35.11	52.70	35.10	60.49	34.00	62.82	33.48
45	30	46.06	34.62	40.02	34.55	43.77	34.61	45.57	33.66
30	30	28.80	34.37	22.56	35.89	27.35	34.99	28.52	33.66
15	30	11.49	35.75	8.02	38.23	10.89	36.40	10.91	35.40
5	30	1.39	36.22	0.81	39.64	1.06	36.91	0.35	36.15
-5	30	-10.65	36.29	-8.03	38.52	-10.30	37.10	-11.35	36.18
-15	30	-21.99	35.80	-18.21	39.87	-21.15	36.50	-22.56	35.27
-30	30	-38.43	36.57	-35.80	37.11	-37.40	36.86	-39.45	34.84
-45	30	-51.82	37.83	-48.15	37.71	-50.49	37.30	-51.93	34.99
-60	30	-62.97	35.78	-57.98	38.02	-63.42	33.68	-61.55	31.24
-75	30	-82.32	23.76	-73.29	29.57	-79.84	26.11	-76.52	20.53
75	45	74.81	33.61	74.52	49.28	78.83	50.90	74.47	43.31
60	45	56.10	50.82	56.43	49.35	56.90	53.39	55.20	52.48
45	45	44.26	52.24	40.57	49.87	43.35	53.00	43.81	52.15
30	45	28.61	51.02	25.68	49.31	28.09	52.04	28.49	50.81
15	45	10.30	53.38	9.44	52.35	10.60	53.78	10.39	53.34
5	45	0.47	54.73	0.21	54.03	0.74	54.80	0.72	54.69
-5	45	-8.07	54.22	-9.18	55.73	-7.99	54.48	-7.86	54.25
-15	45	-18.48	52.27	-18.10	54.41	-18.01	52.88	-18.18	51.92

Continuation of Table B.8

Reference Angles		AVG		MVDR		MUSIC		ESPRIT	
Az.	El.	Az.	El.	Az.	El.	Az.	El.	Az.	El.
-30	45	-36.43	51.25	-35.88	52.42	-35.17	51.41	-36.60	50.05
-45	45	-49.76	54.80	-48.11	56.49	-48.89	53.75	-50.08	52.68
-60	45	-57.04	46.99	-59.68	51.56	-61.95	53.07	-61.58	51.15
-75	45	-83.69	33.81	-76.55	41.09	-83.38	44.10	-87.67	37.02
75	60	70.34	33.61	71.49	52.42	76.30	62.86	71.91	56.44
60	60	55.14	61.71	51.52	59.68	54.40	63.71	51.14	61.05
45	60	42.99	67.21	40.48	64.16	42.16	67.20	41.85	66.41
30	60	28.40	66.58	27.87	66.36	27.61	67.30	28.36	66.32
15	60	9.87	67.90	10.24	70.37	9.75	70.34	9.71	69.80
5	60	0.21	68.15	1.35	71.69	0.17	72.99	0.29	73.01
-5	60	-8.88	69.03	-8.20	72.41	-8.88	72.18	-8.22	71.44
-15	60	-19.44	69.67	-18.67	73.37	-19.65	70.37	-19.08	69.06
-30	60	-36.02	69.11	-34.76	69.39	-35.72	70.37	-35.66	69.06
-45	60	-47.96	70.04	-47.42	67.15	-47.68	71.41	-47.65	69.52
-60	60	-58.37	60.18	-60.52	67.91	-59.42	71.16	-59.51	66.94
-75	60	-59.11	21.73	-79.73	69.37	-82.78	69.41	-86.16	48.45
75	75	73.01	43.83	-150.78	58.26	76.45	76.56	75.39	65.14
60	75	54.08	56.90	53.24	68.01	56.62	75.81	54.23	73.45
45	75	44.03	74.78	38.56	79.81	46.19	90.00	45.68	0.00
30	75	31.59	0.00	27.46	90.00	29.76	90.00	28.97	0.00
15	75	14.80	68.43	13.09	90.00	13.43	90.00	12.74	0.00
5	75	3.56	62.74	3.35	90.00	3.16	90.00	3.14	0.00
-5	75	-7.69	66.50	-6.95	90.00	-6.97	90.00	-6.79	0.00
-15	75	-17.55	86.47	-16.61	90.00	-17.26	90.00	-16.96	0.00
-30	75	-35.86	0.00	-35.55	90.00	-34.95	90.00	-35.30	0.00
-45	75	-49.82	0.00	-47.19	90.00	-49.12	90.00	-49.96	0.00
-60	75	-59.82	68.77	-57.77	90.00	-60.89	85.60	-59.61	77.00
-75	75	-78.63	24.54	-79.56	90.00	-84.77	90.00	-84.06	68.60
75	85	54.64	71.87	56.28	90.00	55.65	90.00	55.51	0.00
60	85	44.93	0.00	43.34	90.00	45.16	90.00	45.84	0.00
45	85	75.03	39.67	-154.01	54.58	74.92	90.00	75.89	72.90
30	85	33.47	0.00	151.39	51.08	30.28	90.00	28.84	0.00
15	85	16.78	62.90	12.59	90.00	14.65	90.00	13.25	0.00
5	85	3.94	59.30	2.67	90.00	3.28	90.00	2.21	0.00
-5	85	-8.91	67.36	-7.31	90.00	-8.13	90.00	-7.62	0.00

Continuation of Table B.8

Reference Angles		AVG		MVDR		MUSIC		ESPRIT	
Az.	El.	Az.	El.	Az.	El.	Az.	El.	Az.	El.
-15	85	-19.62	75.66	-17.07	90.00	-18.14	90.00	-17.46	0.00
-30	85	-34.34	0.00	-31.59	90.00	-33.79	90.00	-33.43	0.00
-45	85	-46.18	0.00	-46.90	90.00	-46.56	90.00	-46.13	0.00
-60	85	-55.30	67.04	-57.38	90.00	-58.21	90.00	-56.25	84.58
-75	85	-63.11	10.83	151.14	59.78	-81.85	90.00	-69.78	60.62

End of Table B.8

Table B.9: Estimated incident angles data measurements (transmit power -8.5 dBm and vertical port)

Reference Angles		AVG		MVDR		MUSIC		ESPRIT	
Az.	El.	Az.	El.	Az.	El.	Az.	El.	Az.	El.
75	0	91.31	3.27	102.46	3.42	88.48	3.53	94.57	3.24
60	0	56.12	1.17	41.87	1.19	48.96	1.70	49.97	1.85
45	0	10.33	0.97	3.20	1.06	15.66	1.30	22.17	1.35
30	0	-5.73	1.25	-16.90	1.82	-0.41	1.46	3.26	1.54
15	0	-11.94	1.54	-18.90	1.63	-7.02	1.74	-4.48	1.86
5	0	-14.16	1.70	-2.90	1.82	-9.78	1.93	-7.68	2.08
-5	0	-23.73	2.10	-23.90	2.64	-21.30	2.30	-20.59	2.47
-15	0	-29.15	2.21	-20.20	2.84	-27.42	2.41	-25.78	2.58
-30	0	-34.44	2.36	-23.61	3.30	-33.47	2.58	-30.64	2.76
-45	0	-37.82	2.48	-39.10	3.51	-38.75	2.74	-36.79	2.92
-60	0	-37.29	2.64	-37.70	3.72	-43.16	3.02	-43.02	3.12
-75	0	-43.74	2.97	-50.60	2.85	-51.91	3.16	-62.75	2.66
75	15	80.62	18.59	71.36	14.51	79.67	17.59	98.32	17.16
60	15	59.65	17.97	51.90	17.36	56.87	18.38	62.50	17.72
45	15	41.25	17.95	36.96	17.83	38.97	18.67	41.89	18.00
30	15	24.09	18.32	20.77	19.71	22.88	19.10	24.44	18.19
15	15	7.90	19.05	2.23	21.56	7.52	19.75	7.84	18.69
5	15	-2.66	19.82	-8.38	21.61	-2.59	20.44	-2.85	19.31
-5	15	-14.20	20.55	-12.63	21.22	-13.40	20.91	-14.20	19.48
-15	15	-23.16	20.70	-20.90	22.03	-22.05	20.91	-23.25	19.39
-30	15	-35.64	20.30	-33.16	22.05	-34.26	20.43	-35.95	18.90

Continuation of Table B.9

Reference Angles		AVG		MVDR		MUSIC		ESPRIT	
Az.	El.	Az.	El.	Az.	El.	Az.	El.	Az.	El.
-45	15	-47.97	19.22	-45.47	21.00	-46.37	19.59	-48.56	18.45
-60	15	-60.07	17.51	-58.77	19.59	-57.77	18.18	-59.42	17.28
-75	15	-70.09	13.53	-73.08	17.30	-67.10	15.21	-68.27	13.91
75	30	86.42	30.43	68.00	37.11	86.84	33.39	95.54	31.95
60	30	62.71	34.99	53.76	34.71	60.44	33.94	62.81	33.40
45	30	46.04	34.67	40.32	34.50	43.74	34.67	45.52	33.73
30	30	28.80	34.40	22.56	35.87	27.35	35.01	28.51	33.72
15	30	11.49	35.75	8.64	37.42	10.90	36.40	10.92	35.41
5	30	1.35	36.21	-0.12	38.56	1.02	36.90	0.31	36.15
-5	30	-10.49	36.26	-8.92	38.95	-10.12	37.06	-11.19	36.12
-15	30	-21.90	35.78	-18.96	39.92	-21.04	36.49	-22.46	35.23
-30	30	-38.39	36.54	-35.78	38.12	-37.36	36.81	-39.44	34.73
-45	30	-51.80	37.79	-47.76	37.52	-50.45	37.26	-51.91	34.92
-60	30	-62.92	35.74	-58.70	36.53	-63.41	33.68	-61.53	31.23
-75	30	-82.44	23.61	-77.17	30.43	-79.93	26.08	-76.84	20.37
75	45	73.94	29.91	72.72	47.23	79.09	51.39	74.21	43.07
60	45	56.05	50.70	55.86	50.18	56.85	53.31	55.09	52.35
45	45	44.31	52.35	40.64	50.42	43.38	53.09	43.87	52.28
30	45	28.61	50.97	26.04	49.80	28.11	52.01	28.50	50.74
15	45	10.30	53.39	9.90	52.67	10.61	53.79	10.38	53.34
5	45	0.53	54.73	0.26	54.68	0.79	54.81	0.78	54.69
-5	45	-8.10	54.27	-9.17	56.37	-8.02	54.54	-7.88	54.29
-15	45	-18.44	52.17	-18.80	55.02	-17.97	52.78	-18.17	51.85
-30	45	-36.42	51.38	-35.73	53.63	-35.19	51.56	-36.58	50.11
-45	45	-49.77	54.69	-48.52	56.16	-48.90	53.65	-50.12	52.66
-60	45	-56.95	46.85	-60.65	51.72	-61.93	53.13	-61.55	51.17
-75	45	-83.00	32.21	-88.54	66.39	-83.22	43.63	-87.88	36.30
75	60	70.23	33.50	68.80	56.66	76.24	63.03	71.94	56.74
60	60	55.10	61.61	51.83	59.97	54.42	63.77	51.16	61.09
45	60	43.03	67.18	40.03	63.20	42.21	67.17	41.91	66.39
30	60	28.39	66.57	27.73	66.08	27.61	67.30	28.35	66.28
15	60	9.87	67.80	10.22	70.46	9.74	70.35	9.70	69.80
5	60	0.15	68.04	1.41	72.09	0.11	72.83	0.23	72.83
-5	60	-8.85	68.86	-8.35	73.46	-8.84	72.10	-8.18	71.30
-15	60	-19.48	69.75	-18.98	73.08	-19.68	70.42	-19.14	69.20

Continuation of Table B.9

Reference Angles		AVG		MVDR		MUSIC		ESPRIT	
Az.	El.	Az.	El.	Az.	El.	Az.	El.	Az.	El.
-30	60	-36.00	69.08	-34.82	70.97	-35.69	70.34	-35.63	69.01
-45	60	-47.94	69.94	-47.15	68.29	-47.68	71.35	-47.65	69.41
-60	60	-58.22	60.03	-57.94	62.38	-59.36	71.06	-59.44	66.80
-75	60	-59.09	21.53	-55.53	37.93	-82.85	69.37	-86.38	48.34
75	75	72.52	42.78	71.66	42.99	76.43	77.19	75.37	64.97
60	75	54.14	56.91	50.68	58.23	56.54	75.40	54.36	73.42
45	75	43.96	74.42	43.30	90.00	46.24	90.00	45.75	0.00
30	75	31.57	0.00	26.97	90.00	29.78	90.00	29.00	0.00
15	75	14.77	68.15	13.72	90.00	13.38	90.00	12.70	0.00
5	75	3.57	62.71	2.65	90.00	3.18	90.00	3.16	0.00
-5	75	-7.69	66.39	-6.76	90.00	-6.96	90.00	-6.78	0.00
-15	75	-17.62	84.41	-16.68	90.00	-17.28	90.00	-16.97	0.00
-30	75	-35.88	0.00	-34.98	90.00	-34.94	90.00	-35.32	0.00
-45	75	-49.76	0.00	-47.34	90.00	-49.07	90.00	-49.88	0.00
-60	75	-58.58	64.05	-55.10	68.33	-60.49	82.57	-59.00	75.76
-75	75	-78.77	22.71	-53.75	51.37	-84.62	90.00	-83.81	67.99
75	85	54.56	71.15	56.12	89.10	55.62	90.00	55.51	0.00
60	85	44.88	0.00	170.08	58.00	45.12	90.00	45.80	0.00
45	85	74.41	38.28	-155.51	53.15	74.94	90.00	76.22	74.16
30	85	33.54	0.00	151.50	55.05	30.25	90.00	28.76	0.00
15	85	16.87	62.60	12.49	90.00	14.66	90.00	13.27	0.00
5	85	4.04	59.33	2.63	90.00	3.37	90.00	2.26	0.00
-5	85	-8.91	67.04	-7.78	90.00	-8.12	90.00	-7.62	0.00
-15	85	-19.72	75.07	-16.15	90.00	-18.13	90.00	-17.46	0.00
-30	85	-34.36	0.00	-32.55	90.00	-33.78	90.00	-33.41	0.00
-45	85	-46.11	0.00	-46.18	90.00	-46.52	90.00	-46.09	0.00
-60	85	-54.36	64.58	-51.97	69.36	-58.01	90.00	-56.07	84.39
-75	85	-61.56	10.83	154.64	61.81	-81.58	90.00	-69.02	58.06

End of Table B.9

Appendix C

Results Antenna Compensation with Varying Snapshot Count

A comprehensive overview of the results for antenna deviation compensation is provided where each table is assigned a specific incident angle.

Table C.1: Improvements antenna deviation compensation at 90° azimuth and 15° elevation

Snapshots	AVG		MUSIC		ESPRIT	
	Az.	El.	Az.	El.	Az.	El.
1	0.10	0.03	0.30	0.00	0.27	0.07
2	0.08	0.02	-0.27	0.10	0.18	0.06
3	0.06	0.02	-0.03	0.02	0.14	0.04
4	0.06	0.02	-0.32	0.12	0.13	0.04
5	0.05	0.02	0.40	0.04	0.12	0.03
6	0.05	0.02	-0.23	0.03	0.11	0.04
7	0.05	0.01	0.52	-0.07	0.11	0.03
8	0.06	0.01	0.35	0.02	0.10	0.03
9	0.05	0.01	-0.21	0.02	0.10	0.03
10	0.05	0.02	0.19	0.00	0.10	0.02
20	0.04	0.01	0.06	0.00	0.08	0.02
30	0.04	0.00	0.06	0.01	0.08	0.01
40	0.05	0.00	0.06	0.01	0.08	0.01
50	0.05	0.01	0.06	0.01	0.08	0.01

Table C.2: Improvements antenna deviation compensation at 90° azimuth and 30° elevation

Snapshots	AVG		MUSIC		ESPRIT	
	Az.	El.	Az.	El.	Az.	El.
1	-0.04	0.06	-0.14	-0.06	-0.06	0.04
2	-0.01	0.04	0.04	-0.09	-0.05	0.01
3	-0.02	0.03	-0.06	-0.09	-0.04	0.00
4	-0.01	0.02	0.02	-0.15	-0.04	-0.01
5	0.00	0.02	0.04	-0.14	-0.04	-0.02
6	0.00	0.02	-0.02	0.01	-0.03	-0.02
7	-0.01	0.02	0.03	-0.06	-0.03	-0.02
8	-0.01	0.01	-0.08	-0.10	-0.04	-0.02
9	-0.01	0.01	-0.11	-0.03	-0.04	-0.02
10	-0.01	0.02	-0.01	-0.01	-0.04	-0.02
20	0.00	0.01	-0.03	-0.03	-0.03	-0.03
30	0.00	0.01	-0.03	-0.02	-0.03	-0.03
40	0.00	0.02	-0.03	-0.02	-0.03	-0.02
50	0.00	0.01	-0.03	-0.02	-0.03	-0.02

Table C.3: Improvements antenna deviation compensation at 90° azimuth and 45° elevation

Snapshots	AVG		MUSIC		ESPRIT	
	Az.	El.	Az.	El.	Az.	El.
1	-0.02	-0.16	0.02	0.18	-0.03	0.01
2	0.00	-0.16	-0.18	0.00	-0.01	0.01
3	0.00	-0.17	-0.01	-0.14	-0.01	0.00
4	0.01	-0.16	-0.16	-0.13	-0.01	0.00
5	0.01	-0.16	-0.13	0.02	-0.01	0.00
6	0.01	-0.17	-0.03	0.11	-0.01	0.00
7	0.01	-0.17	-0.02	0.07	0.00	0.00
8	0.01	-0.17	-0.02	0.07	0.00	0.00
9	0.02	-0.17	0.00	0.01	0.00	0.01
10	0.02	-0.17	0.02	0.10	0.00	0.00
20	0.02	-0.16	0.01	0.00	0.00	0.01
30	0.02	-0.17	0.00	0.00	0.01	0.00
40	0.01	-0.17	0.00	0.01	0.01	0.01
50	0.01	-0.17	0.01	0.01	0.00	0.01

Table C.4: Improvements antenna deviation compensation at 90° azimuth and 60° elevation

Snapshots	AVG		MUSIC		ESPRIT	
	Az.	El.	Az.	El.	Az.	El.
1	-0.03	-0.03	-0.03	-0.08	-0.06	0.21
2	-0.01	-0.09	-0.01	-0.46	-0.03	0.13
3	-0.01	-0.11	-0.08	-0.39	-0.02	0.11
4	0.00	-0.13	-0.05	-0.27	-0.03	0.09
5	0.00	-0.13	-0.12	-0.22	-0.02	0.09
6	0.00	-0.13	-0.08	-0.10	-0.02	0.08
7	0.00	-0.13	0.00	-0.51	-0.01	0.07
8	0.00	-0.14	-0.09	0.07	-0.02	0.06
9	0.00	-0.14	-0.02	0.04	-0.02	0.07
10	0.01	-0.15	0.07	0.11	-0.02	0.06
20	0.00	-0.15	-0.01	0.03	-0.01	0.06
30	0.01	-0.15	-0.01	0.03	-0.01	0.06
40	0.01	-0.16	0.00	0.03	-0.01	0.05
50	0.01	-0.16	0.00	0.03	-0.01	0.05

Table C.5: Improvements antenna deviation compensation at -90° azimuth and 15° elevation

Snapshots	AVG		MUSIC		ESPRIT	
	Az.	El.	Az.	El.	Az.	El.
1	-0.40	-0.01	-0.06	-0.04	-0.35	-0.03
2	-0.23	-0.01	-0.12	-0.01	-0.18	-0.03
3	-0.17	0.00	-0.07	0.05	-0.14	-0.02
4	-0.13	0.00	0.36	-0.05	-0.10	-0.02
5	-0.11	0.00	0.24	0.05	-0.07	-0.02
6	-0.10	0.00	0.14	-0.03	-0.07	-0.02
7	-0.09	0.00	0.16	-0.04	-0.07	-0.02
8	-0.08	0.00	0.09	0.01	-0.05	-0.02
9	-0.07	0.00	0.15	0.00	-0.03	-0.02
10	-0.06	0.00	0.14	0.01	-0.04	-0.02
20	-0.04	0.00	-0.03	-0.01	-0.02	-0.02
30	-0.03	0.00	-0.03	-0.01	-0.01	-0.02
40	-0.03	0.00	-0.02	-0.01	-0.01	-0.02
50	-0.02	0.00	-0.01	-0.01	-0.01	-0.02

Table C.6: Improvements antenna deviation compensation at -90° azimuth and 30° elevation

Snapshots	AVG		MUSIC		ESPRIT	
	Az.	El.	Az.	El.	Az.	El.
1	-0.07	-0.02	-0.09	0.04	-0.07	-0.03
2	-0.04	-0.02	-0.09	-0.02	-0.03	-0.01
3	-0.03	-0.01	-0.13	0.03	-0.03	0.00
4	-0.03	-0.01	0.00	-0.07	-0.01	-0.01
5	-0.02	0.00	-0.17	0.01	-0.01	0.00
6	-0.02	-0.01	-0.07	-0.05	-0.01	0.00
7	-0.02	-0.01	-0.12	-0.02	-0.02	0.01
8	-0.02	-0.01	-0.09	0.05	-0.01	0.01
9	-0.01	-0.01	0.00	0.02	-0.01	0.00
10	-0.01	-0.01	-0.01	0.02	-0.01	0.01
20	-0.01	-0.01	-0.01	0.01	-0.01	0.00
30	-0.01	-0.01	-0.01	0.00	-0.01	0.00
40	-0.02	0.00	-0.01	0.01	-0.01	0.00
50	-0.02	0.00	-0.01	0.01	-0.01	0.01

Table C.7: Improvements antenna deviation compensation at -90° azimuth and 45° elevation

Snapshots	AVG		MUSIC		ESPRIT	
	Az.	El.	Az.	El.	Az.	El.
1	-0.10	-0.03	0.05	-0.24	-0.02	-0.08
2	-0.06	-0.02	-0.05	0.21	0.01	-0.06
3	-0.04	0.00	-0.02	-0.04	0.01	-0.04
4	-0.03	-0.01	0.04	-0.41	0.01	-0.03
5	-0.02	0.00	0.10	0.09	0.02	-0.03
6	-0.02	0.00	0.17	-0.05	0.01	-0.03
7	-0.02	0.00	0.03	0.24	0.02	-0.03
8	-0.01	0.00	-0.04	0.14	0.02	-0.02
9	-0.01	0.00	0.06	0.09	0.02	-0.03
10	-0.01	0.00	0.00	0.09	0.02	-0.02
20	0.00	0.00	0.01	-0.02	0.02	-0.02
30	-0.01	0.00	0.01	-0.02	0.03	-0.02
40	-0.01	0.00	0.01	-0.02	0.03	-0.02
50	-0.01	0.00	0.01	-0.02	0.03	-0.02

Table C.8: Improvements antenna deviation compensation at -90° azimuth and 60° elevation

Snapshots	AVG		MUSIC		ESPRIT	
	Az.	El.	Az.	El.	Az.	El.
1	-0.01	-0.02	0.06	-0.25	0.00	-0.29
2	0.00	0.06	0.05	-0.18	0.00	-0.14
3	0.00	0.10	-0.05	0.03	0.00	-0.09
4	0.01	0.12	-0.09	0.53	0.00	-0.07
5	0.00	0.12	-0.20	0.39	0.00	-0.05
6	0.00	0.14	-0.09	-0.39	0.00	-0.04
7	0.00	0.14	0.09	-0.01	0.00	-0.04
8	0.00	0.15	0.05	-0.58	0.00	-0.04
9	0.00	0.15	-0.06	0.27	0.00	-0.03
10	0.01	0.15	0.01	-0.36	0.00	-0.03
20	0.01	0.16	0.00	0.01	-0.01	-0.02
30	0.01	0.17	0.00	0.01	0.00	-0.01
40	0.01	0.17	0.00	0.01	-0.01	-0.02
50	0.01	0.17	0.00	0.01	-0.01	-0.01